JOURNAL *of*

UNDERGRADUATE REPORTS IN PHYSICS

JURP

JURP

SOCIETY OF PHYSICS STUDENTS

Find SPS on:

Table of Contents

2020 • VOLUME XXVIV, ISSUE 1

The American Institute of Physics is a federation of scientific societies in the physical sciences, representing scientists, engineers, educators, and students. AIP offers authoritative information, services, and expertise in physics education and student programs, science communication, government relations, career services, statistical research in physics employment and education, industrial outreach, and history of the physical sciences. AIP publishes *Physics Today*, the most closely followed magazine of the physical sciences community, and is also home to the Society of Physics Students and the Niels Bohr Library & Archives. AIP owns AIP Publishing LLC, a scholarly publisher in the physical and related sciences. www.aip.org

AIP Member Societies:

American Association of Physicists in Medicine
American Association of Physics Teachers
American Astronomical Society
American Crystallographic Association
American Meteorological Society
American Physical Society
Acoustical Society of America
AVS: Science & Technology of Materials, Interfaces, and Processing
The Optical Society
The Society of Rheology

Other Member Organizations:
Sigma Pi Sigma physics honor society
Society of Physics Students
Corporate Associates

AIP | American Institute of Physics

A Letter from the ΣΠΣ President

by Jim Borgardt, PhD, Woolford Professor of Physics, Juniata College

Albert Einstein, Isaac Newton, Richard Feynman, Marie Curie, Galileo Galilei—what trait do these icons of physics, those we as a community hold to be the best of the best in our tradecraft, share?

The eminently quotable Feynman, speaking of his passion for knowledge, said "It has to do with curiosity. It has to do with people wondering what makes something do something." Renaissance giant Leonardo da Vinci lived by a motto, "Ostinato Rigore," conveying a philosophy of "stubborn rigor" or "tenacious application." Certainly, the most esteemed physicists all possessed an obstinate inquisitiveness.

But while essential to their success as physicists, we would never have heard of any of them if they did not disseminate their ideas and communicate the results of their work for peers to review. This practice of putting ideas out for assessment and critique is a hallmark of physics and fosters a sense of community around our common enterprise.

An essential element of professional life is communicating the results of your work with the broader community. For undergraduate researchers, publishing in a professional journal can be a challenging and daunting endeavor. Fortunately, the *Journal of Undergraduate Reports in Physics* (JURP), a peer-reviewed SPS publication, provides undergraduates with a dedicated place to publish their research findings. A primary goal of the journal is to educate and train students while also providing a means of public dissemination of research and programmatic activities.

One of my great pleasures as an academic, research mentor, ΣΠΣ/SPS advisor, and in my service as ΣΠΣ President is to engage with students as they develop their research skills and to hear students present their research. The excitement and sense of ownership students convey as they share their work at departmental presentations and at professional conferences is amazing to observe and provides assurance that the future of our discipline is in talented and capable hands. These venues offer critical avenues for students to hone their oral and written communication skills. JURP affords an additional mechanism by which undergraduate physics students can impart their research findings and become contributing members of a scholarly community.

In addition to serving as a place to present your research, JURP features student articles on recent professional conferences. Through the articles, JURP aims to introduce readers to these important gatherings and to highlight some of the cutting-edge research topics and opportunities they feature. You'll also find several inspiring reports by SPS chapters, featuring the amazing work they've done in outreach, community building, and research during the last year. These are just

ABOVE: Jim Borgardt. Photo courtesy of SPS National Office.

a small sample of the many projects that are financially supported by SPS and Sigma Pi Sigma donors each year.

I encourage you to make it a practice to read the *Journal of Undergraduate Reports in Physics* each summer, to be inspired by what you find in its pages, and to consider sharing your experiences and research findings with the physics community in response. In doing so, you'll be contributing to your professional community and following in the footsteps of Einstein, Curie, and others! //

Sigma Pi Sigma (ΣΠΣ), the national physics honor society, was founded in 1921 by students at Davidson College. It exists to honor outstanding scholarship in physics, to encourage interest in physics among students at all levels, to promote an attitude of service, and to provide fellowship for those excelling in physics. While its "linked but distinct" counterpart, the Society of Physics Students (SPS), is an organization that helps students transform themselves into contributing members of the professional community, Sigma Pi Sigma serves to provide a lifelong framework through which to advance its mission and provide opportunities to support future physicists.

The American Institute of Physics (AIP) generously underwrites Sigma Pi Sigma programs, including awards for chapter projects, outstanding service, and lifelong commitment to the organization's objectives of SPS and ΣΠΣ. Sigma Pi Sigma also hosts the Physics Congress, or PhysCon, an inclusive conference for undergraduate physics students. We are looking forward with great excitement to the upcoming Physics Congress in Washington, DC, and will mark the centennial celebration of the founding of ΣΠΣ!

Research
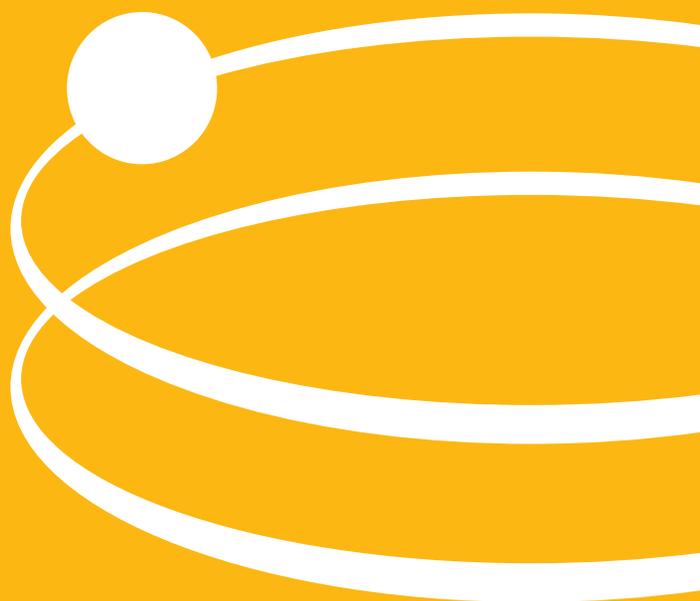
Numerical Study of Critical Liquid Droplets Using Density Functional Theory for 2D Lattice Gas with Short-Range Interactions

Joseph Watson [a]

Department of Physics, McMurry University, Abilene, Texas 79697, USA

[a] Corresponding author: watson.joseph@mcm.edu

Abstract. The method of density functional theory (DFT) was used to create a simulation of a droplet inside a supersaturated vapor. This DFT model was based on a two-dimensional lattice structure with short-range interactions. Closest and second-closest neighbor interactions were included. An iterative numerical procedure was used to solve the DFT equation for the density profile of a critical liquid droplet. Droplets of different radii for a wide range of chemical potentials above coexistence were simulated. Surface tension was found to approach a maximum for a planar liquid-vapor interface as droplet radius increased at a constant temperature. Dependencies of surface tension on the radius shifted as temperature changed.

INTRODUCTION

Density functional theory (DFT) has been widely used in computational physics for solving problems related to interfacial phenomena. An important aspect of a liquid-vapor interface that could be studied with the help of DFT is the surface tension. Surface tension of a critical liquid droplet is one of the key factors that affect the rate of homogeneous nucleation during the first-order phase transition in supersaturated vapor. Original DFT studies of homogeneous nucleation were conducted in the late 1980s and early 1990s.[1,2] Similar DFT models were used in the late 1990s[3,4] to study the dependence of surface tension on the radius of liquid droplets. All these studies involve quite sophisticated DFT approaches that are based on integral equations to account for long-range interactions in fluid and hard sphere approximations to account for short-range interactions. It would have been overly challenging as an undergraduate student to master numerical approaches to solve these DFT equations. However, several years ago a paper devoted to a much simpler two-dimensional (2D) lattice gas version of DFT was published in the *American Journal of Physics*.[5] This work has been studied as part of an upper-division thermodynamics course. The results presented here were obtained in the research project completed during this course. It was surprising to see that results conceptually match the results from much more sophisticated DFT studies, even though a rather simple model was used which did not require very extensive computational work. To obtain a better understanding of these results, it is encouraged to study this work in conjunction with Ref. 5.

DFT FOR 2D LATTICE GAS

Following Ref. 5, a 2D lattice fluid that consists of circular particles with unit diameter was considered for this project. These particles can fill enumerated (sub index i) sites of a rectangular lattice. The number of particles is much smaller than the number of sites, so some sites are going to have one particle (occupation number $n_i = 1$), and some will have none (occupation number $n_i = 0$). Particles can interact by means of the short-range attractions. Only closest neighbor interactions on the four sides of a given particle and second-closest neighbor interactions diagonal to a given particle are accounted for. Corresponding strengths for these interactions are of ε and $\varepsilon/4$. The density of the fluid is constant (ρ) for the bulk homogeneous fluid (liquid or gas) or varying in space (ρ_i) for inhomogeneous fluid, such as liquid droplets inside of gas. This density, $\rho_i = <n_i>$, is the average value of occupation numbers for a given site over all possible configurations of the system. DFT allows the thermodynamic properties of the fluid to be obtained as a function of this average density. This work considers the fluid to be in grand canonical ensemble, so the following equation was used for grand thermodynamic potential:[5]

$$\Omega = k_B T \sum_i [\rho_i \ln \rho_i + (1 - \rho_i) \ln(1 - \rho_i)] - \frac{1}{2} \varepsilon \sum_i \rho_i \sum_j \rho_j - \frac{1}{2} \frac{\varepsilon}{4} \sum_i \rho_i \sum_k \rho_k - \mu \sum_i \rho_i \tag{1}$$

In this equation, k_B is the Boltzmann constant, T is thermodynamic temperature, and μ is chemical potential. Summation with respect to j is performed through the closest neighbors, and summation with respect to k is performed through the next-closest neighbors. The extreme value of this grand thermodynamic potential delivers the density profile of the system at equilibrium, which satisfies this density profile equation:[5]

$$\rho_i = (1 - \rho_i) \exp \left[\frac{1}{k_B T} \left(\mu + \varepsilon \sum_j \rho_j + \frac{\varepsilon}{4} \sum_k \rho_k \right) \right] \tag{2}$$

This equation must be solved in order to determine the density profile of critical liquid droplets in equilibrium with their supersaturated vapor surroundings. Once determined, this density profile can be used to find other thermodynamic properties of a two-phase system.

THERMODYNAMICS OF A TWO-PHASE SYSTEM

From the standpoint of classical thermodynamics, the grand thermodynamics potential of a two-phase system can be split into two contributions: the bulk phases and interfacial contribution. In a 2D case, one can assume that a circular liquid droplet is formed in the middle of an open square ($L \times L$ lattice cells) system, which reduces grand thermodynamic potential:

$$\Omega = -P_l \pi R^2 - P_v (L^2 - \pi R^2) + \sigma 2\pi R \tag{3}$$

Here P_l is the bulk liquid pressure, P_v is the bulk vapor pressure, and σ is the 2D analog of the surface tension. The radius R of the droplet can be calculated assuming an equimolar divining surface:

$$N = \rho_l \pi R^2 + \rho_v (L^2 - \pi R^2) \tag{4}$$

Here ρ_l is the density of bulk liquid and ρ_v is the density of bulk vapor. N is the total number of particles in the system, and by solving that equation, the radius R can be found:

$$R = \sqrt{\frac{N - \rho_v L^2}{\pi (\rho_l - \rho_v)}} \tag{5}$$

This radius can then be used in Eq. (3), which gives the 2D analog of the surface tension:

$$\sigma = \frac{\Omega + P_v L^2 + (P_l - P_v) \pi R^2}{2\pi R} \tag{6}$$

NUMERICAL PROCEDURE FOR SOLVING DFT EQUATION

The density of the bulk liquid and bulk vapor, as well as the pressure, were found by solving the bulk fluid equations introduced in Ref. 5. This was done for a large range of chemical potentials above the coexistence value but below the spinodal value. One can use bulk fluid phase diagrams and equations from Ref. 5 for numeric values of these thermodynamic properties. An iteration procedure described in Ref. 5, with a mixing parameter in the Picard iteration algorithm of 0.02, was used to solve Eq. (2). Following the approach originally introduced in Ref. 1, an initial approximation for the density profile was set to supersaturated vapor everywhere except inside of a region with a given initial radius, where it was set to the bulk liquid. Since the desired solution would represent an unstable critical droplet inside of a supersaturated vapor, the number of particles in the system was monitored throughout iterations to see if the droplet was growing or decreasing. After the original droplet radius was set to 1, iterations were performed until the iteration procedure started diverging. If the number of particles in the system was decreasing at this point, the original radius was increased by 1 and the entire procedure was repeated. The simulation was stopped when the number of particles started to increase. The number of particles in the system at that point was then used to calculate the radius of the critical droplet and the 2D analog of surface tension according to Eqs. (5) and (6).

RESULTS AND CONCLUSIONS

Density profiles of critical droplets inside a 150-lattice cell square matrix were calculated for different chemical potentials (supersaturations) and corresponding droplet radii. Figure 1(a) shows a typical density profile for a droplet with a radius of six lattice cells. Figure 1(b) shows how the density profile changes for decreasing radii. The most interesting result was that for the smallest droplets, the bulk liquid phase is not realized at the center. This points to self-overlapping of the surface layer and is consistent with the results found in more sophisticated DFT models.[1–3] Figure 2(a) shows how surface tension increases to a maximum as the radii increase and how an increasing shift occurs to that maximum as temperature is decreased. This is consistent with the previous findings for small droplets,[3] where

the surface tension would be substantially smaller than that in the planar limit. However, the present model is incapable of predicting nonmonotonic behavior for surface tension as a function of the droplet radius, because no negative Tolman length[3,4] is found for very large droplets. This is not surprising, since liquid and vapor have artificially symmetric bulk properties in this model. This would be considered the weakest feature of this model. Figure 2(b) shows how chemical potential depends on the critical droplet radii and how an increasing shift and change in curvature occur as temperature increases. These dependencies could serve as inputs to study the kinetics of homogeneous nucleation.

(a)	(b)
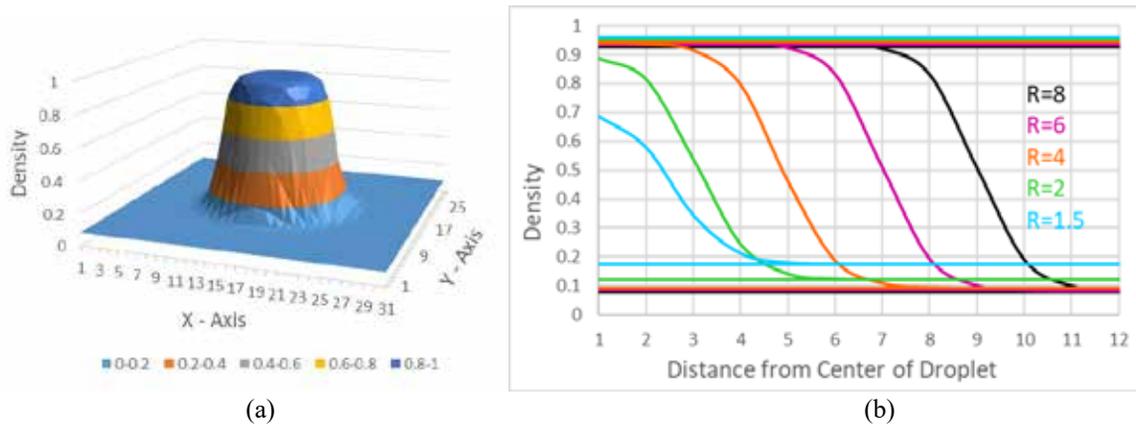
FIGURE 1. (a) A typical density profile [$(\mu-\mu_{coex})/k_BT = 0.11$, $\mu_{coex}/k_BT = -3.01$, $k_BT = 0.83\varepsilon$]. (b) Cross sections of density profiles for droplets of different radii at $k_BT = 0.83\varepsilon$. Position and radii are measured in number of lattice cells. Horizontal lines represent bulk densities.

(a)	(b)
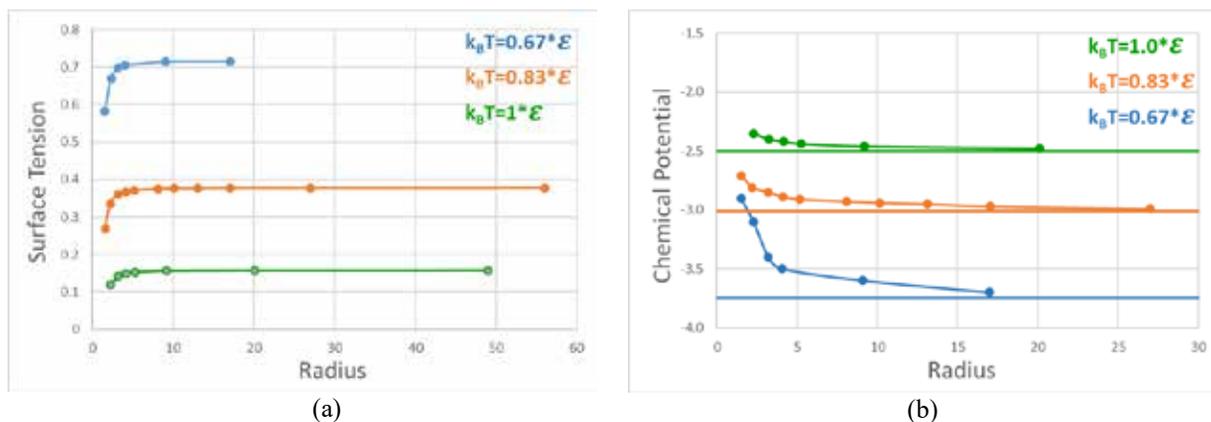
FIGURE 2. (a) 2D analog of surface tension (in k_BT/lattice cell size) for different temperatures and droplet radii. (b) Dependence of chemical potential (in k_BT) on droplet radii, where $\mu_{coex}/k_BT = -2.50\varepsilon/k_BT$, and horizontal lines represent these μ_{coex} values for corresponding temperatures. Radii are measured in the number of lattice cells.

AKNOWLEDGMENTS

REFERENCES

1. D. W. Oxtoby and R. Evans, J. Chem. Phys. **89**, 7521–7530 (1988).
2. X. C. Zeng and D. W. Oxtoby, J. Chem. Phys. **94**, 4472–4478 (1991).
3. T. V. Bykov and A. K. Shchekin, Colloid J. **61**, 144–151 (1999).
4. T. V. Bykov and A. K. Shchekin, Inorg. Mater. **35**, 759–763 (1999).
5. A. P. Hughes, U. Thiele, and A. J. Archer, Am. J. Phys. **82**, 1119–1129 (2014).

Three-Dimensional Relativistic Jet Simulations of Radio-Loud Active Galactic Nuclei (AGN)

Terance Schuh,[1, a)] Yutong Li,[2] and Paul J. Wiita[1]

[1]*Department of Physics, The College of New Jersey, Ewing, New Jersey 08618, USA*
[2]*Institute of Space Sciences, Shandong University, Weihai, People's Republic of China*

[a)]schuht1@tcnj.edu

Abstract. We have computed a suite of simulations of propagating three-dimensional relativistic jets involving substantial ranges of initial jet Lorentz factors and ratios of jet density to external medium density. These allow us to categorize the respective active galactic nuclei (AGN) into Fanaroff-Riley (FR) class I (jet dominated) and FR class II (lobe dominated) based upon the stability and morphology of the simulations. We used the Athena code, and more recently, the Athena++ code, to produce a collection of large 3D variations of jets, many of which propagate stably and quickly for over 100 jet radii, but others of which eventually become unstable and fill up slowing advancing lobes. Comparing the times when some jets become unstable to these initial parameters allows us to find a threshold where radio-loud AGNs transition from class II to class I. With our highest resolution, fully 3D relativistic simulations we can represent the jets more accurately and thus improve upon and refine earlier results that were based on both our now high-resolution 3D and 2D simulations.

INTRODUCTION

Active galactic nuclei (AGN) are galaxies that not only have a supermassive black hole at the center but also emit an intense amount of radiation solely due to the black hole and not the surrounding stars within the galaxy. The black hole is so large and in the process of consuming so much matter that it causes the material it has not yet swallowed to generate so much energy that compared to all the light produced from the billions of stars in the respective galaxy, we see only the radiation due to the black hole! A small percentage of these AGN, around 10%, are classified as radio loud,[1] primarily meaning that they are characterized by relativistic plasma jets extending from the north and/or south poles of the black hole. These jets are linear structures that transport energy and particles at speeds near the speed of light from the compact central region of the AGN out to thousands of parsecs or sometimes even millions of parsecs in length. Another important characteristic of these jet structures is that they emit synchrotron radiation, an observational phenomenon where charged particles such as electrons spiral around magnetic fields, again causing large amounts of radiation to be emitted across the electromagnetic spectrum.[2] Due to the uniqueness and high energy of these radio-loud AGN we desire to understand their underlying physics.

FR I and FR II

The previously described radio jets have long been classified into two categories based upon their radio morphology.[3] Fanaroff-Riley I (FR I) sources have jet-dominated emission and are weaker, with the majority of their radiation arising from the inner halves. The FR II, on the other hand, or classical double sources, have emission dominated by lobes containing terminal hot spots. Furthermore, some hybrid-morphology radio sources (HYMORS) have been discovered that show FR I structure on one side of the radio source and FR II morphology on the other.[4] These sources are important in understanding the basic origin of the FR I and FR II dichotomy, where the different morphologies may be induced by intrinsically different jet properties, interactions with different environments on

either side of the source, or long-term temporal variations combined with the time lag in the observer's frame between evolving approaching and receding lobes.

(a)　　　　　　　　　　　　　　　　　(b)
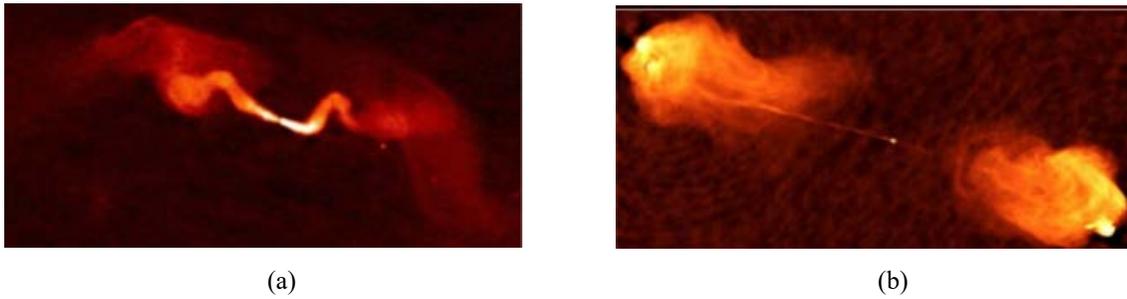
FIGURE 1. Two radio galaxies with jets seen using a radiograph. (a) An example of a FR I–type AGN, specifically, radio galaxy 3C 31. Image courtesy of the NRAO/AUI. (b) An example of a FR II–type AGN, specifically, Cygnus A. Image courtesy of the VLA.

METHOD OF RESEARCH

FR I or FR II type, these radio-loud AGN are impossible to physically create here on Earth, so like most astrophysical research, to study the astronomical objects we computationally model them using supercomputers. Because the jets are comprised of plasma, we can effectively treat them as a fluid; thus we employ hydrodynamical computer codes to generate our models. These hydrodynamical simulations of propagating jets are of critical importance to the understanding of radio galaxies and now have a history spanning four decades.[5–7] These simulations give fundamental support to the idea of the twin-jet models for radio galaxies.[8, 9] Like most computational work, the complexity of the simulations has increased in parallel with growing computational power and algorithm development, leading to a better understanding of the jet phenomenon, focusing on the study of the morphology, dynamics, and nonlinear stability of jets at kiloparsec and larger scales.

To perform our specific research we used The College of New Jersey's ELSA High Performance Computing Cluster in parallel with the Athena code and its successor Athena++, both developed by Stone and colleagues.[10–13] Both codes are highly efficient, grid-based codes for astrophysical magnetohydrodynamics (MHD) that were developed primarily for studies of the interstellar medium, star formation, and accretion flows. Athena++ has the capability to include special relativistic hydrodynamics (RHD), MHD, static (fixed) mesh refinement, and parallelization. The discretization is based on cell-centered volume averages for mass, momentum, and energy, and face-centered area averages for the magnetic field. In order to solve a series of partial differential equations expressing conservation laws, the rest density, pressure, velocity, internal energy, and magnetic field are calculated in the strictly RHD simulations with the magnetic field set to zero.

With the goal to understand the physics and characteristics of FR I– and FR II–type jets, we have simulated these propagating jets and created a very extensive suite of both medium- and high-power jets in three dimensions. Much previous work has been devoted to modeling relativistic jets in two dimensions rather than three dimensions due to a lack of computational power,[14] so after a thorough literature search, to our knowledge we are among the first research groups to model these large-scale jets three dimensionally while maintaining high resolution. Since in reality the jets are three dimensional, this enhancement allows us to classify them more accurately, making better predictions concerning the jets and developing a stronger understanding of them.

SIMULATIONS

We use the Athena code for special relativistic hydrodynamics and the Athena++ code for special relativistic MHD. These codes allow us to produce 3D simulations of jets propagating through initially uniform external or ambient media with a wide range of power. To model our jets, the initial physical parameters of jet velocity v_j (assumed constant across the cross section for our initially cylindrical jets), proper ambient and jet densities (ρ_a and ρ_j, respectively), ambient and jet pressures (P_a and P_j), magnetic fields (B_{jet} and B_{amb}), and adiabatic index Γ must be specified. Of these, the dominant variables are v_j and $\eta = \rho_j/\rho_a$, and these are the ones we discuss. In the MHD simulations the magnetic fields are also dominant variables, but because we have not been able to produce fully high-resolution 3D relativistic MHD simulations, we will not discuss them here.

With substantial experimentation involving different code parameters, our best overall results for faster jets came from simulations of highest resolution (HHR) 3D RHD jets with 1200 × 1000 × 1000 zones with 20 zones per grid. Previously our highest resolution had been 600 × 500 × 500 zones with 10 zones per grid. We now classify this resolution as high resolution (HR). Most recently, upwards of 60 HR RHD simulations have now successfully been performed with the Athena code with different combinations of jet velocities (v_j) and jet-to-ambient matter density ratios (η). Of these HR simulations we have been able to reproduce more than 10 of them at our new higher resolution (HHR). The simulations contain a range of η from 0.0005 to 0.0316 and a range of initial v_j from 0.7c to 0.995c. A summary of the results of these simulations is shown in Fig. 2. The circles in the figure represent runs with jets that eventually become unstable before the end of the grid at 60 or 120 jet radii is reached. This characteristic is intrinsic of FR I radio sources and is the reason why these sources, when scaled to extragalactic dimensions, appear the way they do (see Fig. 1a). The instability is created because the core of the jet is not powerful enough to propagate past a certain threshold on the grid, either due to v_j, η, or a combination of the two. On the contrary, triangles show parameters of runs with jets that are powerful enough to remain stable enough throughout the entire simulation (to even 240 jet radii) and thus are plausibly representative of FR II sources (see Fig. 1b).
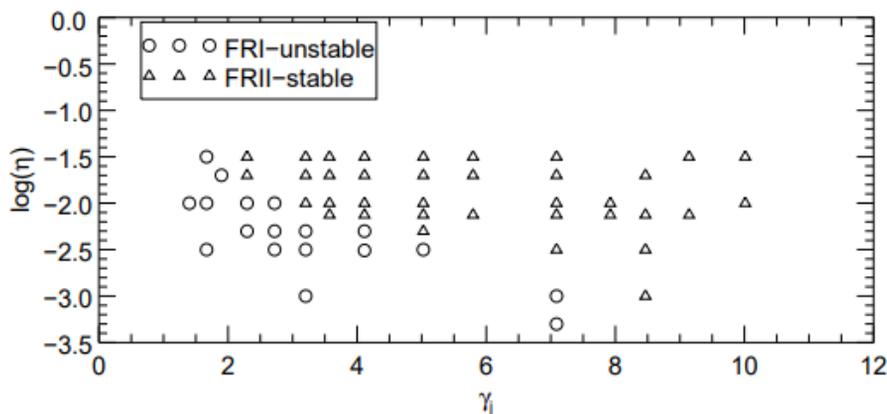
FIGURE 2. A summary of the stability of 54 jets. Note that these are our HR simulations. A subset of these have been produced using HHR. The x-axis is an alternate way of expressing v_j (a larger value corresponds to a faster jet), and the y-axis is a log scale of $\eta = \dfrac{\rho_j}{\rho_a}$. Circles represent FR I runs which have unstable jets; triangles are FR II runs with stable jets.

RESULTS AND ANALYSIS

For simplicity, rather than analyzing data from several runs and determining the overall results, we examine one FR I jet simulation but at the two resolution types and draw conclusions using this approach. The jet we focus on had parameters $v_j = 0.80c$ and $\eta = 0.00316$. The HR simulation had 600 × 400 × 400 zones with 10 zones per grid, and the HHR simulation had 1200 × 800 × 800 zones with 20 zones per grid.

The first step in analyzing any run is always identifying whether the jet becomes unstable, and if so, finding precisely when it does. In this specific case, we suspected our jet would be of the FR I variety, which it was, so thus we concerned ourselves with finding the point of instability. If we look at a short time lapse of the HR simulation, Fig. 3, we see everything begins stable at $t = 0$ and remains so up until approximately $t = 300$. Not shown, the instability first occurs at around $t = 330$, but its effects are especially evident at $t = 450$ because the jet (dark blue region) now appears wavy. It is clear it has lost its stability. As time goes on we continue to see the jet in its entirety propagate toward the edge of the grid, but the jet end (dark blue column region) has come to a stop at around 30 jet radii, while both the cocoon (dark blue balloonlike region) and bow shock (red region) continue to propagate, now more slowly, toward the edge of the grid. Having identified the location of instability (30 jet radii), we compare the simulation to its HHR counterpart. By doing so, we can draw conclusions about the differences between the resolution types.

t = 150   t = 450   t = 700
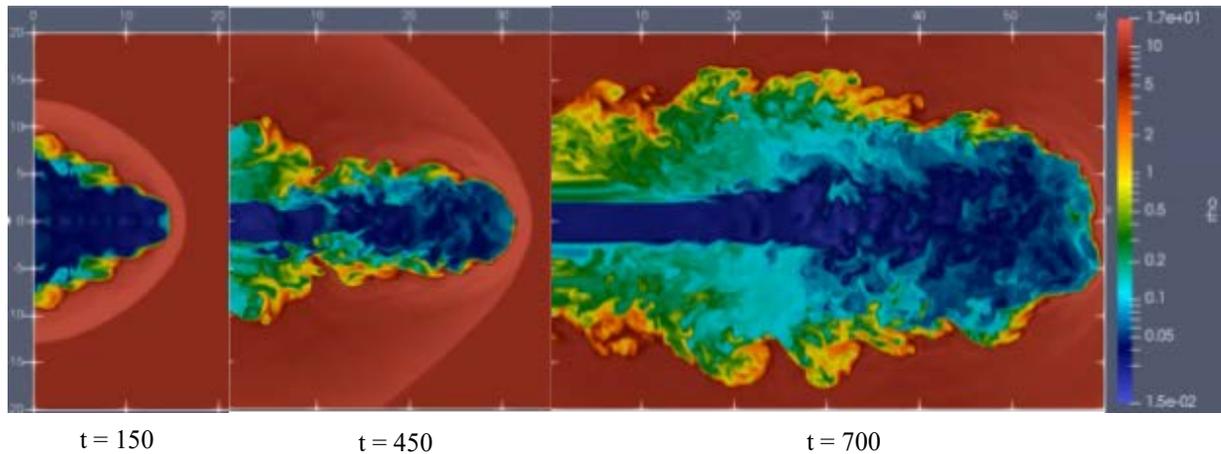
FIGURE 3. HR jet simulation with parameters $v_j = 0.80c$ and $\eta = 0.00316$. This simulation is an FR I type. We see that by t = 450, the jet has become unstable. This is seen by the waviness of the dark blue region. As the simulation continues, the jet itself (dark blue column region) remains nearly fixed at 30 jet radii, while other features such as the cocoon (dark blue balloonlike region) and bow shock (red region) propagate further and reach the edge of the grid.

Now examining the HHR simulation, we again look for the point where the jet goes unstable. Remember the parameters of this jet are identical. Looking at a time lapse, Fig. 4, we see everything begins stable at t = 0, as expected. Like the HR simulation, the jet begins to become unstable at around t = 300. After 100–200 time steps, later it is clear the jet has indeed become unstable, as seen by the wavy feature of the dark blue region. As the jet continues propagating, everything seems identical, except for the fact that we are at a higher resolution. Taking a closer look, we see that our HHR simulation propagates for the same amount of time as the HR version, but it does not propagate as far. We also notice that the jet end (dark blue column region) of the HHR simulation is at approximately 25 jet radii, which is 5 jet radii less than before. At first this is surprising, but it is actually somewhat expected. Because we are at a higher resolution now, the code is performing many more calculations. This is going to make propagation

t = 150   t = 450   t = 700
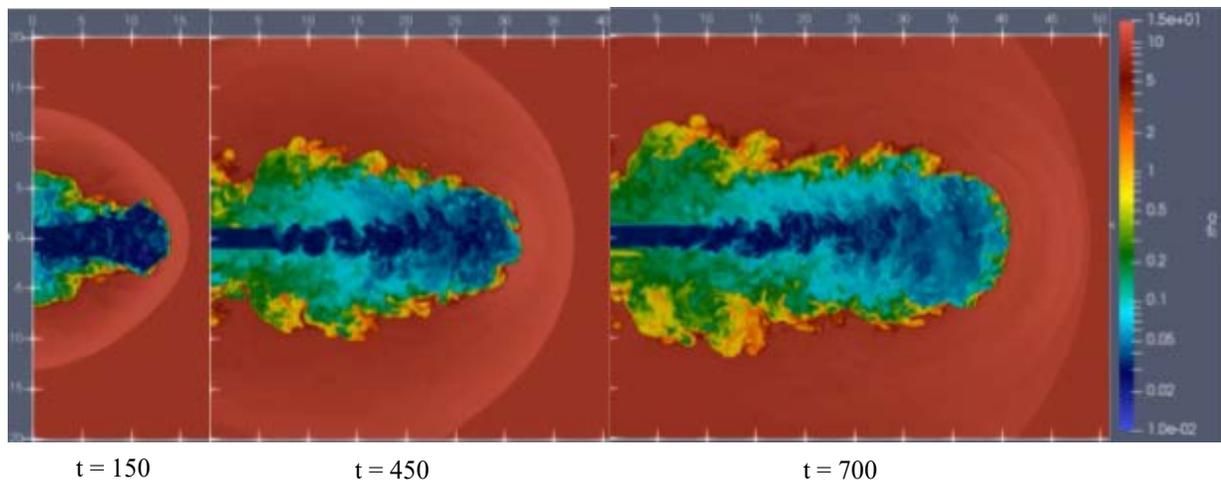
FIGURE 4. HHR jet simulation with the same parameters as the HR simulation in Fig. 3, $v_j = 0.80c$ and $\eta = 0.00316$. This simulation is also an FR I type. We see that by t = 450, the jet has become unstable in the same manner as Fig. 3. As the simulation continues and almost all features propagate further, approaching the edge of the grid, we see that the jet end (dark blue column region) remains nearly fixed at 25 jet radii. Note the progress each jet, Figs. 3 and 4, has made by t = 700. This is a result of the different resolutions.

take longer, but as a tradeoff we are able to see finer details in the jet. These are the reasons why the jet end does not propagate as far, and it actually means that we have produced an even more realistic simulation.

Albeit this is a brief analysis, the significance in increasing the resolution of our simulations is quite apparent. Also, although the above comparison revealed that both our resolution types resulted in FR I–type jets, we have to realize that that might not always be the case. We could have a HR simulation produce a FR I, but its HHR companion simulation produces a FR II. Knowing this, in the future it would be useful to perform even more HHR simulations of jets that already appear on our HR chart from Fig. 2. This way we can more accurately determine what types of three-dimensional jets are FR I and what types are FR II.

In addition to examining the jet morphologies, as mentioned previously, our work on our highest resolution 3D RHD simulations follows our previous high-resolution 3D RHD jet simulations[15] as well as our 2D RHD jet simulations.[14] Based on what we found, it is worth discussing how the various simulation types compare and why we are justified in assuming the highest resolution three-dimensional modeling is superior. Starting with 2D, we found that the simulations are actually more symmetric than 3D versions because fewer instabilities can be excited in the former. We also found that 2D simulations take longer times to cross the entire grid, and their jet ends are much further behind their corresponding bow shocks than they are in the 3D simulations. The biggest difference we found is that 2D simulations inflate much wider bow shocks and cocoons and therefore we lose information off the grid along the upper and lower boundaries. As expected, we discovered in comparing 2D to 3D that the differences are small, confirming our hypothesis that the 3D approach is not only valid but, indeed, superior.

When we compared the HHR simulations to the HR simulations, we first found that the former required 16 times more computational resources in order to make the two runs identical. This was expected, since we doubled the resolution in all three spatial directions and the time coordinate. We also found that HHR showed far more instabilities, because numerical data that could be seen as negligible in HR was now relevant. This led to more detailed, accurate jets. Consequently, the HR simulation propagated at a higher rate, which was also expected. Overall, our comparisons were mostly expected, and they justified our decision to increase our resolution. That being said, if we were to enhance the resolution even further, we would expect to see even more instabilities materialize. We would also like to think that where the FR I jets become unstable would reach a plateau point, meaning as resolution power increased, the times at which instabilities occur would converge to some absolute value. At that point we would have created simulations that depict, to the best ability, actual observed relativistic jets.

CONCLUSION

We have simulated an exceptionally large suite of over 50 3D RHD propagating jets using both Athena codes, 12 of which were reproduced at higher resolution. Our simulations of propagating jets have spanned a significant range of velocities (0.7c−0.995c) that cover the great majority of the velocities deduced for radio galaxies.[16] These flows are light, as is appropriate to radio jets, with jet density to ambient medium density ratios (η) between 5.0×10^{-4} and 3.2×10^{-2}. Both high-resolution (10 zones per jet radius) and higher-resolution (20 zones per radius) simulations have been completed, extending out to 60 jet radii along the direction of motion; in all cases our simulations had widths of 50 jet radii in the two perpendicular directions, so there was no loss of matter out of the grid along those transverse boundaries or the need to worry about waves reflecting off those boundaries and unphysically distorting the jet flow.

These simulations span a sufficient range in power so that the weaker ones are unstable before they pass through our simulation volumes. When scaled to the appropriate extragalactic dimensions and parameters, these cases yield FR I–type morphologies. The majority of our simulations took advantage of the relativistic velocities computable with the two codes and correspond to powerful sources that remain stable for very extended distances and times. On large scales these would be FR II radio galaxies, and on small scales they would be young radio galaxies. Comparisons between our HHR and HR simulations were also made which show that the HR simulations have fewer instabilities and detail, and they take less time to propagate across the entire grid.

In the future we would like to improve our jet simulations even further. This would include continuing to enhance the resolution capabilities of our simulations but also incorporating new factors into our models that we previously neglected for simplicity. An example of this would be using a more complex background medium where the density is nonuniform. This would most likely affect jet stability, but it would create an environment that is even more comparable to what is observed. Lastly, we would like to make more progress with Athena++ by producing fully 3D relativistic magnetohydrodynamic simulations. From there we would then like to produce light curves and power spectral density plots of simulations. This was previously done with the HR simulations to further verify our simulations with observational data. We hope to be able to reproduce those results with our current models. With all these additions, our jets would be even more accurate.

ACKNOWLEDGMENTS

REFERENCES

1. Y. C. Jiang *et al*., Astron. Astrophys. **469**(1), 331–337 (2007).
2. C. M. Urry and P. Padovani, Publ. Astron. Soc. Pac. **107**(715), 803 (1995).
3. B. L. Fanaroff and J. M. Riley, Mon. Not. R. Astron. Soc. **167**(1), 31P–36P (1974).
4. Gp. Gopal-Krishna *et al*., Mon. Not. R. Astron. Soc. **314**(4), 815–825 (2000).
5. D. R. Rayburn, Mon. Not. R. Astron. Soc. **179**(4), 603–617 (1977).
6. P. J. Wiita, Astrophys. J. **221**, 436–448 (1978).
7. M. L. Norman *et al.*, Astron. Astrophys. **113**, 285–302 (1982).
8. P. A. G. Scheuer, Mon. Not. R. Astron. Soc. **166**(3), 513–528 (1974).
9. R. D. Blandford and M. J. Rees, Mon. Not. R. Astron. Soc. **169**(3), 395–415 (1974).
10. T. A. Gardiner and J. M. Stone, J. Comput. Phys. **205**(2), 509–539 (2005).
11. J. M. Stone *et al*., Astrophys. J. Suppl. Series **178**(1), 137 (2008).
12. K. Beckwith and J. M. Stone, Astrophys. J. Suppl. Series **193**(1), 6 (2011).
13. C. J. White, J. M. Stone, and C. F. Gammie, Astrophys. J. Suppl. Series **225**(2), 22 (2016).
14. M. Pollack, D. Pauls, and P. J. Wiita, Astrophys. J. **820**(1), 12 (2016).
15. Y. Li *et al.*, Astrophys. J. **869**(1), 32 (2018).
16. M. L. Lister *et al*., Astronom. J. **137**(3), 3718 (2009).

OPTICAL BUFFERING IN A BOTTLE MICRORESONATOR ON AN OPTICAL FIBER

Kalista Schauer[a)] and Michael Pfenning[b)]

[1]United States Military Academy at West Point, West Point, New York 10996, USA
[a)]kalista.schauer@westpoint.edu
[b)]michael.pfenning@westpoint.edu

Abstract. Manufacturing highly efficient optical communications and computing devices requires designing dense integrated photonic circuits. Unfortunately, surface roughness of microscopic optical signaling devices results in light attenuation, decreasing the efficiency of the optical devices. A microscopic optical buffer would alleviate these issues; a potential solution is the Surface Nanoscale Axial Photonics (SNAP) platform. The SNAP platform operates because of the propagation of whispering gallery modes (WGMs) around the surface of an optical fiber. Because WGMs undergo slow axial propagation, they can be mathematically described by the one-dimensional Schrödinger equation. In this project, we calculate solutions to the effective wave equation to model the circulation of whispering gallery modes. We study the evolution of Gaussian-shaped wave pulses in a bottle microresonator on an optical fiber. By analyzing the propagation of WGMs within the bottle microresonator, we can examine the feasibility of creating a microscopic optical buffer for use in optical signal processing. In this project, we find analytical and numerical solutions to the effective wave equation, which is strikingly similar to the Schrödinger equation. We then use the numerical solutions to the effective wave equation to develop a model of the system in Mathematica.

INTRODUCTION

In 1935, Erwin Schrödinger introduced a thought experiment that applied quantum mechanics to a macroscopic system. In this gedanken, a cat is inside of a box that contains a radioactive particle and a vial of poison. If the particle decays, the poison is released and the cat dies. In quantum mechanics, the radioactive particle has two quantum states: decayed $= |\downarrow\rangle$ and undecayed $= |\uparrow\rangle$. Meanwhile, the cat also has two states: live $= |LL\rangle$ and dead $= |DD\rangle$. According to quantum mechanics, the system exists in a state of superposition where the cat is simultaneously alive and dead. This system is represented by the superposition wavefunction

$$\psi = \tfrac{1}{\sqrt{2}}[|\uparrow\rangle|LL\rangle + |\downarrow\rangle|DD\rangle]. \tag{1}$$

Upon measurement of the system, if the particle is undecayed, then the cat will still be alive. However, if the particle has decayed, then the cat will certainly be dead.

Heisenberg's uncertainty principle states that one cannot precisely measure position and momentum simultaneously, with σ being the standard deviation for position and momentum, and is represented mathematically as

$$\sigma_x \sigma_p \geq \tfrac{\hbar}{2} . \tag{2}$$

The time-dependent Schrödinger equation, written below, can be solved in order to find a particle's wavefunction:

$$i\hbar \frac{\partial \psi}{\partial t} = \frac{\hbar^2}{2m}\frac{\partial^2 \psi}{\partial x^2} + V\psi . \tag{3}$$

Any observable within a given system can be described in terms of the wavefunction. Wavefunctions are given as a superposition of sinusoidal (pure time harmonic) vibrations. A group of vibrations with high quantum number m and

small quantum number differences can be used to represent a particle. The wave group, or density of a particle, described in quantum mechanics is always compact, whereas in classical optics, wave groups spread out into large regions over time. This characteristic applies to multidimensional oscillators as well. This is because wave packets under classical optics are described as a continuum, whereas under quantum mechanics, they are represented as discrete harmonic components.[1]

An oft-studied problem in quantum physics is the infinite square well potential (Fig. 1). A particle in this potential is free, except at the boundaries of the square well. The boundaries of the potential constrain the particle and force it to oscillate. The potential is defined as

$$V(x) = \begin{cases} 0. \text{ if } 0 \leq x \leq a \\ \infty \text{ otherwise} \end{cases} \quad . \tag{4}$$
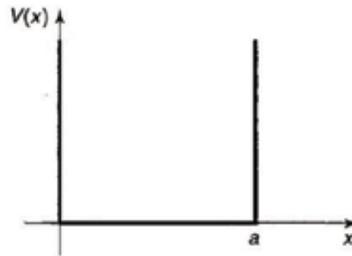
FIGURE 1. Infinite square well potential, Eq. (4).

A less idealized version of the infinite square well problem is that of the finite square well. In this problem, the potential is given by

$$V(x) = \begin{cases} -V_o & |x| < 1 \\ 0 & |x| \geq 1 \end{cases} \quad . \tag{5}$$
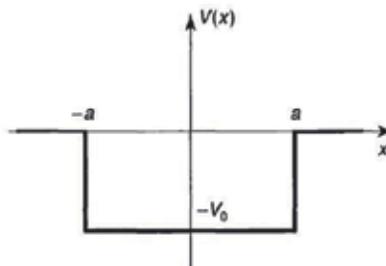
FIGURE 2. Finite square well potential.

Figure 2 is a depiction of Eq. (5).[2]

Harmonic Oscillator

In classical mechanics, a harmonic oscillator is often described as a system containing a mass m attached to a spring with force constant k. The motion of the spring-mass system is described by Hooke's law:[3]

$$-kx = m\frac{d^2x}{dt^2}, \tag{6}$$

with the solution

$$x(t) = A\sin(\omega t) + B\cos(\omega t) , \tag{7}$$

and potential energy

$$V(x) = \frac{1}{2}kx^2 . \tag{8}$$

In quantum mechanics, the potential is written as

$$V(x) = \frac{1}{2}m\omega^2 x^2 . \tag{9}$$

A quantum harmonic oscillator problem is solved by solving the Schrödinger equation for the above potential. The time-independent Schrödinger equation,[3]

$$\frac{d^2\psi}{dt^2} = -k^2\psi \, , \tag{10}$$

describes the particle within the simple harmonic oscillator, with the general solution being

$$\psi(x) = A\sin(kx) + B\cos(kx) \, , \tag{11}$$

where the possible energy values of the particle are quantized and given by[2]

$$E_n = \frac{n^2\pi^2\hbar^2}{2ma^2} \, . \tag{12}$$
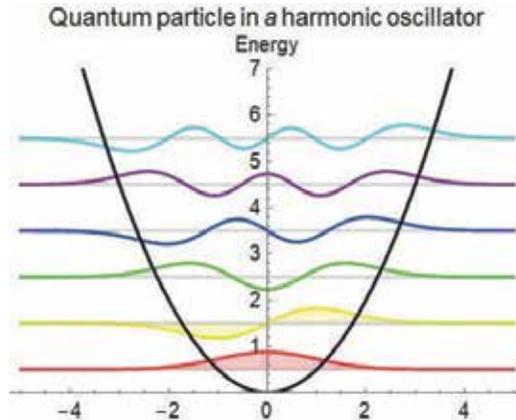
FIGURE 3. Mathematical model of a quantum particle in a harmonic oscillator.

The general solutions to the time-independent Schrödinger equation are visually similar to standing waves formed on a string with length a; the potential well solutions have a ground state corresponding to the lowest energy and excited states corresponding to higher energies. Figure 3 shows the quantized energy states of a quantum particle within a harmonic oscillator. I generated this plot using Mathematica software.

Within a one-dimensional harmonic potential, a wave packet oscillates periodically. These oscillations are not distorted over time, a property that is desired when creating many applications. While creating a one-dimensional harmonic resonator is not viable, it is possible to mimic a quantum wave packet within a harmonic potential by examining optical pulses within bottle microresonators. A Surface Nanoscale Axial Photonics (SNAP) bottle microresonator is defined as a dielectric cylinder that has a nanoscale deformation.[4] This fact is fundamental to this project.
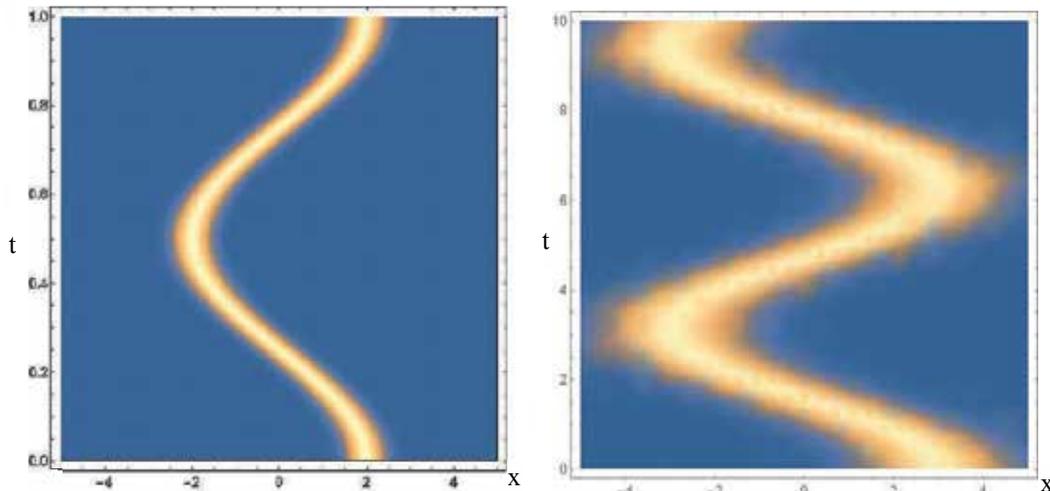
FIGURE 4. Left: A density plot of a stationary state of a wavefunction given in Schrödinger's paper. Right: Mathematica density plot of a Gaussian wave in a harmonic oscillator.

Whispering Gallery Modes

In open dielectric resonators, total internal reflection allows for closed trajectories of light. Within these resonators are circular optical modes known as whispering gallery modes (WGMs). WGMs are closed circular beams that occur because of total internal reflection. WGMs with low volume can achieve a high Q-factor, which is a dimensionless parameter that describes the level of damping of a resonator or oscillator. Simple geometries for open dielectric resonators include spheres, rings, or cylinders. The radius of curvature of these shapes is greater than several wavelengths, and the reflecting boundaries have high-index contrasts. Because of this, the Q-factor is only affected by material scattering or attenuation, which is caused by geometric imperfections such as surface roughness.[5]

Optical dielectric resonators with WGMs are a class of cavity devices that have useful properties, such as extremely high power density, narrow spectral linewidth, and small mode volume. WGM resonators can be used to study quantum electrodynamics or nonlinear optical phenomena. In modern optics, optical resonators are not only fundamental to laser devices, but are also tools for optical filtering and attaining accurate measurements. However, bulk optical resonators have disadvantages concerning size, alignment, stability, and weight. Thus, research began in miniaturized optical resonators that contain dielectric structures with circular symmetry and support WGMs.[6]

Surface Nanoscale Axial Photonics (SNAP)

Current efforts to create highly efficient optical communications and computing devices require some form of dense photonic integration. However, microscopic devices contain surface roughness that leads to undesirable attenuation of light. A possible solution is the SNAP platform. The SNAP platform relies on the circulation of whispering gallery modes around the surface of an optical fiber. WGMs undergo slow axial propagation, which can be mathematically described by the one-dimensional Schrödinger equation. Manipulating the fiber radius on the nanoscale level causes variance in the modes of the WGMs. SNAP devices are extremely low loss, as SNAP devices have fiber surfaces with low surface roughness.[7] Nanoscale variations of the radius of optical fibers result in an altered transmission spectrum. The evanescent field distribution of thin microfibers is very sensitive to nanoscale variations of the fiber radius. Optical fibers with larger radii are also sensitive to nanoscale variations of the fiber radius, and this effect is described by the slow propagation of WGMs along the axis of the fiber. Light in traditional silica optical fibers propagates along the interior core of the fiber. However, WGMs circulate around the surface of the fiber. The main premise of the SNAP platform is to manipulate WGM behavior by varying the effective fiber radius on an extremely small scale. Typically, WGMs can be excited by the evanescent field of a transverse microfiber. The SNAP platform is comprised of low-loss photonic integrated circuits that have sub-angstrom precision. The propagation of WGMs can be described by the Schrödinger equation, with energy proportional to variation of the wavelength and the potential $V(z)$ proportional to the variation of the radius.[8]

A focused CO_2 laser beam can modify the effective radius of the optical fiber on a nanoscale level. In order to achieve a predetermined variation of the radius, the laser beam is translated along the fiber. This method results in fabricated devices with sub-angstrom precision. This level of precision is more advanced than previous photonics technologies by two orders of magnitude.[8] To employ SNAP structures, we use a whispering-gallery-mode nanobump microresonator (NBMR). A NBMR is fabricated by creating a nanoscale-high asymmetric deformation on the surface of the optical fiber. This method is then used to fabricate the SNAP structures. NBMRs cause the localization of WGMs near a geodesic (a closed and stable ray) on the surface of the fiber. Fabricating an asymmetrical nanoscale bump on the surface of the fiber allows for the creation of a microresonator with a high Q-factor and the ability to confine WGMs. Provided that the bump's height is small, the path will be stable and the WGMs will be fully localized. High nanobumps can lead to unstable geodesics. The aforementioned CO_2 laser beam is used to create a nanoscale variation in the effective fiber radius. The laser heats only one side of the fiber radius, leading to the asymmetry of the nanobump. The characteristic axial width of the fundamental whispering gallery mode, when localized in close proximity to a stable geodesic, is given by

$$z_w = \left(\frac{\lambda}{2\pi n_r}\right)^{1/2} \frac{(a r_o)^{1/2}}{(\Delta r_o b)^{1/4}} \, , \tag{13}$$

with height Δr_o and widths a, b.[9]

CALCULATIONS

In this section, we examine the effective wave equation and calculate analytical solutions. The effective wave equation is very similar to the Schrödinger wave equation and differs only in terms of the constants. Thus, we can solve the effective wave equation as we would solve the Schrödinger wave equation. The effective wave equation is

$$i\mu \frac{\partial \psi}{\partial t} = -\frac{\partial^2 \psi}{\partial z^2} + V(x,t)\psi . \tag{14}$$

Given the above wave equation and the initial profile of the wave at time $t = 0$, we can solve for the solution for all times $t \geq 0$ by modeling and solving the well-posed Cauchy problem. A well-posed problem is one that satisfies the following conditions: (1) the problem has a solution, (2) the solution is unique within a specific class of functions, and (3) the solution is dependent upon parameters and data, so that small changes in the boundary or initial conditions results in small changes in the solution.

There are two important assumptions to note. First, we assume a static potential. Second, we assume that the potential is in the physical shape of either a cylinder, mathematically represented by a finite square well potential, or a parabolic-shaped bead, mathematically represented by a harmonic oscillator potential.

An important consequence of the first assumption is that the given modes, which are

$$\psi_k(z,t) = u_k(z)e^{i\omega_k t} \cdot a_k , \tag{15}$$

where $e^{i\omega_k t}$ represents the harmonic time dependence, imply the generic solution of

$$\Psi_k(z,t) = \sum_{\text{all modes } k} \psi_k(z)e^{i\omega_k t} \cdot a_k , \tag{16}$$

where a_k is a Fourier coefficient.

We use the initial condition of $\Psi(z,0)$ to determine the solution, giving

$$\Psi_k(z,0) = \sum_{\text{all modes } k} \psi_k(z) \cdot a_k \tag{17}$$

Solving the remainder of this problem requires using Fourier analysis. To do so, it is necessary to define the inner product as

$$\langle f(x), g(x) \rangle = \int_{\text{all space}} f(x)\overline{g(x)}dx . \tag{18}$$

For this specific problem, the inner product can be written as

$$\langle \Psi(z,0), \psi_j(k) \rangle = \sum_{\text{all modes}} \langle \psi_k, \psi_j \rangle a_k . \tag{19}$$

where j, k are arbitrary parameters. The inner product can also be represented as

$$\langle \Psi(z,0), \psi_j(k) \rangle = \sum_{\text{all modes}} \delta_{k,j} a_k , \tag{20}$$

where $\delta_{k,j}$ is the Kronecker delta, defined as

$$\delta_{k,j} = \begin{cases} 0, k \neq j \\ 1, k = j \end{cases} . \tag{21}$$

Because the Kronecker delta gives a nonzero result only when $k = j$, the only surviving term of the inner product is

$$\langle \Psi(z,0), \psi_j(k) \rangle = a_j . \tag{22}$$

Thus, the analytic solution to the well-posed Cauchy problem is

$$a_k = \langle \Psi(z,0), \psi_j(k) \rangle \tag{23}$$

$$\Psi(z,t) = \sum_{\text{all modes}} a_k \psi_k(z)e^{i\omega t} . \tag{24}$$

When the assumptions do not hold true, such as with beads of different shapes or time-changing potentials, it is necessary to abandon the analytic solution for a numerical simulation calculated on a computer.

RESULTS

Figure 6, middle, simulates a Gaussian pulse in an idealized infinite square well. This Mathematica-generated plot is two-dimensional and simulates the pulse as the light pulse propagates radially in the microresonator. This image shows that the Gaussian pulse reflects off the boundary of the microresonator and then interferes with itself, causing the interference patterns shown past $t = 0.2$. As the simulation uses an infinite square well, the only interference occurs from the pulse itself. The pulse only reflects off the boundary of the microresonator, and no part of the pulse is transmitted past the boundary. Figure 5 is a Mathematica-generated 3D plot that models a parabola-of-revolution–shaped bottle microresonator. Figure 6 left demonstrates the time evolution of a Gaussian-shaped wave pulse inside of a bottle microresonator. This model corresponds to the behavior of a harmonic oscillator potential.

Visit spsnational.org/jurp to see the entire article

High-Resolution Muography Using a Prototype Portable Muon Telescope

R. Perez,[a)] S. A. Shanto,[b)] M. Moosajee, and S. Cano

Texas Tech University, Department of Physics & Astronomy,
Advanced Particle Detector Laboratory,
1204 Gilbert Drive, Lubbock, Texas 79416-2104, USA

[a)] Corresponding author: raulperezjr.perez@ttu.edu
[b)] sadman-ahmed.shanto@ttu.edu

Abstract. We report on our continued development of a portable muon telescope with excellent angular resolution capable of imaging large archaeological structures in detail. The first prototype (Phase I) consists of four trays of scintillator bars, Winston cones, silicon photomultipliers (SiPMs), readout electronics, and a network of Arduinos to handle data acquisition. Finally, we developed a reconstruction algorithm to create the final image. The cosmic muons produce scintillation photons as they pass through the scintillator bars; these photons are transported by the Winston cones to the SiPMs where they are converted into electrical signals. The electrical signals are then digitized and transmitted to an offline computer for reconstruction. The entire system is mounted on a wheeled cart and can be pointed to target different objects of interest. With Phase I, we are able to reconstruct large objects in two-dimensional space with an angular resolution of 20 mrad with an operating efficiency of 89%.

INTRODUCTION

Muons are elementary particles able to penetrate deep into structures, allowing us to image through very dense material. The muons we interact with are created in the Earth's upper atmosphere from cosmic rays colliding with the nuclei of air molecules. These high-energy collisions result in pions, which often decay into muons and muon neutrinos.[1] The muon flux reaching the Earth's surface is about 10,000 muons per minute per square meter, making them the most abundant cosmic ray particle at sea level.[2] These charged particles lose energy mostly through inelastic collisions in materials. Many of these collisions can take place per given path length, causing substantial energy loss. The energy loss per unit length ($-dE/dx$) is generally given by the Bethe-Bloch formula[3] and is used to describe the density-dependent energy loss in materials. Muon tomography is a technique that uses this fact and the measured muon flux to reconstruct images. Muon tomography has been used to image large objects such as volcanoes, buildings, and ancient archaeological structures for more than 50 years.[4] In his pioneering work, Alvarez searched for hidden structures in an Egyptian pyramid in 1970, thus showing the noninvasive feature of muon tomography and its applications.[5]

The goal of this project is to develop a portable muon telescope that is capable of the best possible angular resolution that is physically attainable. Developing such a system requires an efficient muon detector, communication electronics, and excellent software for reconstructing the muon trajectory. Our first prototype telescope (Phase I) was built at the Advance Particle Detector Lab at Reese Technology Center in the summer of 2019 for training purposes. In this paper, we discuss the performance, detector construction, and results from imaging a local water tower using the Phase-I telescope.

Phase-I Muon Telescope

The Phase-I telescope is mounted on an aluminum frame cart, spanning an area of approximately 90 cm × 180 cm, as shown in Fig. 1(a). The telescope consists of four trays of plastic scintillator bars (Eljen, EJ-200).[6] Each bar has a cross-sectional area of 5 × 5 cm and is 60 cm long. Every other tray is rotated by 90 degrees so that the bars in adjacent trays are perpendicular. Measuring a signal in a pair of consecutive trays allows both x and y position of the incident muon to be inferred. The two pairs of trays give independent x and y measurements and form a track—a parameterization of the muon's trajectory. The two pairs of trays are one meter apart, providing an angular resolution of 20 mrad. The angular resolution depends on the point position resolution of a single bar (14.4 mm) and the separation distance between the two pairs of trays.

Inside each tray, 11 bars are placed parallel to each other and are individually wrapped in reflecting foil to increase the light collection efficiency of the scintillator. Figure 1(b) shows these bars in a single tray during assembly. A SensL (MicroFC-60035-SMT)[7] silicon photomultiplier (SiPM) is optically coupled to a single bar via solid Winston cone,[8] which helps focus scintillation light from the larger cross-sectional area of the bars (5 × 5 cm^2) to the smaller area of the SiPM (36 mm^2).

(a)   (b)   (c)
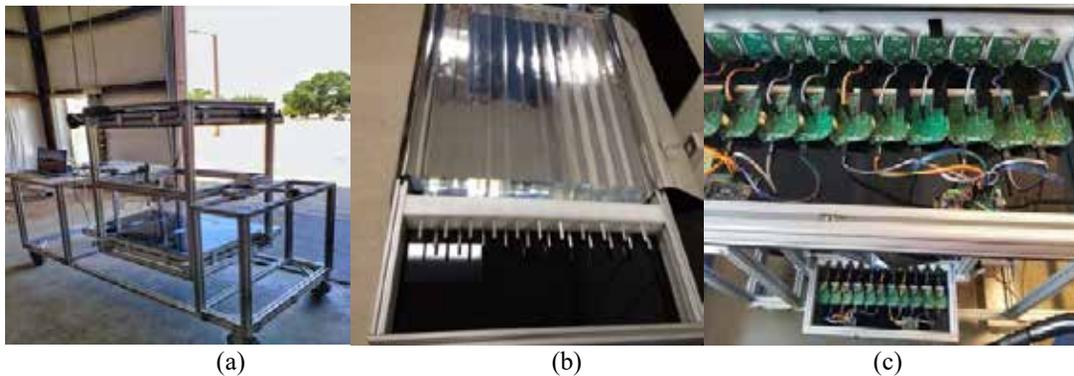
FIGURE 1. (a) The Phase-I muon telescope with top and bottom trays. (b) Scintillator bars positioned in a tray during construction. (c) SiPMs and custom electronics mounted to the bars in top and bottom trays.

Scintillation light is produced as a muon passes through the scintillator, losing ~2 MeV per centimeter. This scintillation light is detected by a SiPM that converts photons into low-voltage pulses. Since the response time of a raw pulse from a SiPM (~100 ns) is three orders of magnitude smaller than the time sensitivity of our readout electronics, we made a custom printed circuit board (PCB) based on MIT's Cosmic Watch, consisting of a dual-channel amplifier (Linear Tech, LT1807),[9] which amplifies and stretches the raw signal. A schematic of our circuit is shown in Fig. 2. The amplified signals from a channel are then sent to an Arduino Nano, which converts them into digital signals. This task is accomplished by a pair of nanos in each tray acting as nodes, communicating with up to six channels at a time. This digitized signal is then transferred to a local computer that aggregates data from all the channels for analysis. The data acquisition software allows continuous online monitoring for data loss or hardware malfunction during a data-taking period.
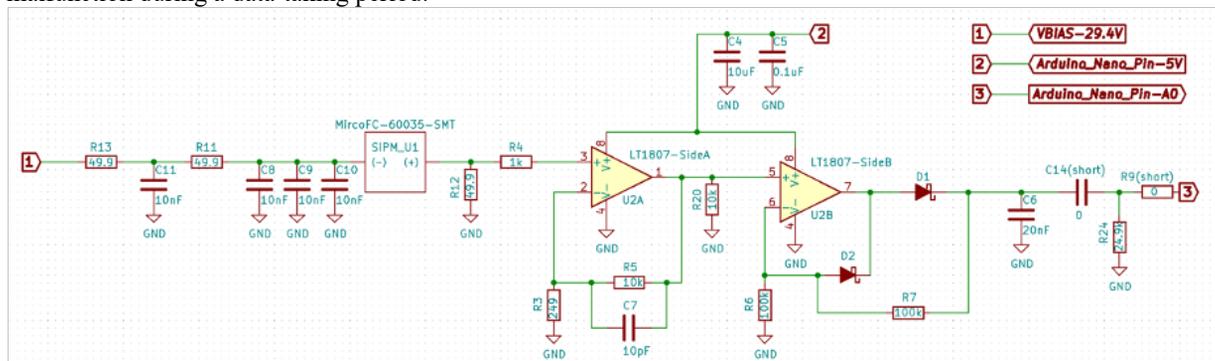
FIGURE 2. Schematic of circuit including SiPM.

The digitized data from a completed run are stored on a local computer for offline analysis. Our analysis requires that a muon pass through each of the four layers within a millisecond. This enables us to record two single space points—$(x, y, z = d)_T$ on the top and $(x, y, z = 0)_B$ on the bottom—from which we can calculate the angle of impact of the muon. We store the number of muons per detected angle and their energy deposits, respectively, which allows us to reconstruct a two-dimensional image of the object of interest.

Water Tower Experiment

Using the Phase-I telescope at Reese Technology Center, we imaged a nearby water tower as our first case study. The telescope was positioned pointing directly at the water tower at 45 degrees (Fig. 3). This configuration was empirically found to be the optimal angle for detecting the midpoint of the tank, which was defined by the location of the telescope stationed in a nearby barracks. To establish the muon flux without obstructions, reference runs were taken pointing the telescope away from the water tower. The water tower has a height and diameter of 43.8 m and 15 m, respectively, with a capacity of 500,000 gallons.
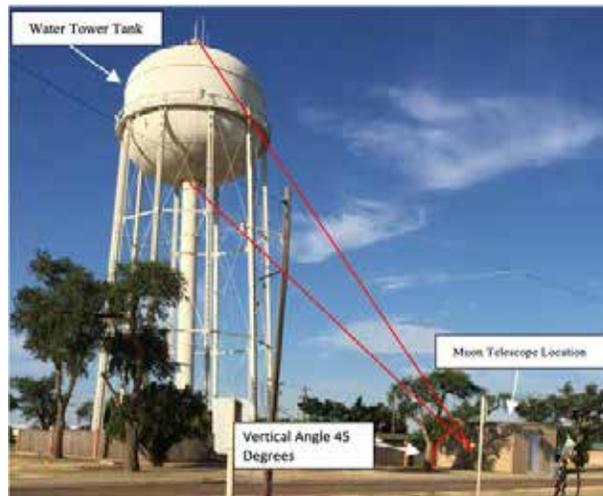
FIGURE 3. Water tower at the Reese Technology Center and the location of the Phase-I muon telescope.

The experiment was conducted over the course of a few months while collecting data each consecutive day for an exposure time of 24 hours. Information on the varying water levels inside the tank throughout the day was provided by Reese Technology Center personnel. A Monte Carlo simulation was created using GEANT4[9,10] that allowed us to model the geometry of our telescope and water tower, as shown in Fig. 4, while also allowing us to simulate how muons interacted with the materials in our models. In order to realistically describe the cosmic muon momentum spectrum, we used the Cosmic Ray Shower Library (CRY).[11] The program CRY is linked with GEANT4, which

(a)   (b)
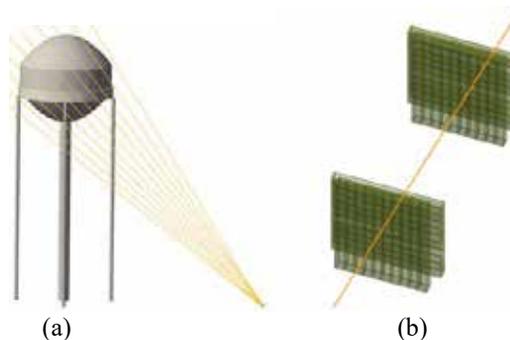
FIGURE 4. (a) Screen capture of detected muon tracks passing through the water tower. (b) Muon track passing through simulated scintillator bars.

allowed us to extract the relevant physical information from the muon paths as they pass through the different geometries. Muons are simulated with random trajectories, and based on whether or not they interact with our telescope model, we can infer what fraction of muons will be detected. Example trajectories of muons detected are shown in Fig. 5(a).

(a)

(b)
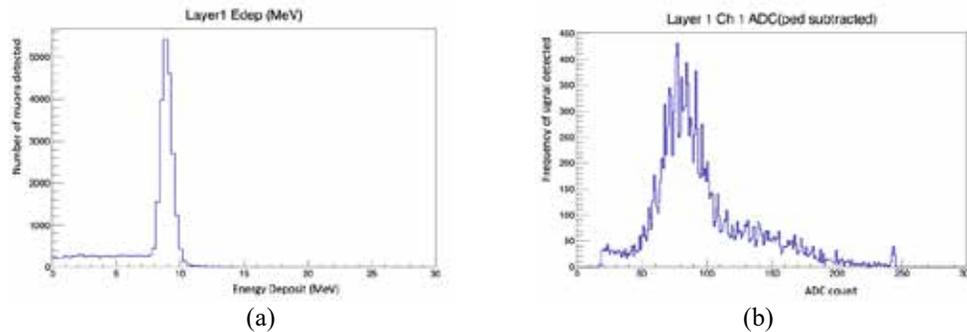
FIGURE 5. (a) Energy loss by muons in a single bar. (b) Measured signal distribution for a single bar in ADC counts.

During the experiment, we collected ~3 million events during each run, with only 5.2% containing enough hits to form a muon track. Image reconstruction uses the muon tracks from both the reference run and the water tower run for the same exposure time. These two datasets contain information on the number of muons detected per a given angle. Taking the ratio between the datasets represents the color, as shown in Fig. 6(a) of our reconstructed 2D image of the water tower with respective horizontal vs. vertical axes. The ratio indicates that there is roughly a 15% loss of muons due to the presence of the water tower. This muon loss represents the muon absorption and scattering when interacting with dense materials. Similarly, we produced the same 2D image using simulated events, as shown in Fig. 6(b). The simulation suggests a 70% loss, compared to 15%. The disagreement between observation and simulation is currently being studied.

(a)

(b)
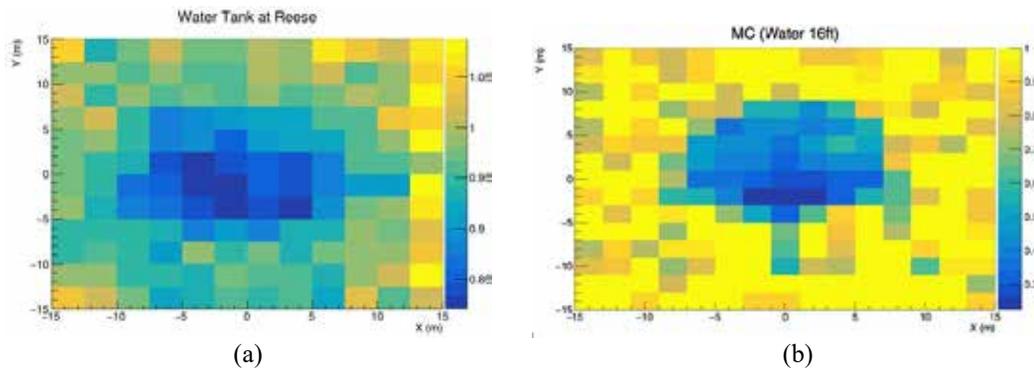
FIGURE 6. (a) 2D image of the water tank from data. (b) 2D image of the water tank from simulation.

CONCLUSIONS

Our experiment shows that we can noninvasively image objects of interest using cosmic muons. The shadow of the water tank observed by our Phase-I telescope capable of an angular resolution of 20 mrad confirms that high-resolution tomography is feasible while providing portability. A comparison between the observed data and the simulation estimates the working efficiency of our telescope to be 89%. The questions of extracting the water level from the images and the disagreement between data and the Monte Carlo simulations are currently being investigated, and improvements to the system are now being implemented. The next data-taking period with the Phase-I telescope will take place this summer with significantly enhanced signal detection efficiency. We are also experimenting with

scintillator fibers as a potential replacement of scintillator bars for finer spatial segmentation. Our goal is to achieve a resolution of 0.5 mrad with the next prototype (Phase II).

REFERENCES

[1] S. Procureur *et al.*, Nucl. Instrum. Methods Phys. Res., Sect. A **878**, 169–179 (2018).

[2] H. Yang *et al.*, Final Technical Report: Imaging a Dry Storage Cask with Cosmic Ray Muons, US DOE, Office of Scientific and Technical Information (2018).

[3] M. Tanabashi *et al.* (Particle Data Group), Phys. Rev. D **98**, 030001 (2018), and 2019 update, available at http://pdg.lbl.gov/2019/reviews/rpp2019-rev-passage-particles-matter.pdf.

[4] H. Gómez *et al.*, Nucl. Instrum. Methods Phys. Res., Sect. A **936**, 14–17 (2019).

[5] L. W. Alvarez *et al.*, Science **167**, 832–839 (1970).

[6] See supplementary material at https://eljentechnology.com/products/plastic-scintillators/ej-200-ej-204-ej-208-ej-212 for properties and chemical compatibility of the Eljen Technology scintillator bars EJ-200.

[7] See supplementary material at https://sensl.com/downloads/ds/PB-Intro_to_SiPM_2_Pages.pdf for properties of the SensL SiPM.

[8] J. A. Aguilar *et al.*, Astropart. Phys. **60**, 32–40 (2015).

[9] See supplementary material at https://www.analog.com/media/en/technical-documentation/data-sheets/18067fc.pdf for properties of the amplifier.

[10] S. Agostinelli *et al.*, Nucl. Instrum. Methods Phys. Res., Sect. A **506**, 250–303 (2003).

[11] C. Hagmann *et al.*, Cosmic-ray Shower Library (CRY), Lawrence Livermore National Laboratory (2012), available at https://nuclear.llnl.gov/simulation/doc_cry_v1.7/cry.pdf.

Calculation of the Magnetostatic Energy in Spin Density Functional Theory

Lórien MacEnulty[1, 2, a)] and David D. O'Regan[1, b)]

[1] *School of Physics, AMBER and CRANN, Trinity College Dublin, The University of Dublin, Dublin 2, Ireland*
[2] *Department of Physics and Astronomy, Drake University, Harvey-Ingham Hall,*
2804 Forest Avenue, Des Moines, Iowa 50311, USA

a) Corresponding author: lorien.macenulty@drake.edu
b) david.o.regan@tcd.ie

Abstract. In density functional theory calculations of materials and molecules, it is conventional to neglect the relativistic magnetostatic contribution of unpaired electron spins to the total energy and potential. For small systems, the magnetostatic contribution to the total energy is negligible, yet it is not obvious that it remains negligible in extended systems with high spin magnetic moment. We make use of a mathematical shortcut, using a fictitious magnetic charge density, to calculate the magnetic field and to determine the degree to which this relativistic effect can be ignored in electronic structure calculations. Using this, we compare the strength of the magnetostatic energy to the electrostatic energy. This ratio is consistently on the order of 10^{-5}, which is on the order of $1/c^2$ in atomic units, as is expected from its formula.

INTRODUCTION

Electron Spin, Magnetization, and Density Functional Theory

Quantum effects give rise to an intrinsic angular momentum or spin, characteristic of all particles, which interacts with external magnetic fields. For collinear spins, unpaired electrons in valence orbitals of atoms contribute to the overall magnetization $\vec{M}$ via linear accumulation of the z-component of their spin-generated magnetic moments:

$$\vec{M} = \frac{-\mu_B}{e}\left(\rho^\uparrow - \rho^\downarrow\right)\hat{M}. \tag{1}$$

Here, ρ^σ is the charge density of electrons of spin σ, $\mu_B = 1/2$ in atomic units is the Bohr magneton, e is the electronic charge, and $\hat{M}$ is the magnetization orientation unit vector.

Density functional theory (DFT), a computational method for calculating quantum properties, allows us to solve the many-body Schrödinger equation indirectly by asserting that the energy may be written as a function of the electron probability density, a function of spatial coordinates.[2] The Kohn-Sham equation, an auxiliary DFT analog to the Schrödinger equation, can incorporate both quantum interactions and relativistic interactions. We are concerned with the latter axis, wherein any relativistic electron-spin-generated magnetostatic energy is considered a higher order relativistic correction to the electrostatic Hartree term. Usually, this term is negligible, although it is known to play a role in determining magnetic domain sizes. The effects and energy scales that typically compete with the magnetostatic energy are the spin-orbit energy and the exchange-correlation magnetic field energy. In systems with high spin magnetic moment, such as in elemental manganese, the term's negligibility is not immediately evident.

The magnetostatic energy term manifests in the many-body electronic Hamiltonian. In this context, we can begin to approximate this corrective term in Kohn-Sham DFT, including relativistic exchange and correlation effects. In our own work, we explore the non-self-consistent energy contribution of this term to the density, not the self-consistent effect. Nonetheless, it is worth recalling the weakly relativistic Hamiltonian for a vanishing applied magnetic field,[3]

$$\hat{H} = \hat{T} + \int d^3r\, [\hat{n}(\vec{r})V_{\text{ext}}(\vec{r})] + \int d^3r \int d^3r' \left[\frac{e^2}{2}\frac{\hat{n}(\vec{r})\hat{n}(\vec{r}')}{|\vec{r}-\vec{r}'|} - 2\pi\,\mu_B^2\,\hat{m}^i(\vec{r})\left(\frac{2}{3}\delta_{ij}\delta(\vec{r}-\vec{r}') + d_{ij}(\vec{r}-\vec{r}')\right)\hat{m}^j(\vec{r}')\right], \tag{2}$$

where $\hat{T}$ is the kinetic energy operator, $\vec{r} - \vec{r}'$ is the source-field displacement, and $\hat{m}(\vec{r})$ is the magnetization density operator. The tensor d_{ij} is defined as[3]

$$d_{ij}(\vec{r} - \vec{r}') = -\frac{1}{4\pi}\nabla_i\nabla'_j\frac{1}{|\vec{r}-\vec{r}'|} + \frac{1}{3}\delta_{ij}\delta(\vec{r} - \vec{r}'). \tag{3}$$

For the purposes of this investigation, we are primarily interested in the μ_B^2 term of Eq. (2) but refer the reader to Refs. 3 and 4 for further clarification on the constituents of the previous Hamiltonian.

METHODS

A versatile algorithm was built to systematically determine the magnetostatic energy contribution U_M of valence electron spin given a static magnetization $\vec{M}$. The systems with which we are concerned have no free current density. We thus derive the curl of the magnetic field strength $\vec{H}$ to be zero, so effectively, $\vec{H}$ may be written as the negative gradient of a scalar potential, which we will call the scalar magnetic potential ϕ_M. To obtain this ϕ_M, we start by finding the fictitious magnetic charge density ρ_M, an exclusively mathematical object simulating the north and south poles of magnetic bodies, defined as

$$\rho_M = -\nabla \cdot \vec{M}. \tag{4}$$

We then extract a density table as a function of coordinates. The Fast Fourier Transform method translates the density table into reciprocal space. We construct the reciprocal potential $\widetilde{\phi_M}(\vec{k})$ by dividing terms in the reciprocal density table by the inverse k^2, thereby employing the Fourier space equivalent of Poisson's equation for magnetism:[5]

$$\widetilde{\phi_M}(\vec{k}) = \frac{\widetilde{\rho_M}(\vec{k})}{k^2}. \tag{5}$$

It is expected that $\widetilde{\rho_M}$ averages to zero inside the cell in source-free magnetism, so the limit of $\widetilde{\phi_M}(\vec{k})$ as $k \to 0$ is separately set to zero in the program. The Inverse Fourier transform of the reciprocal potential table yields ϕ_M, and thus we attain $\vec{H} = -\nabla\phi_M$. The magnetostatic energy U_M is then obtained via the volume integral in Eq. (6), which is preceded by $\mu_0 = 4\pi\alpha^2$ in atomic units, where $\alpha = \frac{1}{c} \approx \frac{1}{137}$ is the fine structure constant:[6]

$$U_M = \int_V \frac{\mu_0}{2}\left(M^2 + \vec{H} \cdot \vec{M}\right) dV. \tag{6}$$

We applied the algorithm to a variety of atomic systems modeled by both theoretically and computationally derived
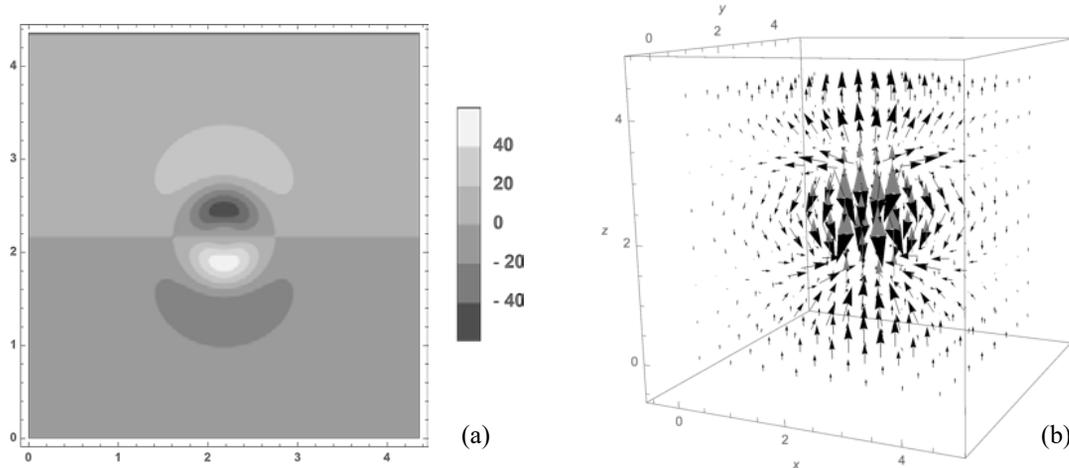
FIGURE 1. (a) Magnetic charge density ρ_M in a.u. of Mn $3d$ orbital resultant of magnetization pointing in z-direction (x-z plane, $y = \frac{a}{2}\, a_0$). (b) Vector field of magnetization $\vec{M}$ (gray) and magnetic field strength $\vec{H}$ (black) of Mn $3d$ orbital. Values in a.u.

electron densities and enclosed in various crystal lattices. One model system investigated comprised a single manganese atom, the elemental transition metal with the highest spin magnetic moment, at the center of a cube of lattice constant 4.35 a_0. Assuming the spin is collinear, Mn adopts a total magnetic moment along the quantization axis $\hat{z}$ of 5 μ_B due to its five unpaired electrons in the $3d$ valence shell. The magnetization under consideration, of similar form to Eq. (1), is thus

$$\vec{M}_{\text{Mn}}(r) = \frac{5}{2}\left[\frac{4}{27\sqrt{10}}\left(\frac{Z_{\text{eff}}}{3a_0}\right)^{\frac{3}{2}}\left(\frac{r*Z_{\text{eff}}}{a_0}\right)^2 \exp\left[\frac{-r\cdot Z_{\text{eff}}}{3a_0}\right]\right]^2 \hat{z}, \quad (7)$$

where r is the distance from the origin, set at (0,0,0), and Z_{eff} is the effective nuclear charge of Mn.

RESULTS AND DISCUSSION

Figure 1(a) shows the magnetic charge density generated by a single, highly idealized Mn atom at the center of a cube. As expected, we observe regions of opposite sign corresponding to the south and north poles of the magnetization field. Figure 1(b) is a three-dimensional vector field plot of both $\vec{M}$ and $\vec{H}$ as functions of Cartesian coordinates. The flux of $\vec{H}$ appears to oppose that of $\vec{M}$ amidst the approximate domain of the Mn 3d orbital. This is precisely the behavior we expect to see mathematically and provides a degree of validation that the algorithm works as expected. The magnetostatic energy was converged as a function of increasing interpolation order and number of points.

The magnetostatic energy of this system converges to a value of around -0.0220 a.u. per atom. Across all systems, it is exclusively the energy contribution of the $\vec{H} \cdot \vec{M}$ term, denoted $U_{H \cdot M}$, that varies with orientation, whereas the M^2 volume integral remains constant. By contrast, the electrostatic energy of the same atomic system is approximately 609 a.u. per atom. The ratio of magnitudes of magnetostatic to electrostatic energy contributions is consistently on the order of 10^{-5} across the various atomic systems tested, including the cubic system and an FCC lattice system (both primitive and conventional unit cells, lattice constant $4.35\sqrt{2}\,a_0$). This ratio is physically plausible since the magnetostatic term is scaled by a factor of μ_0, which is proportional to the square of the fine structure constant.
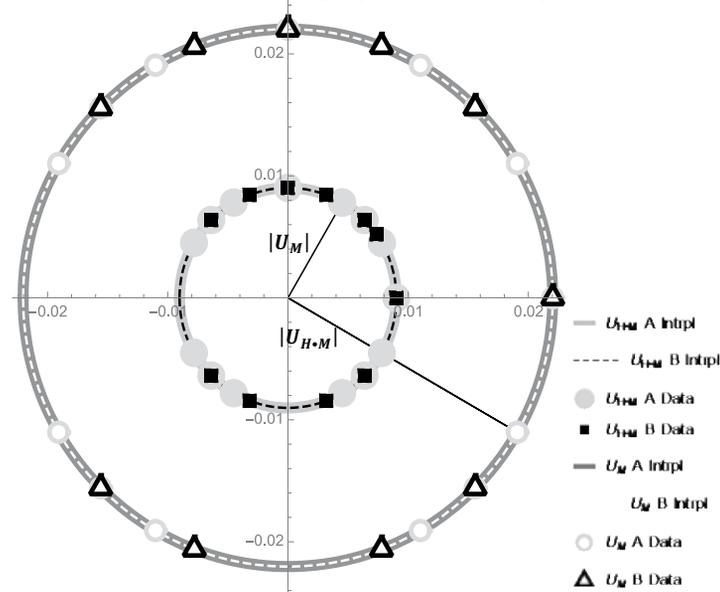
FIGURE 2. Magnetostatic energy in a.u. of single Mn atom cubic system as a function of $\vec{M}$ orientation. Distance from the origin to the point is $|U_M|$ or $|U_{H \cdot M}|$ (see legend). Legend entries denoted "A" signify $\vec{M}$ orientation in the x-y plane ($M_z = 0$); those denoted "B" are beholden to the plane generated by vectors {0,0,1} and {1,1,1}. "Intrpl" = interpolated function of circle.

This cubic system was then immersed in a crystalline lattice environment and subjected to computational testing for an expected magnetostatic anisotropy. The orientation of $\vec{M}$ was varied in order to measure its effect on the magnitude of the magnetostatic energy. In crystalline lattice environments, the distance between atoms along a given vector is not generally the same, and thus variation of the dipole orientation would enlighten us to the existence of a discernible anisotropy contribution.[1] As demonstrated in Fig. 2 and validated across multiple other orientations of $\vec{M}$, the cubic system in question exhibits a subtle, even negligible energy variation with orientation angle; the magnitude

of $\vec{U}_M$ remains close to constant despite the change in orientation of $\vec{M}$.

CONCLUSIONS

The spin-generated magnetostatic contribution to the total energy of atomic systems is small, consistently on the order of $1/c^2$ times its electrostatic counterpart. We cannot conclude definitively that DFT practitioners may exclude the magnetostatic dipole energy, noting, however, that we did not investigate a situation in which the dipole and spin-exchange-correlation magnetic field energies compete. This approach demonstrates the value of the magnetic charge density as an interesting stratagem for computing the properties of magnetic fields. We hope to inspire further investigation of the magnetic charge density in the context of approximate functional construction for relativistic DFT, where it may be useful for the study of systems with less localized spin densities or embedded in inherently anisotropic crystal structures.

ACKNOWLEDGMENTS

REFERENCES

[1] J. Coey, *Magnetism and Magnetic Materials* (Cambridge University Press, Cambridge, England, 2010), p. 66, 168.
[2] C. Fiolhais, F. Nogueira, and M. Marques, *A Primer in Density Functional Theory*, edited by C. Fiolhais, F. Nogueira, and M. A. L. Marques, Lecture Notes in Physics Vol. 620 (Springer Verlag, Berlin, Heidelberg, 2003), pp. 1–5.
[3] C. Pellegrini, T. Müller, J. K. Dewhurst, S. Sharma, A. Sanna, and E. K. U. Gross, Phys. Rev. B **101**, 144401 (2020).
[4] H. J. F. Jansen, Phys. Rev. B **38**, 8022 (1988).
[5] J. Mathews and R. Walker, *Mathematical Methods in Physics*, 2nd ed. (Addison-Wesley Publishing Co., Menlo Park, CA, 1970), pp. 239–245.
[6] D. Griffiths, *Introduction to Electrodynamics*, 4th ed. (Pearson, New York, 2017), p. 330.

Analysis of Physical and Structural Properties of Alkali Oxide–Modified Tellurite Glasses

Martha Jesuit,[1, a)] Michael Packard,[1] Makyla Boyd,[1] Nagia S. Tagiara,[2] Efstratios I. Kamitsos,[2] Oliver Alderman,[3] Chris Benmore,[4] Alex Hannon,[3] Matthew Appler,[1] and Steve Feller[1, b)]

[1]Department of Physics, Coe College, Cedar Rapids, Iowa 52402, USA
[2]National Hellenic Research Foundation, Athens 116 34, Greece
[3]Rutherford Appleton National Laboratory, Didcot OX11 0QX, England, UK
[4]Argonne National Laboratory, Lemont, Illinois 60439, USA

a) Corresponding author: mrjesuit@gmail.com
b) sfeller@coe.edu

Abstract. Glasses in the system $x\,M_2O \cdot (1-x)\,TeO_2$ ($0 \le x \le 0.25$), where M = Li, Na, K, Rb, Cs, were made by melting in platinum crucibles. Various quenching methods were used to make each glass because some glasses require extremely rapid cooling. Physical properties such as the glass transition onset temperature (T_g) and density (ρ) were measured. In order to explore the short-range structure in these glasses, Raman spectroscopy, infrared spectroscopy, and high-energy x-ray diffraction were used. These experiments on tellurite glasses were performed to find correlations between the physical and structural properties.

INTRODUCTION

Pure tellurium dioxide glass was once perceived as impossible to make in bulk quantities. The only methods of forming this glass were by roller quenching or aero-levitation, making only hundredths of a gram of sample at a time.[1] However, Tagiara et al. developed the new intermittent quenching technique (IQ technique), which can produce pure amorphous TeO_2 in gram quantities.[2] The IQ technique involves dipping the bottom of the crucible in and out of water rapidly in a controlled manner. This hard-to-make glass has shown unusual physical and chemical properties in comparison to other oxide glasses, which makes this a very sought-after material for research. These characteristics include a high refractive index and dielectric constant, low phonon energy and melting temperature, excellent third-order nonlinear optical properties, and a large thermo-optic coefficient.[3–8] Based on these data, tellurium dioxide glasses are favorable materials for numerous optical devices, such as erasable optical recording media,[9] optical switching devices,[10] or lenses and fibers for near-infrared applications. However, since there still exists disagreeing results of the coordination number of tellurium, n_{TeO}, there is still much to test to find an agreement on what the data are conveying. The coordination number of Te and its number of bridging oxygens is denoted as $Q_m{}^n$, where the index n gives the number of bridging oxygens bonded to the central atom and m gives the coordination number.[11] The resulting $Q_m{}^n$ for each tellurite polyhedron can be found in Fig. 1.

Studies from various techniques such as neutron diffraction[1] (ND) and Raman spectroscopy[12] show that pure amorphous TeO_2 has a mixture of approximately two-thirds TeO_4 units and one-third TeO_3 trigonal pyramids, but this answer still remains uncertain. One nuclear magnetic resonance (NMR) study[13] has not found any evidence of TeO_3 units, which differs from another NMR result[14] where TeO_3 or TeO_{3+1} units were recorded (where TeO_{3+1} refers to 4 coordination with one longer bond). In addition, a recent high-energy x-ray diffraction study of TeO_2 glass has shown the presence of $Q_4{}^4$ units.[15] TeO_3 units may show the existence of terminal oxygens in the glass structure and cause a decrease in coordination number. A 2000 study from McLaughlin et al. suggests that only $Q_4{}^4$ and $Q_4{}^3$ exist of the possible 4-

coordinated tellurium, because species like Q_4^2 would require a change in the oxidation state of tellurium, which was not observed.[11] This is mostly consistent with the NMR study by Marple et al., which found the coordination number to be 3.89.[14] Although it is often assumed that Te in pure a-TeO$_2$ is 4 coordinated, analogous to crystalline polymorphs of TeO$_2$, the average n_{TeO} decreases as the amount of modifier is added through the intermediate formation of TeO$_{3+1}$ until the tellurium is entirely 3 coordinated.[1] The lowering of the coordination number can be seen as less than 4 for glasses with as little as 1 mol % modifier alkali oxide. The active lone pair of electrons on the tellurium atoms induces a pseudo-trigonal bipyramid structure in α-TeO$_2$. This can suggest that a-TeO$_2$ is composed of asymmetric [TeO$_4$] units with two short (1.882 Å) equatorial and two long (2.177 Å) axial Te-O bonds.

EXPERIMENTAL PROCEDURES

FIG. 1. Left: Q_m^n, where $m = 3,4$ identifies the total number of oxygen bonded to the tellurium atom and $n = 0–4$ is the number of bridging oxygen bonded to the tellurium atom.[11] Right: Tellurium dioxide crystal (left). Pure tellurium dioxide glass made with IQ technique (right).

All glasses for x-ray studies at the Advanced Photon Source (APS) at Argonne National Lab were made using Sigma Aldrich chemicals of ≥99% purity (see Fig. 1 for TeO$_2$). Lithium, sodium, and potassium tellurite glasses were formed up to 25 mol % modifier by heating the alkali carbonate and tellurium dioxide mixture in a platinum crucible for 10 min at 800ºC twice. After the first melt, the contents were cooled outside of the furnace. Once cooled the weight loss was recorded, subtracting off the crucible weight. The roller-quenched glasses were ideal for loading into the capillaries for x-ray diffraction. Once the second melt had finished, it was immediately poured into a stainless-steel roller quencher, which yielded mostly glass. This resulted in thin transparent yellow pieces of glass. Half of the glass made was stored in a nitrogen-sealed glove box and the other half was directly taken to measure T_g. The glasses stored in the glove box were eventually taken to the APS for high-energy x-ray diffraction measurements.

Glasses for infrared and Raman spectroscopy at the National Hellenic Research Foundation were made using Sigma Aldrich chemical of ≥99% purity. Glasses modified with M$_2$O (M=Li, Na, K, Rb, Cs) were made from 5–25
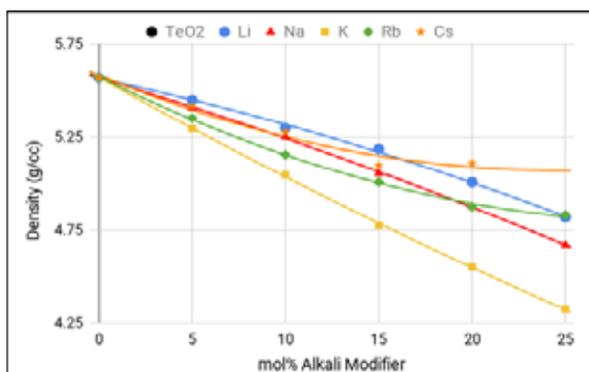
FIGURE 2. Densities of alkali tellurite glasses vs. mol % of alkali oxide.
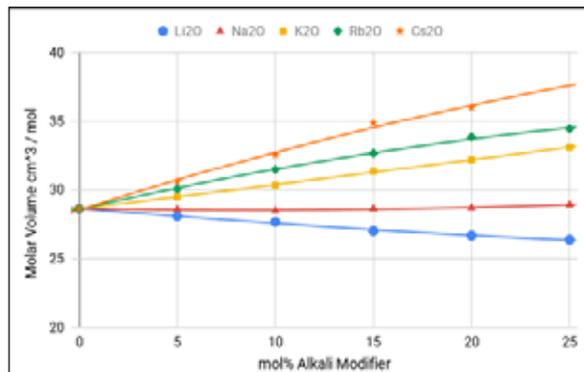
FIGURE 3. Molar volume of alkali tellurite glasses vs. mol % of alkali oxide.

mol % of modifier oxide. However, Cs_2O-TeO_2 could not be made at 25 mol % modifier. These glasses were melted in a platinum crucible for 15 min at 1000°C for M=Li, Na, Rb, Cs and 15 min at 800°C for M = K. Then the contents cooled in the crucible without any sort of quenching aid. Glasses were easily formed and came out of the crucible in a coinlike shape, which was most suitable for infrared and Raman polishing and signal gathering.

Differential scanning calorimetry (DSC) was used to find the glass transition onset temperature. Samples were ground into a powder and crimped tightly into an aluminum pan while in a nitrogen glove box. DSC was then performed at 40°C/min in air on all samples immediately after formation to avoid water absorption. Glass onset temperature (T_g) and crystallization temperature (T_x) were measured on a Perkin Elmer DSC 7. DSC results were reported at the 2019 International Congress on Glass.
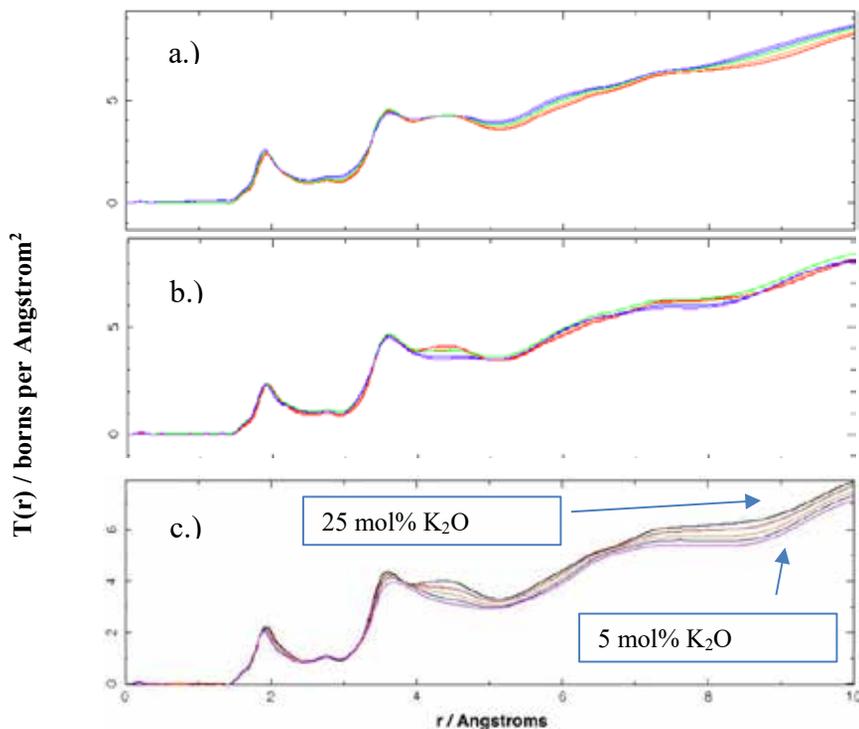
FIGURE 4. Total correlation functions from x-ray diffraction analysis: (a) Li_2O-TeO_2, (b) Na_2O-TeO_2, and (c) K_2O-TeO_2. The following was observed: Short Te−O bonds (1.85−1.88 Å) and a longer Te−O bond and O-O bond at (2.5−2.9 Å). The different colored lines represent the various mol % of alkali oxide in the glass. The alkali content increases such that 5 mol % of alkali oxides is the bottom line and 25 mol % is the top line, as shown in Fig. 4c.

Density was found using a Quantachrome Ultrapyc 2000e automatic helium pycnometer. Pellets of aluminum were loaded into a calibrated sample chamber of known volume. Helium was introduced and the pycnometer measured the volume of the sample 15 times. Then the last five measurements were averaged together to find the average volume of the sample. Since the density of aluminum is known, 2.698 g/cm^3,[16] we used this as our reference of 15 runs of aluminum, 15 runs of our glass sample, and another 15 runs of aluminum. Our average densities can be found in Fig. 2, while molar volumes are shown in Fig. 3.

High-energy x-ray diffraction measurements were made at beamline 6-ID-D of the Advanced Photon Source at Argonne National Lab. Roller-quenched samples of M_2O-TeO_2 (M=Li, Na, K) glasses were powdered with a mortar and pestle and loaded into thin walled borosilicate glass capillaries of 1.5 mm internal diameter. The diffraction pattern was recorded using an incident beam energy of 100.36 keV and a flat-panel Varex 4343CT detector (2880 × 2880 pixels of 150 × 150 μm) for a total of 15 min. The capillary was also measured for the background subtraction. The sample-to-detector distance of 346.9 mm was calibrated by measurement of a sample of NIST standard CeO_2. Each sample was tested for a total of 135 min. The powder patterns from the x-ray diffraction were obtained using the Fit2D program. All tests for each sample were averaged together and the powder pattern was then read. Once the powder patterns were made, the files were converted to an .XYE file and uploaded to GudrunX[17] to make further corrections

to the x-ray data, for example, absorption, background, fluorescence, density, abundance, and calibration factors. X-ray structure factors obtained using GudrunX were then Fourier transformed to obtain the total correlation functions using software provided by Dr. Alex Hannon. The total correlation function was then found to measure the bond lengths between tellurium to oxygen, tellurium to tellurium, and oxygen to oxygen in every M_2O (M=Li, Na, K) modified tellurite glass, see Fig. 4.

RESULTS AND DISCUSSION
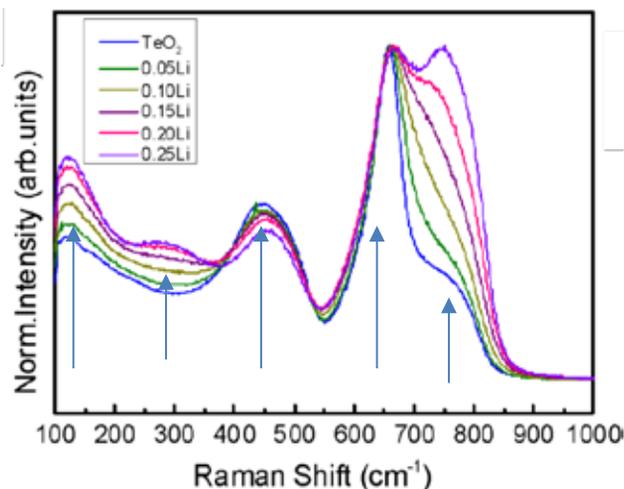
FIGURE 5. Raman spectra for Li-TeO$_2$ glasses.

Molar volume is shown in Fig. 4. This graph makes sense, because as the modifier cation gets larger, the molar volume increases. The total correlation functions are consistent with a distribution of Te-O bond lengths over a very wide range. The coordination of tellurium is consistent with 4. Since there is a wide distribution, this can be thought of as 3+1.

Raman spectra for a representative glass system (Li) are shown in Fig. 5. The first peak at around 120 cm^{-1} is known as a notch filter artifact. The second set of peaks at around 295 cm^{-1} is probably related to Li+ motion. Also, network deformations are expected around this frequency range. The peak at around 450 cm^{-1} is the symmetric stretching/bending vibrations of Te-O-Te bridges. At 660 cm^{-1} the stretching of TeO$_4$ units is observed. Scattering above 700 cm^{-1} is due to the asymmetric stretching of the Te-O-Te bridges connecting tellurite units. The stretching of the TeO$_3$ units formed by adding the modifier oxide, Li$_2$O, to TeO$_2$ content was seen.
Infrared spectra are not shown here due to space limitations and will be reported at a future Glass and Optical Material Division meeting of the American Ceramic Society.

CONCLUSIONS

Alkali tellurite glasses were studied by XRD, Raman spectroscopy, infrared spectroscopy, and molar volume determination. The results form a structural picture in which tellurium was found to be 4 coordinated in a form likely of three short Te-O bonds and one longer Te-O bond. As alkali oxide modifies the glass, nonbridging oxygens are created at the expense of bridging oxygens. The present XRD results confirm previous NMR and high-energy x-ray diffraction studies where the coordination of tellurium was found to be near 4 in TeO$_2$ glass.[13,14] As the glass is modified, the tellurium changes its coordination number from 4 to 3.

ACKNOWLEDGMENTS

REFERENCES

1. E. Barney, A. Hannon, D. Holland, N. Umesaki, M. Tatsumisago, R. Orman, and S. Feller, J. Phys. Chem. Lett. **4**, 2312–2316 (2013).
2. N. S. Tagiara, D. Palles, E. D. Simandiras, V. Psycharis, A. Kyritis, and E. I. Kamitsos, J. Non-Cryst. Solids. **457**, 116–125 (2017).
3. J. E. Stanworth, Nature **169**, 581–582 (1952); J. E. Stanworth, J. Soc. Glass Technol. **38** 425–435 (1954).
4. H. Bürger, W. Vogel, and V. Kozhukharov, Infrared Phys. **25**, 395–409 (1985).
5. M. J. Weber, J. Non-Cryst. Solids. **123**, 208–222 (1990).
6. E. M. Vogel, M. J. Weber, and D. M. Krol, Phys. Chem. Glasses **32**, 231–254 (1991).
7. R. A. H. El-Mallawany, *Tellurite Glasses Handbook: Physical Properties and Data* (CRC Press, Boca Raton, FL, 2002).
8. T. Honma, N. Ito, and T. Komatsu, J. Am. Ceram. Soc. **93**, 3223–3229 (2010).
9. K. Kimura, Jpn. J. Appl. Phys. **28**, 810–813 (1989).
10. H. Nasu, O. Matsushita, K. Kamiya, H. Kobayashi, and K. Kubodera, J. Non-Cryst. Solids **124**, 275–277 (1990).
11. J. C. McLaughlin, S. L. Tagg, J. W. Zwanziger, D. R. Haeffner, and S. D. Shastri, J. Non-Cryst. Solids **274**, 1–8 (2000).
12. A. G. Kalampounias and S. Boghosian, Vib. Spectrosc. **59**, 18 (2012).
13. M. N. Garaga, U. Werner-Zwanziger, J. W. Zwanziger, A. DeCeanne, B. Hauke, K. Bozer, and S. Feller, J. Phys. Chem. C **121**, 28117 (2017).
14. M. A. T. Marple, M. Jesuit, I. Hung, Z. Gan, S. Feller, and S. Sen, J. Non-Cryst. Solids **513**, 183–190 (2019).
15. O. L. G. Alderman, C. J. Benmore, S. Feller, E. I. Kamitsos, E. D. Simandiras, D. G. Liakos, M. Jesuit, M. Boyd, M. Packard, and R. Weber, J. Phys. Chem. Lett. **11**, 427–431 (2020).
16. Emsley, J., *The Elements*, 3rd ed. (Oxford University Press, Oxford, England, 2000), p. 18.
17. A. K. Soper and E. R. Barney, J. Appl. Crystallogr. **44**(4), 714–726 (2011).

A Pedagogical Model of CO$_2$ and O$_2$ Atmospheric Abundances and Tree Population due to Human Population

Mckayla Benner

Department of Physics, Southern Nazarene University, Bethany, Oklahoma 73008, USA

Abstract. A pedagogical model of the effects of human population on the global tree population and the atmospheric abundances of carbon dioxide and oxygen is provided, which, though too simple to be precise, offers meaningful insights with the virtue of being solvable by analytical means using only elementary calculus.

Introduction

This paper presents a model ecosystem of human and tree populations living in an atmosphere of carbon dioxide and oxygen. It addresses the effects of a growing human population and a declining tree population on the CO$_2$ and O$_2$ abundances. Full disclosure requires acknowledging the model's oversimplified nature. It is to climatology what frictionless ramps and circular planetary orbits are to mechanics—idealized models intended to illustrate strategy over precision. It provides a pedagogical stepping-stone toward more realistic models.

The dynamics of greenhouse gases and their effects on climate are well studied.[1] Thus our simple model offers no new climatology results. Rather, it offers experience in thinking about issues that arise in such models and can be solved analytically using only introductory calculus.

Model

Let t denote time, with $t = 0$ in the year 1500, because we are interested in the industrial era that followed. Our calculations were done in 2018, or $t = 518$ yr. Let $P(t)$ denote the human population in number of individuals; $C(t)$ and $O(t)$ the atmospheric oxygen abundance in tons, respectively. For boundary conditions we borrow data from several authors: $P(0) \equiv P_o$ = world human population in 1500 = 0.4×10^9;[2] global population in 2018 = $P(518$ yr$)$ = 7.6×10^9 persons;[2] from Wolchover,[3] $P(\infty) \equiv P_\infty$ = human population at global saturation (carrying capacity) = 20×10^9;[3] from Amos[4] and Bolton,[5] T_o = tree population in 1500 = 6×10^{12}, and $T(518$ yr$)$ = 3×10^{12} trees. Amos's data[4] places the present tree loss rate between 10 billion and 15 billion trees annually[4]:

$$\left[\frac{dT}{dt}\right]_{2018} = -15\{10\} \times 10^9 \text{ trees/yr}$$

In our model we take the 15 billion value, but in calculations that depend on this rate we include in brackets { } for comparison results for the 10 billion annual loss. For the reader's reference, initial conditions and other relevant constants are gathered in Table 1.

Turning to the rate equations, the human population growth rate is proportional to the current population and to the difference between the present and saturation levels; hence

$$\frac{dP}{dt} = P\lambda\left(1 - \frac{P}{P_\infty}\right) \tag{1}$$

with rate coefficient λ.

The tree population declines due to human-caused deforestation at a rate proportional to P. For several decades the human deforestation rate has been on the order of an acre per second.[6] Since human deforestation dominates over natural tree death, for the tree population rate equation we write

$$\frac{dT}{dt} = -(\mu P)T \tag{2}$$

with rate coefficient μ.

Initial human population:	$P_o = 0.4 \times 10^9$ persons
Carrying capacity:	$P_\infty = 20 \times 10^9$ persons
Fraction of carrying capacity at $t = 0$:	$\rho = 0.02$
Initial tree population:	$T_o = 6 \times 10^{12}$ trees
2018 tree population:	$T(518) = 3 \times 10^{12}$ trees
2018 tree loss rate:	$[dT/dt]_{2018} = 10 - \{15\} \times 10^9$ trees/yr
Human population rate constant:	$\lambda = 0.0109/$ yr
Human-caused tree loss rate constant:	$\mu = 1.06 \times 10^{-13}/$person-yr
Rate const., O_2 production by trees:	$k_1 = 0.13$ T/tree-yr
Rate const., O_2 consumption by people:	$k_2 = 1.8 \times 10^{-4}$ T/person-yr (breathing only)
	12.5 T/person-yr (including machines)
Rate const., CO_2 people & machines:	$k_3 = 11$ T/person-yr
CO_2 absorbed per tree per year	$k_4 = 0.024$ tons/tree-yr
$\gamma \equiv \mu P_\infty / \lambda$	$\gamma = 1.2 \{0.8\}$

Humans and their machines produce carbon dioxide with rate coefficient k_3, while trees consume carbon dioxide with rate coefficient k_4. Neglecting other sinks of carbon dioxide (such as the ocean) because we restrict our study to the effects of trees only, we write

$$\frac{dC}{dt} = k_3 P - k_4 T \tag{3}$$

Oxygen is produced by trees with rate coefficient k_1 and is consumed by people and their machines with rate coefficient k_2; hence

$$\frac{dO}{dt} = k_1 T - k_2 P \tag{4}$$

Eqs. (1)–(4) are schematically represented in Fig. 1.
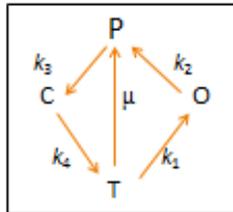
FIG. 1. CO_2 and O_2 flow diagram described by our model's rate equations, which includes human population P, tree population T, atmospheric carbon dioxide abundance C, and oxygen abundance O. Rate coefficients are denoted on the directed lines.

In general the rate coefficients are not constants. For instance, in 1967 the human population growth rate coefficient λ exceeded 2%/yr, but by 2018 it dropped to 1.09%/yr. Thus for maximum realism one should solve Eqs. (1)–(4) numerically, stepping through time slices of duration Δt with elapsed time $t_n = n\Delta t$ (n is a non-negative integer). For example, Eq. (1) would become

$$P(t_{n+1}) = P(t_n) + (\Delta t)\lambda(t_n)P(t_n)\left[1 - \frac{P(t_n)}{P_\infty}\right] \tag{5}$$

However, because we seek an illustrative analytic solution, we approximate all the rate coefficients as constants. For their values we borrow published data: The human population growth rate in 2018 is $\lambda = 1.09\%/\text{yr}$;[2] the tree loss rate coefficient μ can be estimated from Eq. (2) using contemporary values of Amos[4]:

$$\mu = \left[\frac{1}{TP}\frac{dT}{dt}\right]_{2018} = 1.06 \times 10^{-13}/\text{person} - \text{yr}$$

From Ref. [7] we obtain k_1 = oxygen production rate per tree per year = 260 lb/tree-yr = 0.13 tons/tree-yr; and from Ref. [8], k_2 = oxygen consumed per person (breathing only) per year = 0.17 kg/person-yr = 1.8×10^{-4} tons/person-yr (the oxygen consumption of machines will be addressed later); k_3 = annual CO_2 production (in 2018) by humans and their machines = 11 tons/person-yr;[9] from New York State University data,[10] k_4 = CO_2 absorbed by one tree per year

= 48 lb/tree-yr = 0.024 tons/tree-yr.[10] The coefficients k_1 and k_3 are determined by biology and are essentially constant on human timescales. In contrast, k_2 and k_3 depend on—and are dominated by—technology.

Consider what must happen among the rate coefficients in order to have equilibrium between the CO_2 and O_2 abundances. Setting their rates of change equal to zero, Eqs. (3) and (4) require the k_3 equilibrium value k_{3o} to satisfy

$$k_{3_o} = \frac{k_2 k_4}{k_1} = 0.067 \text{ lb/person} - \text{yr} \tag{6}$$

But in 2018, $k_3 = 11$ tons/person-yr, greater than our equilibrium value by a factor of 328,400. This suggests that humanity's relationship with the atmosphere may be unsustainable.

For breathing only, each person needs about 1.8×10^{-4} tons of oxygen per year.[8] Each tree produces about 0.13 tons/yr of oxygen.[7] Thus each tree can supply N persons with just enough oxygen for breathing, where

$$N k_2 = k_1 \tag{7}$$

which with our assumed value of k_1 and k_2 gives $N \approx 716$—one tree can supply 716 people with just enough oxygen necessary for life.[11] The 2018 tree population is about 3 trillion,[4,5] which means that with these numbers, the present tree population by itself can support about 4.4 billion people—about half the current population. Clearly our model is too simple; for example, we neglect photosynthesis of other plants and ocean phytoplankton, and these estimates do not include oxygen consumed in burning fossil fuels. But within the world described by our model, each tree can support 716 people, so in this model a critical time t_c in the human–ecosystem relationship occurs when

$$\frac{T(t_c)}{P(t_c)} = 716 \tag{8}$$

We next derive expressions for $T(t)$ and $P(t)$.

Solutions to Rate Equations

Equation (1) can be integrated by separation of variables, which gives

$$P(t) = \frac{P_o P_\infty e^{\lambda t}}{P_\infty - P_o + P_o e^{\lambda t}} \tag{9}$$

If $P_o \ll P_\infty$, then

$$P(t) \approx \frac{P_o e^{\lambda t}}{1 + \rho e^{\lambda t}} \tag{10}$$

where $\rho \equiv P_o / P_\infty$ denotes the fraction of population capacity reached in the year 1500. With our numbers, $\rho = 0.02$.

Using Eq. (10) in Eq. (2) allows another separation of variables, yielding

$$T(t) = T_o \left(\frac{1 + \rho e^{\lambda t}}{1 + \rho} \right)^{-\gamma} \tag{11}$$

where $\gamma \equiv \mu P_\infty / \lambda = 1.2 \{0.8\}$. Since $\rho << 1$ then

$$T(t) \approx T_o \left(1 + \rho e^{\lambda t}\right)^{-\gamma} \tag{12}$$

For sufficiently large times, when $\rho e^{\lambda t} >> 1$, even though $\rho << 1$, Eqs. (14)–(12) become $T(t) \approx T_o \rho e^{-\gamma \lambda t}$, an exponential decline in the tree population with half-life $t_{1/2} = \frac{\ln 2}{\gamma \lambda} = 53$ yr {79 yr}. To examine the early behavior of $T(t)$, expand the right-hand side of Eq. (12) in a Taylor series about $t = 0$ and approximate $1 + \rho \approx 1$. These steps result in

$$T(t) \approx T_o \left(1 - \rho \gamma \lambda t + \frac{1}{2} \rho \gamma^2 \lambda^2 t^2 + \cdots \right) \tag{13}$$

Since $\gamma \lambda = \mu P_\infty$, Eq. (13) can alternatively be written

$$T \approx T_o \left(1 - \rho \mu P_\infty t + \frac{1}{2} \rho (\mu P_\infty)^2 t^2 + \cdots \right) \tag{14}$$

where $\mu P_\infty \sim 10^{-3}$/yr and $\rho = 0.02$. Equation (13) shows a linear decline in trees at times shortly after the year 1500. When did nonlinearity in Eq. (14) become apparent? Compare Eq. (13) to the Taylor series expansion of a function $f(t)$ to second order, where $f(0) = 1$. The quadratic term becomes apparent when

$$\frac{t^2}{2} f''(0) = \alpha \tag{15}$$

where α is just large enough to be detectable. If $f(t) = T(t)/T_o$, then Eq. (15) gives

$$t = \frac{1}{\mu P_\infty} \sqrt{\frac{2\alpha}{\rho}} \approx \sqrt{\alpha} \times 10^4 \text{ yr} \tag{16}$$

If nonlinearity is detectable when α is, say, one-tenth of one percent, then in our model $t = 316$ yr, the year 1816, and we are now well into a nonlinear decline of the tree population.

Let us return to the critical time defined by Eq. (8), when the number of trees per person equals the minimum necessary to support human life (not to mention the lives of other oxygen-breathing species). Let n be the

number of persons per tree when $t = t_c$, which with our numbers of 716 trees/person gives $n = 0.0013$ persons/tree. Inserting Eqs. (10) and (14) into Eq. (8) gives

$$\frac{nT_o}{P_o} = x(1 + \rho x)^{\gamma-1} \tag{17}$$

where $nT_o/P_o = 1.07 \times 10^7$ and $x = e^{\lambda t_c} \equiv 10^{7+\varepsilon}$. A numerical solution of Eq. (17) shows $\varepsilon = -0.856 \{+1.44\}$, so that $e^{\lambda t_c} = 1.4 \times 10^6 \{2.75 \times 10^8\}$, and $t_c = 1298 \{2001\}$, the year 2798 \{3501\}. (In 2018 there were about 7 billion people and 3 trillion trees, so $n_{2018} \sim 0.002$ persons/tree.)

Next we turn to the rate equations for carbon dioxide and oxygen. Using Eqs. (10) and (12), upon integration Eq. (3) becomes

$$C(t) - C_o = k_3 P_o I(t) - k_4 T_o J(t) \tag{18}$$

and for Eq. (4),

$$O(t) - O_o = -k_2 P_o I(t) + k_1 T_o J(t) \tag{19}$$

where C_o and O_o are integration constants,[12] with

$$I(t) = \int_0^t \frac{e^{\lambda t'}}{1+\rho e^{\lambda t'}} \, dt' = \frac{1}{\rho\lambda}\ln(1 + \rho e^{\lambda t}) \tag{20}$$

and

$$J(t) = \int_0^t (1 + \rho e^{\lambda t'})^{-\gamma} \, dt' \tag{21}$$

One can try several approximation schemes. For instance, at sufficiently large times when $\rho e^{\lambda t} \gg 1$,[13] we may say $I(t) \approx \frac{1}{\rho\lambda}(\ln\rho + \lambda t)$, and $J(t)$ becomes

$$J(t) \approx \frac{1}{\rho^\gamma \gamma \lambda}(1 - e^{-\gamma\lambda t}) \tag{22}$$

Now Eq. (18) becomes approximately

$$C(t) \approx C_o + \frac{k_3 P_o}{\rho\lambda}(\ln\rho + \lambda t) - \frac{k_4 T_o}{\rho^\gamma \gamma \lambda}(1 - e^{-\gamma\lambda t}) \tag{23}$$

and Eq. (19),

$$O(t) \approx O_o + \frac{k_2 P_o}{\rho\lambda}(\ln\rho + \lambda t) + \frac{k_1 T_o}{\rho^\gamma \gamma \lambda}(1 - e^{-\gamma\lambda t}) \tag{24}$$

It is revealing to separate the two contributions to the *changes* in the CO_2 and oxygen abundances from 1500 to 2018. Using our data in Eq. (23), the net change in CO_2 shows an increase of over 8 GT:

$$C(518 \text{ yr}) - C_o \approx (81.4 - 0.1) \times 10^{12} \text{ tons} = 81.3 \text{ GT} \tag{25}$$

where 81.4 GT comes from people with their machines producing 11 T/person-yr of CO_2, and the 0.1 GT comes from CO_2 uptake by trees. The oxygen difference, using $k_2 = 1.8 \times 10^{-4}$ tons/person-yr for *breathing only*, gives a result that, when compared to the effects of technology, is quite revealing. Then the terms in Eq. (24) show a net O_2 decrease on the order of 0.8 GT:

$$O(518 \text{ yr}) - O_o \approx (-1.34 + 0.54) \text{ GT} = -0.80 \text{ GT} \tag{26}$$

The negative balance means that when people use oxygen only for breathing, oxygen consumption due to population growth depletes the oxygen supply faster than trees can replenish it. Figure 2 shows $C(t) - C_o$ and $O(t) - O_o$ as functions of time. Notice that the CO_2 abundance is essentially flat until the year 1900, the O_2 abundance declines sharply almost coincidentally with the CO_2 increase, and these quantities become equal at approximately $t = 600$ yr, the year 2100. After that CO_2 increases and O_2 decreases approximately linearly, according to Eqs. (23)–(24).

However, each person with their machines produce about 11 tons of CO_2 per year (2018 figures).[9] Of this, only 1.8×10^{-4} tons are exhaled in breathing,[9] and therefore essentially all of the 11 tons/yr is produced by machines. How much annual per capita O_2 consumption does this imply? Consider the combustion of octane, the dominant molecule in gasoline. Its combustion proceeds according to the reaction

$$C_8H_{18} + 12.5\, O_2 \rightarrow 8CO_2 + 9H_2O \tag{27}$$
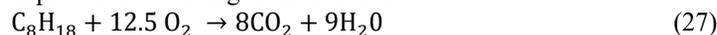
The weight ratio of eight CO_2 molecules to one octane molecule is $[8CO_2]/[C_8H_{18}] \approx 3$. A gallon of gasoline weighs approximately 6 pounds. Therefore the combustion of one gallon of gasoline produces about 18 pounds of CO_2. The weight ratio of 12.5 O_2 molecules to 8 CO_2 molecules is $[12.5\, O_2]/[8\, CO_2] \approx 1.136$, so to produce 11 tons of CO_2 consumes about 12.5 tons of O_2 per capita each year. Taking into account the oxygen consumption by machines per capita, the rate coefficient for O_2 consumption changes k_2 into 12.5 tons/person-yr, which in turn changes Eq. (26) into

$$O(518 \text{ yr}) - O_o \approx -92 \text{ GT} \tag{28}$$

The oxygen consumption of machines accounts for an "excess" oxygen consumption of over 90 billion tons.
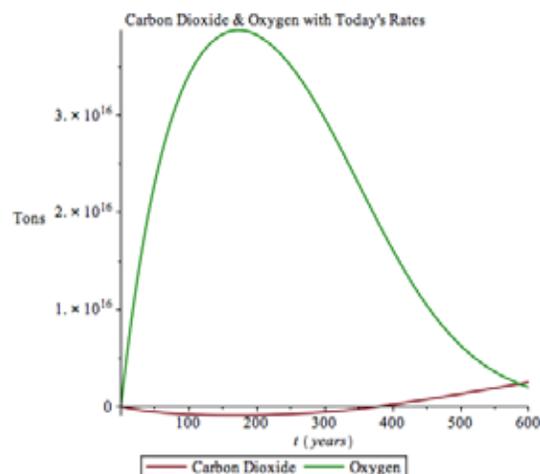
FIG. 2. The model's atmospheric carbon dioxide and oxygen abundances, $C(t) - C_o$ and $O(t) - O_o$, using rate coefficients held at their 2018 values. $t = 0$ denotes the year 1500.

Discussion

The foregoing calculations are a toy model intended to demonstrate the issues involved in studying the dynamics of atmospheric carbon dioxide and oxygen abundances as they are affected by trees and people *only*. The final numbers produced in this model are not meant to be taken seriously, but they do suggest qualitative trends that we as a society, and as individuals, would do well to take seriously. As Freeman Dyson has observed, "In the long run, qualitative changes always outweigh the quantitative ones."[14]

We have chosen the year 1500 as $t = 0$ because it was near the end of the pre-industrial era, before fossil fuel burning became the norm and before much of the planet was deforested, and because robust estimates exist of the human and tree populations at that time.

Most of the rate coefficients are not constants—a feature we have ignored for mathematical simplicity. To step through Eqs. (1)–(4) numerically would require data for the rate coefficients as a function of time, a task beyond the scope of this study. More realistic models would also include other sources and sinks of carbon dioxide and oxygen (e.g., the ocean's phytoplankton produces at least half of the oxygen[15]), other agents besides human actions that affect tree population, and other atmospheric gases.

One point is certain: This study reinforces the realization that unabated fossil fuel consumption, deforestation, and exponential population growth are not sustainable. Human economies and desires are not immune to nature's realities.

Acknowledgment

References

1. S. Weart, *The Discovery of Global Warming* (Harvard University Press, Cambridge, MA, 2003), offers a comprehensive survey with references to a large number of important papers.
2. "Population Estimates: Year One through 2010 A.D.," http://www.ecology.com.population-estimates-year-2050/.
3. N. Wolchover, "How Many People Can Earth Support?" https://www.livescience.com/16493-people-planet-earth-support.html, Oct. 11, 2011; "How Many People Can Our World Support?" http://worldpopulationhistory.org/carrying-capacity/.
4. J. Amos, "Earth's Trees Number 'Three Trillion,'" http://www.bbc.com/news/science-environment-34134366, Sept. 3, 2015. On p. 4 Amos says "The team estimates we are removing about 15 billion trees a year, with perhaps only five billion being planted back."
5. D. Bolton, "There are 3 Trillion Trees on Earth—But They're Disappearing Fast," https://www.independent.co.uk/environment/how-many-trees-are-there-on-earth-10483553, Sept. 2, 2015; https://www.livescience.com/27692-deforestation.html.

Neutron Attenuation in Polyethylene Using an AmBe Source

Dylan Barbagallo,[1, a)] Brooke Bolduc,[1] Brian Hassett,[1] Walter Johnson,[1] Kendrick Koumba,[1] Ally Leeming,[1] Phuc Mach,[1] Joe McCormack,[2] Molly McDonough,[1] and Jacqueline Nyamwanda[1, b)]

[1] *Department of Physics, Suffolk University, 20 Somerset St., Boston, Massachusetts 02108, USA*
[2] *Massachusetts General Hospital, Proton Center, 55 Fruit St., Boston, Massachusetts 02114, USA*

a) Corresponding author: dbarbagallo@su.suffolk.edu
b) jnyamwanda@suffolk.edu

Abstract. In this project an americium-beryllium (AmBe) neutron source was used to study the attenuation characteristics of polyethylene on an incident flux of varying neutron energies from 200 keV to 10 MeV. The linear absorption coefficient suitable for a single neutron energy was found to vary with absorber thickness due to the higher cross section for absorption of low-energy neutrons. The attenuation coefficient for a thickness greater than 15 cm was found to be associated with higher velocity neutrons.

INTRODUCTION

The research in this paper is based on a collaboration between the Suffolk University Physics department and the Radiation Oncology department at Massachusetts General Hospital in Boston. Neutrons are produced in several circumstances, such as high-energy photons hitting high-z materials in medical LINACs, nuclear reactors, and future spaceships traveling to Mars subject to high-energy cosmic rays. Neutrons of various energies have detrimental effects on humans, so it is important to understand the shielding properties of different materials. Materials with a large concentration of H atoms, such as polyethylene, are of interest given that collisions between neutrons and H atoms produce a large fractional energy loss of the incident neutrons, resulting in a high probability of neutron absorption. This paper concerns attenuation of neutrons ranging in energy from 200 keV to 10 MeV by polyethylene generated from an AmBe source.

EXPERIMENTAL APPARATUS

Source. For a neutron source, the AmBe source was used, courtesy of the Proton Center at Massachusetts General Hospital (MGH). This source (Am-241) has a known activity, which is A_{ct} 1.1×107 n/s. The neutron distribution as a function of energy is not known, but AmBe sources average at 4.2 MeV, with a maximum value of 11 MeV.[1] The energy spectrum of an AmBe source varies with composition of Am and Be but in general has a decreasing neutron flux with energy.[2, 3] To illustrate, data from this reference was used to calculate the percentage of neutron flux vs. energy from an AmBe source.

Detectors. In order to detect neutrons bubble detectors were used, which are insensitive to gammas and sensitive to neutron energies above 200 keV.[4] These detectors are available from Bubble Technology Industries (BTI) in Chalk River, Canada, and are the size of a test tube. Each detector consists of a plastic tube holding a polymer medium with microscopic liquid droplets dispersed throughout. When pressure on the polymer is released by unscrewing a plunger at the base of the tube, the droplets become metastable with vapor pressure in excess of ambient pressure and vaporize when exposed to recoils from neutron interactions.[5] The number of bubbles produced is proportional to the neutron dose, and each detector is calibrated by the manufacturer in bubbles/mrem. After

exposure to radiation, the detectors contain bubbles (shown in Fig. 2) which that can be counted using ImageJ software.
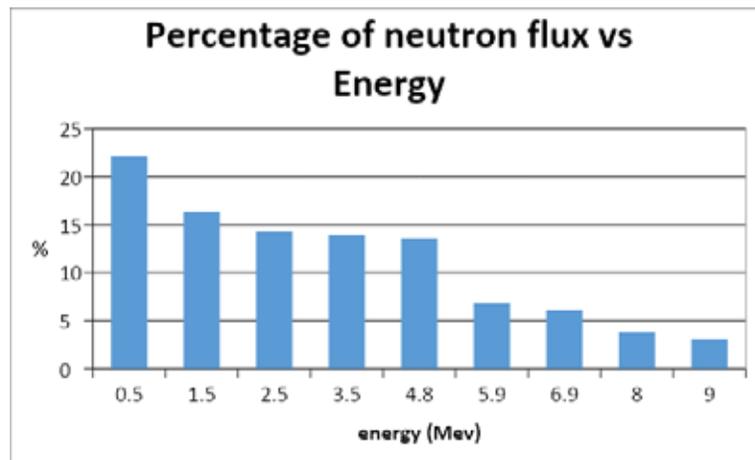
FIGURE 1. Sample dataset from an AmBe source.

Shielding. The absorbers were pure polyethylene rectangular blocks, each 1 inch in thickness. In order to produce varying thicknesses of shielding, blocks were stacked between the AmBe source and the bubble detector. Figure 2 shows four bubble detectors separated by 90°. Each detector is placed 35 cm from the center of the table where the cylindrical neutron source is placed.
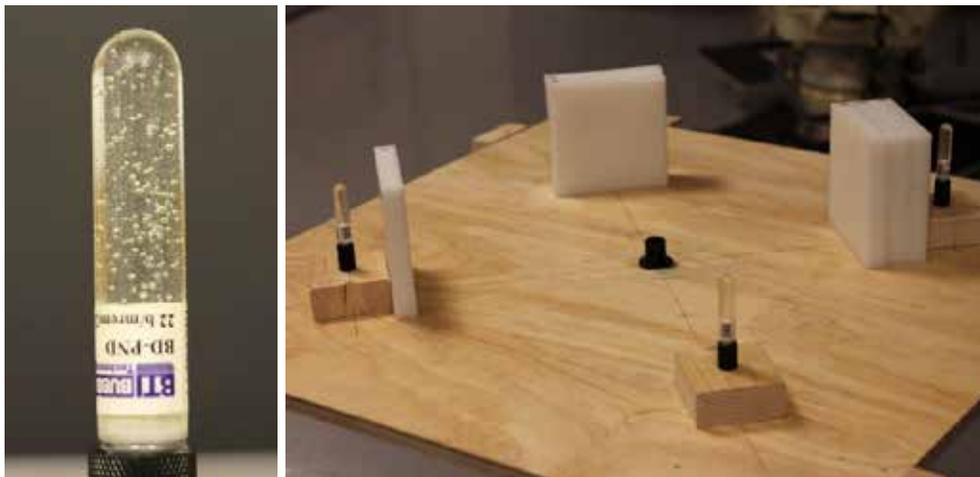
FIGURE 2. Left: An exposed bubble detector used for counting. Right: Experimental setup.

PROCEDURE AND CALCULATIONS

The intensity arriving at an unshielded bubble detector r_0 away from the source is given by

$$I_0 = \frac{A_{ct}}{4\pi r_0^2} \qquad \text{w/ } A_{ct} = 1.1 \times 10^7 \frac{\text{neutrons}}{\text{s}} \tag{1}$$

This includes all energies of neutrons emitted by the source and for 35 cm gives

$$I_0 = 715 \frac{n}{\text{cm}^2 \text{ s}} \tag{2}$$

This is the theoretical value (not measured) based on the activity of the source and includes neutrons of all energies.

The bubble detectors, however, are sensitive only to neutrons above 200 keV, so a bubble detector which is not shielded at this distance from the source will react to a theoretical intensity corresponding to

$$I_1 = \frac{A_{>200\text{ keV}}}{4\pi r_0^2} \tag{3}$$

This intensity was measured using the bubble detector, as described below, and gave the value

$$I_1 = 617 \ \frac{\text{neutrons}}{\text{cm}^2 \text{ s}} \tag{4}$$

The difference between all the neutrons given by (2) and those above 200 keV given by (4) is a measure of the neutrons from our AmBe source which are below 200 keV arriving at 35 cm. This gives about 98 neutrons/cm² s, corresponding to about 14% of the total of 715 in (2). This is consistent with the 22% below 1 MeV shown above in Fig. 1 for a typical AmBe source.

If a rectangular slab of polyethylene of thickness d is placed in front of the bubble detector, then the intensity reaching the bubble detector is decreased and given by

$$I_2 = I_1 e^{-\mu d} \tag{5}$$

This equation holds for a value of μ for each neutron energy in the beam. For multiple energies in the incident flux the value of the attenuation coefficient is a weighted average depending on the distribution of energies in the beam.

This neutron intensity is determined by use of bubble detectors which determine dose delivered in time t, which is then converted to neutrons/cm² (fluence) over that time using calibration information from the bubble detector manufacturer. The conversion constant is

$$C = 3.7 \times 10^{-5} \text{ mrem per } \frac{\text{neutrons}}{\text{cm}^2} \tag{6}$$

The measurement of the dose at the location is done by counting the bubbles produced:

$$B = \text{bubbles in detector}$$
$$S = \text{sensitivity} = \frac{\text{bubbles}}{\text{mrem}}$$
$$D = \text{dose in mrem}$$
$$D = \frac{B}{S} \tag{7}$$

There is an error in the dose due to uncertainty in the number of bubbles. This uncertainty has two sources: (1) errors in counting the number of bubbles and (2) statistical binomial errors associated with the number of counts.

After the experiment, each bubble detector was photographed four times at 90° angles, and then the bubbles were counted by different people and an average was taken:

$$\sigma_B = \text{error in the number of bubbles}$$
$$\sigma_{ct} = \text{error in the counting of the bubbles in the detector}$$
$$\sigma_{st} = \text{statistical error in the bubbles in the detector}$$
$$\sigma_B^2 = \sigma_{ct}^2 + \sigma_{st}^2 \tag{8}$$

The dose in mrem is determined by the fluence F, the number of neutrons/cm² delivered to the detector over the radiation time. The fluence F is the neutrons/cm² after some time t:

$$F = \frac{\text{neutrons}}{\text{cm}^2} \text{ at the detector}$$

The fluence is determined from the dose using the factor C given in Eq. (6):

$$F = \frac{D}{C} \tag{9}$$

To measure the neutron intensity in neutrons/cm²/s, use the fluence determined by the bubbles divided by the time:

$$I_{meas} = \frac{F}{t} \tag{10}$$

In this way the intensities mentioned above, I_1 and I_2, and the errors in each can be calculated.

The error in the intensity as shown above depends on the error in F and D and therefore the error in the number of bubbles shown in Eq. (8). There is also another consideration due to the solid angle subtended by the detector. The active area of the detector from top to bottom is 5 cm. The neutron source was positioned so that its center was the same height as the midpoint of the active area of the bubble detector, so from the source to the center of the bubble detector was 35 cm. However, the solid angle subtended by the detector was not all at the same distance r from the source because of increasing distance from the source as you move from the center of the detector to the top or bottom of the detector. To the top and bottom of the detector the distance was 35.09 cm. The intensity goes like $1/r^2$, so we can find the error in the intensity due to this effect by propagation of errors in r to the intensity. Using the maximum error in r as 0.09 we have

$$\frac{\sigma_I}{I} = \frac{2\sigma_r}{r} = 5.1 \times 10^{-3}$$

The result is that the solid angle effect at the detector produces an error of approximately 0.5%, which is negligible compared to the other errors in calculation of intensities and attenuation coefficient, as shown below in Table 1.

The effect of the absorber is shown by a decrease in neutron intensity from I_1 to I_2 expressed by the ratio

$$R = \frac{I_2}{I_1} \tag{11}$$

The error in the ratio R is obtained from the errors in the intensities:

$$\sigma_R^2 = \left(\frac{1}{I_1^2}\right)\sigma_{I_2}^2 + \left[\left(\frac{I_2^2}{I_1^4}\right)\right]\sigma_{I_1}^2 \tag{12}$$

From Eq. (5), to determine the absorption coefficient μ,

$$\mu = -\frac{1}{d}\ln\left(\frac{I_2}{I_1}\right) \tag{13}$$

The error in d is negligible, so the error in μ is given from the usual propagation of errors equation:

$$\sigma_\mu^2 = \left(\frac{\partial \mu}{\partial I_2}\right)^2 \sigma_{I_2}^2 + \left(\frac{\partial \mu}{\partial I_1}\right)^2 \sigma_{I_1}^2 \tag{14}$$

The result follows:

$$\sigma_\mu^2 = \left(\frac{1}{dI_2}\right)^2 \sigma_{I_2}^2 + \left(\frac{1}{dI_1}\right)^2 \sigma_{I_1}^2 \tag{15}$$

RESULTS AND DISCUSSION

The linear absorption coefficient calculated for each thickness of the polyethylene shield as described above gives the results shown in Table 1. The effectiveness of the absorber in decreasing the incident flux is clear from the plot shown in Fig. 3. An exponential fit shows the expected behavior, but it should be noted that the points below 10 cm thickness are consistently below the fit and the points for higher thickness are above the fit. This is consistent with the early layers of polyethylene removing the lower energy neutrons, which have a higher value of the absorption coefficient μ, and the latter layers being exposed to higher energy neutrons with a lower absorption coefficient. The average fit of the solid curve is a compromise between the two energy regions.

TABLE 1. Linear absorption coefficient calculated for each thickness of polyethylene.

Thickness (cm)	I_2/I_1	Fit	I_2/I_1 Err	μ	Err μ
0.000	1.00	1.00	0.000	Na	Na
2.540	0.632	0.719	0.111	0.181	0.069
5.080	0.472	0.516	0.76	0.148	0.032
7.620	0.326	0.371	0.046	0.147	0.019
10.160	0.267	0.267	0.044	0.130	0.016
15.240	0.136	0.138	0.019	0.131	0.009
17.780	0.126	0.099	0.018	0.116	0.008
20.320	0.110	0.071	0.0016	0.109	0.007

This is shown more clearly in Fig. 3, where the absorption coefficient is significantly higher at the lower values of thickness of absorber. This is discussed in more detail below.

Now consider the linear absorption coefficient μ as a function of thickness. The decreasing value of μ with increasing thickness is an interesting result associated with two factors: (1) an incident flux of neutrons from the AmBe source with a larger proportion of low-energy neutrons (as illustrated in Fig. 1), and (2) a higher absorption cross section for low-energy neutrons.[6] When the incident beam of mixed energy neutrons with a large fraction of low-energy neutrons approaches an absorber whose thickness is only a few centimeters, a larger fraction of low-energy neutrons is removed from the beam than high-energy neutrons. The attenuation for this small thickness results in a value of μ dominantly associated with low-energy neutrons.

From Fig. 3, it can be determined that 15 cm of polyethylene drops the flux to below 15% of the incident flux, and 20 cm drops it to about 10% of the neutron flux for the AmBe source studied. However, for a much larger thickness, over 10 cm, most of the low-energy neutrons have been removed in the first few centimeters of absorber so that the last few centimeters of the thickness are dominated by a beam mostly of high-energy neutrons and a correspondingly lower attenuation coefficient. The result is a steadily decreasing average attenuation coefficient with thickness as the proportion of neutrons in the beam becomes higher and higher energy for the latter layers of the thickness.
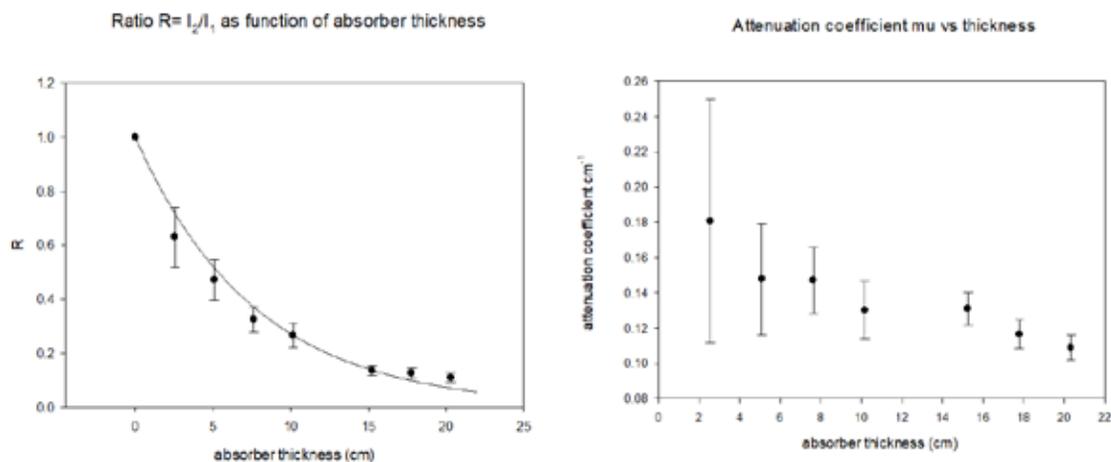
FIGURE 3. Left: Transmitted over incident flux vs. absorber thickness. Right: Absorption coefficient μ vs. absorber thickness.

If only the last three data points corresponding to a thickness greater than 15 cm are used, an average attenuation coefficient characteristic of high-energy neutrons can be obtained. The measured result is $\mu = 0.12 \pm 0.01$ cm^{-1}. This compares well to the value of 0.119 given for fast neutrons in Ref. 6.

CONCLUSIONS

The attenuation of neutrons from an AmBe source at Massachusetts General Hospital has been measured as a function of thickness for pure polyethylene absorbers. The results were obtained using bubble detectors sensitive to neutrons with energy greater than 200 keV. The attenuation coefficient shows a decreasing value with thickness as low-energy neutrons are removed from the first layers of the absorber and the measurements for thick absorbers produce values consistent with those in the literature for fast neutrons. For the energy distribution present in the neutron emissions from this AmBe source, a thickness of 20 cm of polyethylene will drop the flux to approximately 10% of the original value.

Next steps will involve using a series of bubble detectors with energy-dependent thresholds to determine the energy distribution of the AmBe source at MGH. The results can then be used to predict absorption of the incident flux with absorber thickness and compare with experimental results. Additional results will also be able to determine the energy distribution of the emerging beam after passing through an absorber of a certain thickness.

ACKNOWLEDGMENT

REFERENCES

1. United States Nuclear Regulatory Commission, Neutron Sources, Basic Health Physics, 0751 - H122 - 25 (2010); https://www.nrc.gov/docs/ML1122/ML11229A704.pdf.
2. I. Murata, I. Tsuda, R. Nakamura, S. Nakayama, M. Matsumoto, and H. Miyamaru, Prog. Nucl. Sci. Technol. **4**, 345–348 (2014); 10.15669/pnst.4.345.
3. R. Méndez *et al.*, Phys. Med. Biol. **50**, 5141 (2005).
4. F. Vanhavere, M. Loos, and H. Thierens, Radiat. Prot. Dosim. **85**(1-4), 27–30 (Sept 1999).
5. R. Sarkar, B. K. Chatterjee, B. Roy, and S. C. Roy, Radiat. Phys. Chem. **75**(12), 2186–2194 (2006).
6. Y. Elmahroug and C. Souga, Int. J. Phys. Res. (IJPR) **3**, 33–40 (2013).

Additional articles available online at the AIP Publishing home of the Journal of Undergraduate Reports in Physics:

aip.scitation.org/journal/jur

Quantum Inequalities and Particle Creation in the Presence of an External, Time-Dependent Mamaev-Trunov Potential

Kalista Schauer,[a] Michael Pfenning,[b] and Jared Cochrane[c]

United States Military Academy at West Point, West Point, New York 10996, USA
[a]kalista.schauer@westpoint.edu
[b]michael.pfenning@westpoint.edu
[c]jared.cochrane@westpoint.edu

Abstract. In 2011, Mr. Dan Solomon proposed a model of a quantized scalar field interacting with a time-dependent Mamaev-Trunov potential in two-dimensional Minkowski spacetime. This model is governed by the Klein-Gordon wave equation with a time-dependent potential. Mr. Solomon claims that this model violates both the classical energy conditions of special relativity and the quantum energy conditions of quantum field theory in curved spacetime. Every classical energy condition can be violated, and their natural replacements are known as quantum inequalities. Mr. Solomon attempted to prove violations of the spatial and temporal quantum inequalities, and he correctly assumed that the negative energy splits into two fluxes at the Cauchy surface, where the potential is turned off. Unfortunately, Solomon neglects the contribution to the energy density due to particle creation when the potential is turned off at time t=0. In this project, we calculate the contribution to the stress energy tensor due to particle creation. We show that the classical energy conditions are still violated but that the quantum energy inequalities hold, contrary to Mr. Solomon's statements.

Revisiting the Room-Temperature Metastable ^2E Lifetime in the Upper-Division Ruby-Phosphorescence Laboratory

Z. Jones[1,2], J. Hinds[1,3], S. Woznichak[1], and A. Calamai [1, a]

[1] *Department of Physics and Astronomy, Appalachian State University, Boone, NC 28608*
[2] *Department of Physics, East Carolina University, Greeenville, NC 27834*
[3] *Department of Physics, Michigan State University, East Lansing, MI 48823*

[a] Corresponding author: calamaiag@appstate.edu

Abstract. Many existing advanced laboratory experiences associated with the metastable ^2E term of Cr^{3+} in ruby, which gives rise to the R-lines at 692.7 and 694.3 nm, focus on a room-temperature measurement of the radiative lifetime of the ^2E term. In our local work developing a laboratory experience in atomic phosphorescence, we noted a lack of consistency in the literature for the lifetime of the Cr^{3+} ^2E term. These projects typically use commercially available ruby spheres for which the manufacturer(s) only state an ~2% Cr concentration. The uncertainty in chromium concentration represents one major source of systematic error for this laboratory experience, as does the neglect of reabsorption of R-line photons within the respective sample. We present our results and corrections for systematic issues that make this project a more rewarding experience for students. Our result for the room-temperature radiative-lifetime for the ^2E term is 3.3 ± 0.1 ms; which, unlike some more recent reports[1], compares favorably with that of Nelson and Sturge[3].

Programs
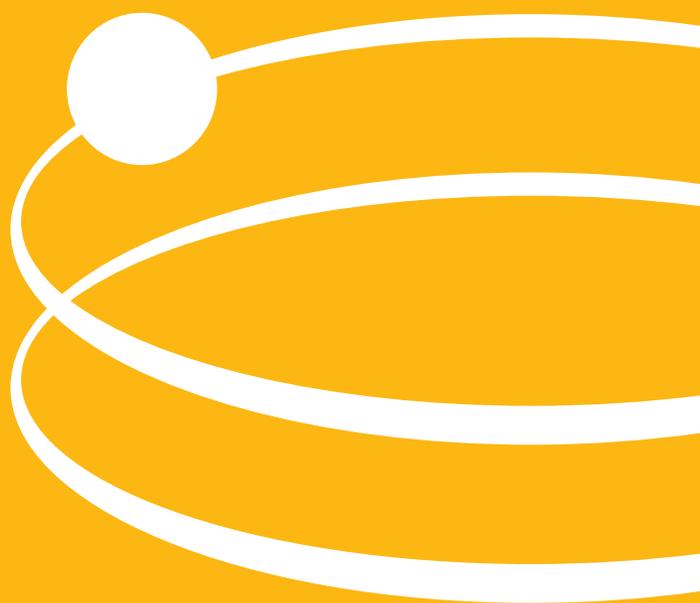
2019–20 SPS and Sigma Pi Sigma Year in Review

by Kayla Stephens and Mikayla Cleaver, SPS National Office

"Nothing in life is to be feared, it is only to be understood. Now is the time to understand more, so that we may fear less." — Marie Curie

Though it began just like any other, the 2019–20 academic year unexpectedly turned into something most of us have never experienced in our lifetimes. As doors to universities, colleges, and workplaces closed around the world, SPS National continued to support the SPS community, providing opportunities in research, scholarship, outreach, leadership, and advocacy. We are so proud of the response of the SPS and Sigma Pi Sigma community, who stepped up to support one another during this difficult time. We are in this together. No matter the circumstance, #PhysicsDontStop!

Fall 2019 began with activities to get the SPS community excited and prepared for the event of the year—November's gathering of over a thousand physics and astronomy students, mentors, alumni, and renowned scientists. The 2019 Physics Congress, "Making Waves & Breaking Boundaries," was held in Providence, Rhode Island, and gave attendees the opportunity to hear from luminaries in the field, tour fascinating science sites, engage in thought-provoking workshops, present scientific posters, and much more.

With the help of Sigma Pi Sigma members, SPS alumni, and the National Science Foundation, SPS dispersed approximately $70,000 in travel aid for students to attend this unique conference through PhysCon Travel and Reporter Awards, HBCU/MSI Travel Awards, and an SPS chapter video competition award.

The keystone of SPS and Sigma Pi Sigma is our community of volunteers, particularly the elected SPS National Council. This year's SPS National Council significantly contributed to the success of the 2019 Physics Congress. Along with that huge task, the Council had many other noteworthy accomplishments, including the creation and approval of the SPS and ΣΠΣ Statement on the Climate Crisis. The Council also approved and updated the SPS and ΣΠΣ Statement on Diversity, Inclusion, Ethics, and Responsibility. To view the statements written and approved by the SPS National Council, please visit spsnational.org/about/governance/statements.

Despite the challenges, the National Council also had the pleasure of welcoming new SPS and ΣΠΣ chapters in the 2019–20 academic year.

New Sigma Pi Sigma Chapters
#583 Brown University (Zone 1)

New SPS Chapters
#6118 Saint Catherine University (Zone 11)
#7390 Troy University (Zone 6)

The spring semester was different than ever before, with a global pandemic in effect. Colleges and universities closed their doors, and many students were deeply affected by personal loss, displacement, and the move to online learning. In response to this, SPS created many virtual opportunities to promote a sense of normalcy and community, ranging from March Madness–style brackets on our social media platforms to a weekly virtual colloquium series. We also created the SPS Emergency Scholarship to help members financially affected by the COVID-19 pandemic (spsnational.org/scholarships/SPSEmergency).

As of May 15, 2020, SPS has approximately 5,500 members and 832 chapters. Usually, each of the 18 SPS zones hosts a meeting for the SPS chapters in their region to support chapter and member growth. As the majority occur in the spring, many zones rescheduled for Fall 2020 or Spring 2021, in hopes that it will be safe to gather for conferences and meetings. Other zone meetings went virtual and, with the support of the SPS National Office, alumni, and volunteers, successfully engaged attendees with invited speakers and professional development activities.

SPS saw an increase in applications for both our fall and spring awards. In the fall, 35 chapters received awards, totaling $24,333 in funding. This spring, the number of applications for SPS scholarships doubled from the previous year, making it our most competitive pool yet. SPS awarded 18 scholarships, two Outstanding Undergraduate Research Awards, and the Outstanding Chapter Advisor Award, totaling $48,700 in prizes and funding.

Because of the COVID-19 pandemic, many undergraduate summer REU and internship positions were cancelled. However, with the support of the American Institute of Physics and partner organizations such as AAPT, APS, NIST, NASA, and our friends on Capitol Hill, SPS was able to continue its summer internship program, providing opportunities to 16 SPS members. The 2020 SPS Summer Internship Program will be held virtually, and activities will be provided to support an enriching experience for each intern.

Last summer, the 2019 Science Outreach Catalyst Kit (SOCK) intern, Noura Ibrahim, created an astronomy-themed outreach kit that we provided FREE to SPS chapters. The SOCK utilizes desserts to demonstrate different astronomical concepts—for example, Jell-O to show how LIGO measures gravitational waves and brownies to demonstrate the formation of craters on celestial bodies. SPS still has SOCKs in stock, so request your

free kit through our awards system. Also keep an eye out for our 2020 SOCK, which will focus on acoustics in celebration of the International Year of Sound!

ΣΠΣ continues to honor outstanding scholarship in physics and service. ΣΠΣ cuts across generational and professional lines and encourages connection and excellence in the physics community. This year included 160 inductions, nearly 100 of which were held virtually due to stay-at-home orders and to ensure the safety of our community. A total of 1,060 new members were inducted into lifelong membership of ΣΠΣ across 583 chapters.

Even though this year has been unprecedented, GradSchoolShopper, the Careers Toolbox, and the Alumni Engagement Program continue to support SPS members in effectively navigating career options. These free resources guide students in connecting with SPS alumni, resume building, interview tips, and much more. They are especially important for supporting seniors as they prepare for life after graduation, whether they plan to go directly into the workforce or to pursue a graduate degree.

SPS continues to support undergraduate attendance at national meetings of professional physics societies such as AAPT, APS, OSA, AMS, AAS, and more. SPS Travel and Reporter Awards give students the opportunity to present their research or write about their experiences for the SPS community. In the 2019–20 academic year, SPS provided 27 students with a total of $9,105 in travel funding, excluding the 2019 Physics Congress. As many meetings move to virtual platforms, SPS is now also offering $75 Reporter Awards to support registration costs for virtual conferences.

This also has been a great year of disseminating the research and programmatic activities of our members, enabling them to share their voices within the physics community through our publications. We published four issues of the SPS Observer, which includes JURP, and two issues of Radiations.

SPS Observer
2019 Fall: "Toward a Culture of Inclusion"
2020 Winter: "Up Your Momentum–Take Your SPS Chapter to the Next Level"
2020 Spring: "Physics and a Climate in Crisis"
2020 Summer: *Journal of Undergraduate Reports in Physics*

Radiations
2019 Fall: "Empowering the Next Generation of Physicists"
2020 Spring: "Reflecting on the Past, Preparing for the Future"

The 2019–20 year of SPS and ΣΠΣ embodied the mission of enriching the lives of students locally, regionally, nationally, and internationally. Although the year included moments of uncertainty, the SPS community came together and provided tools to allow members to flourish professionally, foster connections through a diverse network of physicists, and impact lives through outreach services. SPS and ΣΠΣ have worked to transform the future of physics and astronomy, and we are looking forward to what 2020–21 brings! If you are interested in continuing this legacy of opportunity and would like to donate, please visit donate.aip.org. And, of course, we hope to see you for the 2021 Physics Congress in Washington, DC. //

ABOVE: The 2019–20 National Council gives their best "Thumbs Up for Science" at PhysCon 2019. Photo courtesy of SPS National.

Meeting Notes are SPS member reflections on their experiences while attending professional scientific meetings. Professional meetings offer undergraduate students a unique opportunity to network amongst their peers, develop valuable skills and connections, present their research, and gain invaluable knowledge within the field. The following articles are select student reporter reflections from meetings that occurred within the last year.

You can find out how to apply for a reporter award here: spsnational.org/awards/reporter.

A PASSION FOR TEACHING REKINDLED

American Association of Physics Teachers
(AAPT) 2020 Winter Meeting

by Isabel Montero, SPS Member, University of North Georgia

When I arrived in Orlando, Florida, for the 2020 AAPT Winter Meeting, I was greeted by the sight of a young boy swaggering out of the Caribe Royale lobby doors like he owned the resort. In that moment, I wished I had even an ounce of the confidence that he possessed.

My nervousness about attending my first national AAPT meeting was palpable, compounded by the fact that I was the only undergraduate student from the University of North Georgia in attendance. Although I'm typically outgoing at conferences, I had never been to an event this large and was worried I might get swept up in all the commotion.

My goals for the conference were simple: to learn more about physics education research and, hopefully, narrow down a research project for my remaining undergraduate semesters. While I did achieve those goals, I was unprepared for the number of serendipitous events that also happened over the conference weekend.

At the AAPT Tweet-Up, I met a professor who would later introduce me to undergraduate student Carissa Giuliano, president of the Adelphi University SPS chapter. This introduction was the beginning of a rewarding friendship that benefited the constituents of both our chapters and led to a Winter Meeting weekend centered around the Society of Physics Students and outreach.

I then attended the AAPT Committee on Diversity in Physics meeting, where I observed how to run a coherent, successful, and interesting meeting while treating each person with respect and validating their concerns and ideas. Implementing these skills with my SPS chapter resulted in one of the most fluid semesters ever for our officers and members. In fact, there's been such a significant improvement in meeting attendance and member cohesion that it's hard to believe it's even the same organization as before—and we gained all of these incredible new characteristics by putting into practice what I observed at this meeting.

I also had the opportunity to network with national SPS figures, including SPS director Brad Conrad and programs manager Kayla Stephens, and was invited to volunteer at the Students Exploring Engineering and Science (SEES) outreach event on the final day of the conference. Alongside other undergraduate STEM students, I led hands-on activities on exciting topics in physics and astronomy

TOP: Isabel Montero. Photo by Celeste Montero.

ABOVE: Isabel Montero attends the AAPT Tweet-Up event with John Indergaard (right), Matthew Wright (second from right), and Dr. Gabriel Spalding. Photo by Jerri Anderson, AAPT marketing coordinator.

for young future scientists. This was decidedly the most impactful day of the conference for me.

The young students' excitement during the activities was infectious. I often think we physics and astronomy undergraduates become so overwhelmed by our majors that we forget that we were once in these kids' shoes. That innocent passion and developing curiosity was what propelled many of us into what we do today. The SEES event reminded me where my passion for physics

originated and rekindled my enthusiasm for teaching young minds and encouraging their pursuit of STEM.

Attending the AAPT Winter Meeting reaffirmed my passion for what I do and for the possibilities my future holds. When I first arrived, I wished for an ounce of that little boy's confidence. I wanted nothing more than to not get swept up in the commotion, to make it through the weekend by observing from the sidelines. This conference took every one of my intentions and shaped them into what I needed, not what I desired. I was totally consumed by my experience and left reinvigorated and ready to take what I had learned and pass it on to others—and I couldn't be more grateful. **//**

FORGING A PATH TO THE STARS

235th Winter Meeting of the American Astronomical Society

by Hannah Umansky, Morgan Waddy, and Levi Schult, SPS Members, University of Virginia

How can aspiring astronomers build careers in such a broad and dynamic field? At the 2020 American Astronomical Society meeting in Honolulu, Hawaii, we discovered that the road to success isn't always a straight one. Amid a whirlwind of overlapping exhibits, events, workshops, and plenary talks, we went off-schedule, overcame anxiety, and became inspired to merge passions. Along the way, we caught up with speakers who shared some advice for those just starting out.

For Creative Inspiration, Read Widely, by Hannah Umansky

Dr. Jason Hessels—a researcher at ASTRON, the Netherlands Institute for Radio Astronomy, and a professor at the University of Amsterdam—researches fast radio bursts, bright radio sources that emit for only milliseconds at a time. During a plenary session, Hessels explained how these bursts can be used to study the intergalactic medium, the ionized material between galaxies. After the lecture, we sat down with Hessels and asked how he got his start in fast radio bursts.

"I spent most of my PhD searching for millisecond pulsars . . . [and] a lot of the techniques are very similar to what you need to search for fast radio bursts," Hessels said. He recommended that students hoping to continue in research always check arXiv (arxiv.org) and read newly released papers from both inside and outside their field of study.

"Being able to put your results into context and understanding the links to other things is . . . a prerequisite for having the creativity to do something very interesting, instead of just turning the crank on something people have done before," Hessels told us.

Everyone's Path Looks Different, by Morgan Waddy

On the last day of the conference we caught up with astrophysicist Sheperd S. Doeleman, founding director of the Event Horizon Telescope project (EHT), after his plenary. He was an interesting character—for example, we learned that after receiving a bachelor of arts degree, he spent a year conducting experiments at McMurdo Station in Antarctica.

We talked with him about the things he was most excited about surrounding EHT—a global network of radio telescopes. He told us that EHT isn't a "first-light instrument," and that with the progression of time and the addition of more antennas, the resolution of the instrument only increases.

Since Doeleman had such an interesting journey to his current position, we asked if he had any advice for young astrophysicists. He drove home to us that everyone's path looks different. His work, he said, wasn't amazing out of the gate, but once he found his niche he was able to make up for lost time. His other advice? Recognize good opportunities when they present themselves—because they're seldom offered again.

Keep an Open Mind, by Levi Schult

After the NANOGrav (North American Nanohertz Observatory for Gravitational Waves) session, we interviewed Dr. Xavier Siemens—a

TOP: Hannah Umansky and Levi Schult (far right) interview researcher Jason Hessels of the Netherlands Institute for Radio Astronomy. Photo by Morgan Waddy.

ABOVE: Morgan Waddy makes a clay pulsar. Photo by Levi Schult.

physics professor at Oregon State University—and asked if he had advice for early-career astronomers.

"Keep an open mind about what you might be interested in," he said. "For a long time I thought I was only interested in cosmology . . . and later I discovered that there are actually a lot of interesting other things that you can do."

Siemens worked in cosmology before transitioning to gravitational wave work in LIGO and then NANOGrav. This shift wasn't initially by choice. He explained that he couldn't find a postdoctoral position in cosmology but was able to find one in gravitational waves. He kept an open mind and ended up enjoying it supremely! //

BREAKING BOUNDARIES: THE INTERDISCIPLINARY NATURE OF PHYSICS

2019 Sigma Pi Sigma Physics Congress (PhysCon)

by Ahnika Boring, Genevieve Nelson, and Daniel Wilson, PhysCon Reporters and SPS Members, Wheaton College

Physics is the study of matter and energy. Matter and energy make up everything. Therefore, physics *is the study of everything*. Well, things aren't quite that simple, but our group of liberal arts students is fascinated by how interconnected the world is—it's part of the reason we study physics in the first place.

As the largest gathering of undergraduate physics students in the United States, PhysCon provides an unparalleled opportunity for networking, exposure to new ideas, and development as future physicists. It highlights the breakdown of disciplinary boundaries and the cutting-edge research that's making waves in physics and the world at large. One of the highlights of our experience was the poster session, during which students had the opportunity to share their work with attendees.

Brightly colored posters, each surrounded by its own cluster of excited students and faculty, were organized into neat rows throughout the exhibit hall. The air buzzed with conversation as student researchers described their work to curious attendees. It was into this sea of sound, sights, and color that we waded, seeking out how student researchers experienced the interconnectedness of physics and the world.

Before long we bumped into Harry Chen, a student from the University of California Merced, who was presenting research at the intersection of physics, biology, and mathematics. He described his work as the experimentalists' analog of "turning knobs"—as fine-tuning the parameters of a particular model. His enthusiasm regarding the interdisciplinary nature of the project was almost tangible. He was excited to not only be gaining new perspectives but also to be making a difference.

We continued our journey around the room, taking in the different topics students were pursuing. In addition to more traditional physics fields like particle physics, there were posters on outreach, science policy, and even sociology.
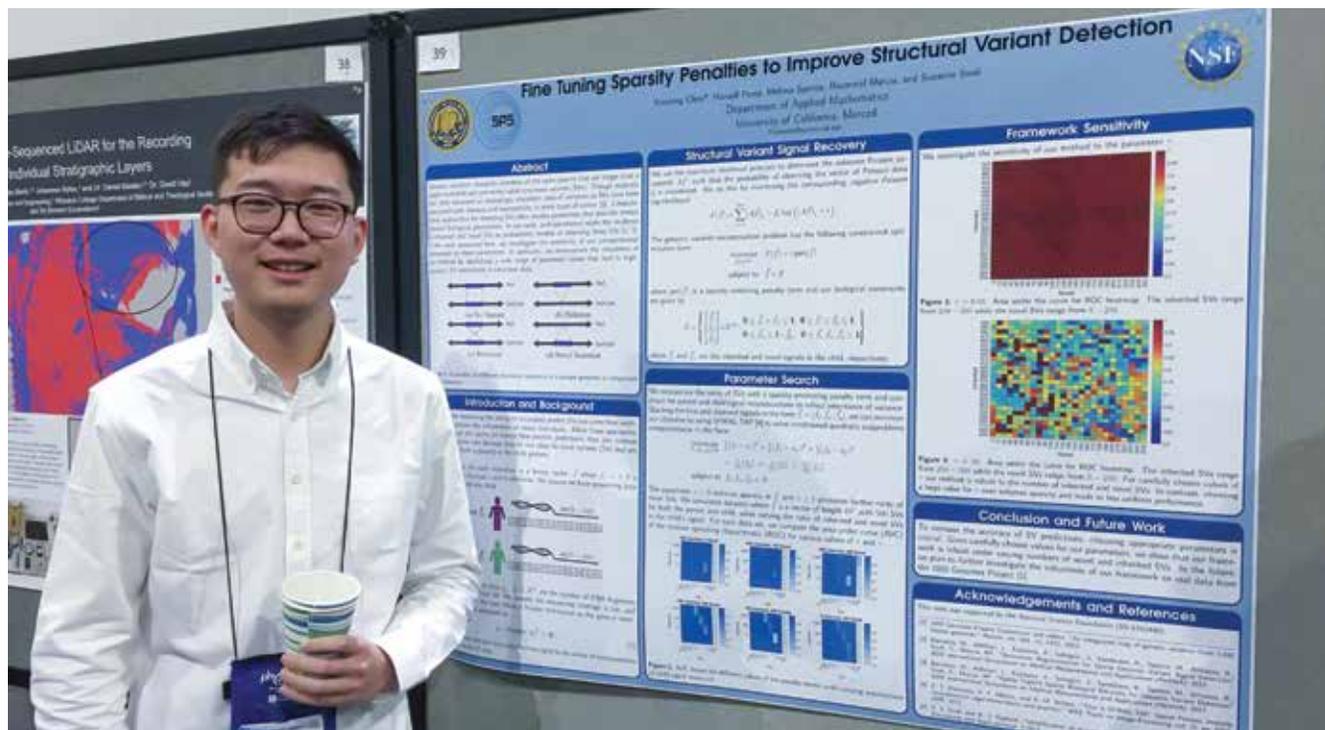
ABOVE: Harry Chen, a student from the University of California Merced, presenting his work at the 2019 PhysCon Poster Session. Photo courtesy of the Wheaton College PhysCon reporters.

Zubia Hasan, a student from Johns Hopkins University, shared her poster on condensed matter physics with us. She was working on the synthesis and evaluation of the compound $CuTeO_4$. Hasan noted the necessity of cooperation between chemists and physicists in her lab and beyond. "[Y]ou will often find a chemistry lab and a physics lab side-by-side because they sort of always work in collaboration," she told us.

Next, we stopped by an astronomy poster related to the TESS (Transiting Extrasolar Survey Satellite) mission, presented by Helena Richie, a student from the University of Pittsburgh. In her research group, members learn to do observational astronomy bottom-to-top. Richie says this provided her with a strong foundation in astronomical research but also allowed her to gain valuable leadership skills that can be applied anywhere.

As the crowd began to file out of the exhibit hall to make it to the next PhysCon plenary talk, we took a minute to grab coffee and reflect. We felt privileged to have heard so many different perspectives in such a short time. We were encouraged to hear that so many physicists think interdisciplinary research and communication is crucial—physics truly is the study of everything. //
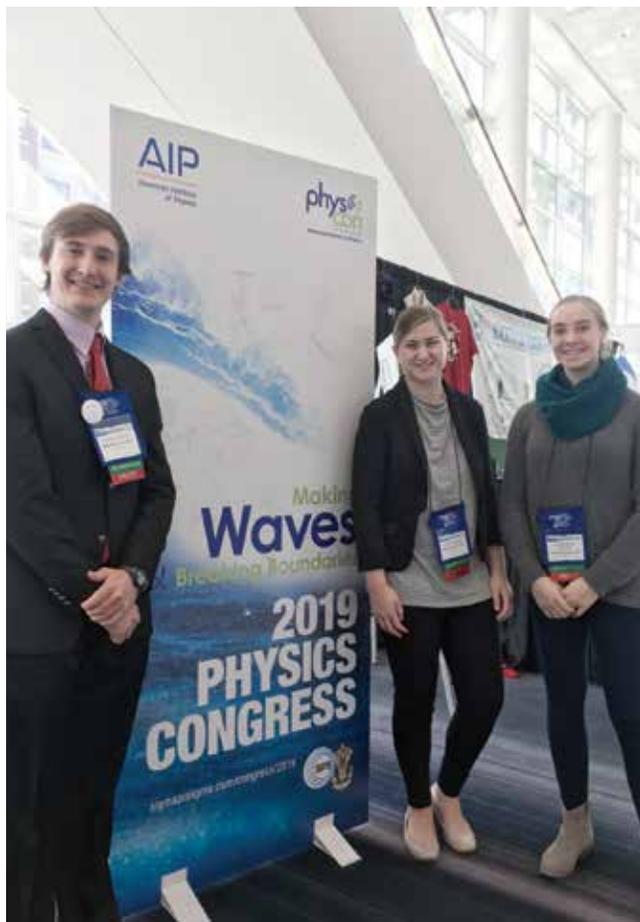
ABOVE: From left, 2019 PhysCon reporters Daniel Wilson, Ahnika Boring, and Genevieve Nelson. Photo courtesy of the Wheaton College PhysCon reporters.

SCIENCE POLICY AT PHYSCON: A LESSON IN COMMUNICATING THROUGH UNDERSTANDING

2019 Sigma Pi Sigma Physics Congress (PhysCon)

by Robin Glefke, PhysCon Reporter and SPS Member, Georgia Institute of Technology

PhysCon 2019 kicked off with an icebreaker, the group working together to perform a fun reaction-diffusion experiment by propagating a human wave across the audience. While a silly exercise on the theme of the conference—"Making Waves and Breaking Boundaries"—it demonstrated our unity as physics students. Unity is especially important as we work together to bridge the communication gap between physicists and the public, and between physicists and other scientists.

My first workshop at PhysCon was Science Policy for Scientists, led by Anna Quider, assistant vice president for federal relations at Northern Illinois University, and Steve Gerencser, associate director of government relations at Brown University. I walked in with two friends from my university, and just as we sat down, one of them spilled coffee across the table. Over that spilled coffee, we bonded with our tablemates and eagerly learned about the intersection of science and the US federal government—notably, the effects of the 2018–19 government shutdown on science.

We were then directed to look at the proposed budget for government-funded research and allocate an 8% cut. We could cut all of the programs by 8%, eliminate one or more programs that totaled 8% of the budget, or do anything in between.

It often feels satisfying to scapegoat the US Congress for the lack of funding in important research areas, but this activity demonstrated the complexity of the decisions they face. Most science research is funded under the Commerce, Justice, and Science allotment of the US discretionary spending budget. This budget is separate from other slices of the budgetary pie, such as the homeland security or defense allotments. It also means that science research programs are competing for a finite amount of money from the slice of the budget that also supports transportation infrastructure, public safety entities, and other important areas.

Discussing what should be cut given the constraints was eye-opening, particularly in the case of the James Webb Space Telescope (JWST).

I love astronomy. I initially studied physics because of my love of the stars. JWST will be an incredible step in humanity's exploration of the cosmos, and if I heard its budget would be significantly cut, I would angrily shake my fist at the powers that be. However, during this activity I realized that it's *expensive*. It has cost about half a billion dollars each year for the last several years from NASA's roughly $20 billion total spending budget. Despite how much I value JWST, I chose to cut more money from this program than any other. Many other students did too.

Some students proposed that the federal science funding crisis could be fixed by cutting defense spending instead, even though some fraction of defense spending does go to research. It seemed that workshop attendees had found an enemy to rally behind.

ABOVE: Led by Steve Gerencser and Anna Quider, PhysCon attendees tackle the subject of science policy. Photo courtesy of Anna Quider.

But we are a diverse community of people; near the end of the workshop, a student from the United States Air Force Academy stood up to speak. She asked with a true desire to understand, considering that her background shielded her from many of these opinions, why people felt such disdain for the current level of defense funding. This was an amazing response to criticism, and a very respectful discussion followed!

Removing the context from this discussion leaves behind a fundamental principle that can be utilized in other problems: the desire to understand and communicate. In conversations with climate change deniers and people who don't trust science, there is often a lack of understanding that leads to conflict. Similarly, when we as researchers make an enemy of an entity, we may ostracize others and limit the progress of science. Sometimes, all it takes to combat this is a person who is willing to start a conversation, like my new friend from the Air Force Academy. *//*

SPS awards are generously funded by donations from SPS alumni, Sigma Pi Sigma members, and friends of SPS. All awardees submit a final report highlighting how they carried out their proposed project. The following articles are abbreviated reports from recent Future Faces of Physics, Marsh W. White, Sigma Pi Sigma, and Chapter Research awardees.

To learn more about the SPS Chapter Awards, visit spsnational.org/awards/chapter-awards.

UPLIFTING STUDENTS WITH HOVERCRAFTS: A SMOOTH INTRODUCTION TO PHYSICS

2018–19 SPS Future Faces of Physics Award

Rhodes College

Project Lead: Evan Main

Chapter Advisor: Brent Hoffmeister

Project Summary: The Rhodes College SPS chapter launched an outreach initiative focused on engaging underprivileged elementary students in the Memphis area. Our goal was to get these students excited about physics by building and riding hovercrafts.

Our SPS chapter is known for its wild demonstrations, so building a hovercraft that could lift four students at once was the perfect project for our daylong outreach initiative, made possible in 2019 by our Future Faces of Physics Award. Through this initiative, we taught students physics concepts, created a working hovercraft that can be used in future demos, and established a relationship with a new elementary school.

Working with one class at a time, we engaged with around 90 fifth-grade students from Idlewild Elementary School, which has a culturally and economically diverse student body. Each session began with a presentation about how hovercrafts work and introduced concepts like pressure and buoyancy. We worked through a real example of a physics problem and were happy to find that the students weren't too intimidated.

After the presentation, we revealed a surprise—the students would be building their own balloon-powered hovercrafts, an activity they really seemed to enjoy. The crafts were simple, elegant, and physically analogous to the big hovercraft we built for the event. It was a lot of fun to watch the students get creative with their designs and then use their hovercrafts.

We then had another surprise: It was time to ride the big hovercraft! Powered by a leaf blower, our fully functional hovercraft is entirely electric—making it safe and not too loud—and can lift four students at once. Some students were apprehensive at first, but once they saw their classmates zooming around like they were riding an air hockey puck, they were sold.

Throughout the day, we made note of whether the students were engaging with the activities and—most importantly—having fun. We could see that many of them had an active interest in science and creating. Some students were so excited about their hovercrafts that they modified them over lunch, using lunch trays to increase their surface area. Genius!

The response of the teachers and administrators at the school was very encouraging, and the SPS members who helped make the event possible gained new skills—including event organization, communication, and working with young students—and became better friends along the way. Our SPS chapter as a whole was strengthened by this outreach opportunity, and we're looking forward to including more members next year. Our thorough documentation of this process will help our chapter plan future outreach events.

By building and testing hovercrafts, we provided a fun and interesting demonstration, and judging by all the smiles and laughter throughout the event, we accomplished our goal. We loved watching the students' faces light up when they realized they would be riding a huge hovercraft during school. We hope this was an experience they'll never forget and that their enjoyment of the activity inspires them to pursue physics in the future. //

For more details on this project, visit our SPS award page at spsnational.org/awards/future-faces-physics-award/2019/rhodes-college.

ABOVE: Project lead Evan Main tests out the big hovercraft. Photo by Anna Murphree.

I CAN SCIENCE: HANDS-ON LESSONS ENCOURAGE SCIENTIFIC CURIOSITY

2018–19 SPS Future Faces of Physics Award

The George Washington University

Project Lead: Jason Starita

Project Advisor: Gary White

Project Summary: I CAN Science is an outreach collaboration between The George Washington University's SPS chapter and the Life Pieces to Masterpieces afterschool program. Aimed at young African American boys, the program promotes hands-on physics learning through demonstrations.

"Physics Is Everywhere"

For 36 African American boys at Drew Elementary School in Washington, DC, the theme of our I CAN Science program became clearer with each lesson they received over the course of the 2019 Spring semester.

The students, ages seven to twelve, were participants in the Life Pieces to Masterpieces afterschool program hosted by Drew Elementary. In partnership with the program, members of The George Washington University's SPS chapter made seven trips to the school to inspire scientific curiosity in students. By helping our youth feel included in STEM—first by acknowledging cultural differences, then by empowering students with the resources to explore their budding scientific questions—we hope to enhance their interest in physics, now and in the future.

Each lesson focused on one or two buzzwords—physics, astronomy, motors and vehicles, motion and rotation, fluid, light, and phase change—and included two to four interactive lab stations overseen by SPS members and our adviser. In keeping with our theme, the activities revealed that physics is everywhere in our daily lives.

Concepts demonstrated at each station varied depending on age. During the lesson on vehicles, for example, younger students learned about lift versus gravity by making, testing, and revising paper airplane designs. Older students learned about the functions of motors by making simple robots.

Each lesson was designed to allow students to learn about different physical concepts in a hands-on environment. To keep the material engaging and accessible, we deemphasized the complicated mathematics driving these ideas. Lessons concluded with time for students to reflect on what they'd learned, share exciting new facts—"Saturn's rings are really just tiny rocks around the planet"—and possibly hear something they may have missed, giving them the opportunity to engage like scientists in a collaborative community.

ABOVE: Students in the I CAN Science program create robots to learn about the functions of motors. Photo courtesy of Seneca Wells.

Students were able to expand upon their understanding of each week's topic using the ideas and concepts they learned in previous weeks or while in school. They also had access to our portable science station, which allowed them to take home items like diffraction glasses and Slinkys. This helped students feel more connected to the topics they learned about and more eager to share their scientific experiences with peers, family, and other mentors.

Our SPS chapter has worked with Life Pieces to Masterpieces for the past five years. We intend to continue our relationship with the program, both to support the growth of scientific curiosity among students and to give SPS members hands-on teaching experiences. By fostering this relationship, we're proud to support this multifaceted program that aims to develop character, self-reliance, and integrity in young African American men while fostering mentorship relationships with positive role models.

By engaging these students with physics demonstrations, we seek to invoke a passion for science that inspires them to pursue physics and other STEM fields. In turn, we hope this work ultimately results in greater diversity in the scientific community. With a wider range of backgrounds and outlooks, we gain new perspectives and benefit from individual ideas and experiences. The students in this program are the future of our scientific communities. //

For more details on this project, visit our SPS award page at spsnational.org/awards/future-faces-physics-award/2019/george-washington-university.

QUANTUM KIDS: YOU GOT THIS!

2018–19 Marsh White Award

University of Maryland, College Park

Project Lead: Tyler B. McDonnell

Project Advisor: Donna Hammer

Project Summary: The University of Maryland SPS received the Marsh W. White Award from SPS National to design a program of activities focusing on quantum concepts for elementary school students that introduces them to the world of quantum through diverse learning experiences.

Quantum physics for kids? Absolutely! Our outreach program, designed for elementary school students, proved that physics can be accessible to young learners. The program focused on the quantum concepts of wave–particle duality, quantization of energy, energy levels, and interacting particles. Each concept had a station designed to engage the students' interest and provoke thought. During the program, students also had access to a quantum library with books covering these and other concepts.

The two 2-hour sessions we hosted began with a discussion on the scope of the program, everyday quantum technologies, current national focus on quantum education, and current research being conducted at the University of Maryland. Afterward, students were given passports containing questions and fill-in-the-blank responses, allowing them to track their progress through the program. The students rotated through four stations: the double-slit experiment, blackbody radiation, LEDs and energy levels, and superconductivity.

At the double-slit experiment station, focused on wave–particle duality, students observed laser light through a double slit, single slit, and their own constructed pinhole apertures to investigate the diffracted light pattern created. Afterward, they were shown the double-slit effect with photon particles creating the same pattern. These guided students to observe and think about how peculiar the quantum world can be in comparison to our everyday world.

Students stopping at the blackbody radiation station learned about Max Planck's discovery and how energy is considered quantized, and then built their own blackbodies from shoe boxes and colored paper to investigate the concept through critical thinking and discussion. At the superconductivity station, students were shown a superconducting track demo and engaged in Q&A on how the superconducting puck was able to float across the entire track, examining a different way that particles can interact.

To understand the concept of energy levels, students discussed the color spectrum and were given colored LEDs to see which LED color allowed them to write their name the fastest. They then learned how a forward-bias p-n junction operates and how the amount of

TOP: Students create their own blackbodies, while Thomas P. Gleason explains their significance.

ABOVE: The Quantum Kids: You Got This! team, left to right: Donna Hammer, Robert Whitlock, Cody Kuntz, Thomas P. Gleason, Peter Mielke, David Stewart, and Tyler B. McDonnell. Photos courtesy of Cody Kuntz.

energy released in light is dependent on the energy gap. They were then taught that a reversed LED is the basis for a solar cell.

The quantum library station was available during the program for students who wished to learn more than what the program offered or wanted the option of learning the material in their own way. Parents also enjoyed the quantum library as they waited for their children to complete the program! The books provided parents with knowledge that enabled them to discuss the scientific concepts with their children after the program ended.

This outreach event exposed students to quantum physical concepts while also highlighting everyday technologies that make use of quantum physics. Students became more intrigued after participating in hands-on activities and completing their passports. We are energized by the feedback we received from families and will refine our efforts to help young students build a foundation to learn modern physics. //

To learn more about this project, visit spsnational.org/awards/marsh-w-white-outreach-award/2019/university-maryland-college-park.

ESCAPE THE PHYSICS BUILDING

Marsh White 2018–19

University of Texas at Dallas

Project Lead: Andrew Marder and Austen Adams

Project Advisor: Jason Slinker

Project Summary: The SPS chapter of the University of Texas at Dallas presented its second annual "Escape the Physics Building" event, centered around a physics-themed escape room and hosted in our very own physics building. The hope of this project was to pique interest in physics and showcase what SPS could accomplish to members of the campus community.

The challenge: Gain access to the prestigious Dr. Gamma's laboratory and, upon entering, help Dr. Gamma's lead lab technician, Denton, prevent the catastrophic failure of a "black hole generator" that is threatening to consume the entire building.

This is what participants face during "Escape the Physics Building," one of the last SPS events held during the academic year, serving as a final opportunity to get students interested in SPS before they go home for the summer. Our hope is that this event makes a lasting final impression, leading students to return to SPS at the beginning of the next academic year. It also occurs a few weeks before our SPS officer elections, giving members an opportunity to work with the officers and determine if they would like to run for an officer position themselves.

Participants in the event enter the lobby of our local physics building in small groups and are ushered into a nearby classroom, while one of our officers begins a timer. Groups then work together to solve small puzzles, making their way through three separate rooms to save the physics building from destruction! The puzzles include a Nobel Prize–themed riddle, a hidden message within a circuit board (visible with use of a thermal camera), and a magnetized message revealed by cleverly maneuvering some nearby iron shavings.

Upon completion, group times are recorded and displayed on a leaderboard, and snack-based prizes are awarded to the winners.

Despite being planned for groups of about four students, one brave soul attempted the escape room entirely on his own. On average, a group of students took about 30 to 40 minutes to complete the escape room, but this individual persevered through an hour-long mission to save the building. Some freshmen who had heard about the escape room also participated. They had the opportunity to interact with our treasurer, Ben, who at the time was playing the role of Denton and led them through their perilous journey with plenty of theatrics.

After the event, we sat down with a handful of participants to get their feedback and thoughts. The vast majority were surprised that it was a group of students who put on the event without large participation by professors or staff. As the officers, we were especially glad to hear this bit of feedback. Some students even expanded on the concept by saying the event made them feel like they, too, could help create something through SPS that "could actually come to fruition." We believe the project as a whole furthered interest in physics for both current physics students and those not affiliated with SPS or the physics department. **//**

To learn more about this project, visit spsnational.org/ awards/marsh-w-white-outreach-award/2019/university-texas-dallas.
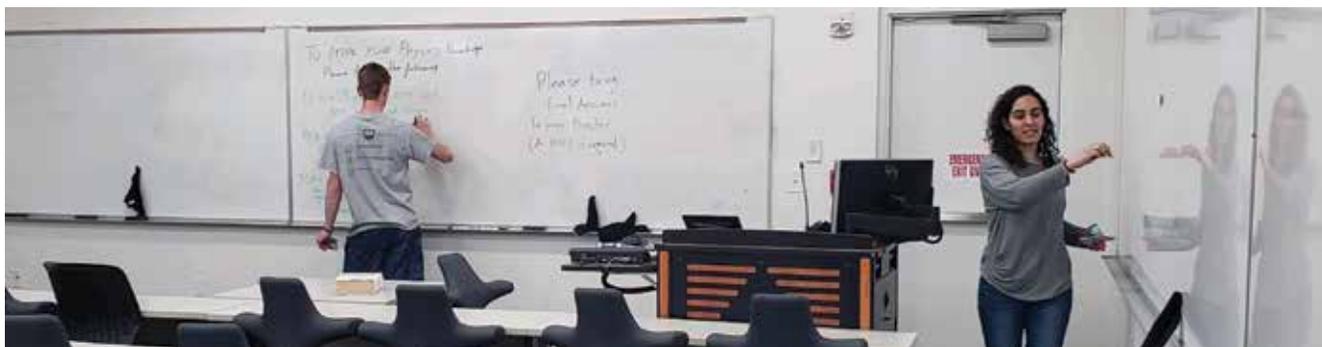
TOP: Students discuss their experience and learn about SPS after completing the escape challenge.

ABOVE: Duo searching for various scientists' names to decipher a riddle. Photos courtesy of University of Texas at Dallas SPS chapter.

COMPUTING MATCHUP: SMALL SUPERCOMPUTER CLUSTER VS. SINGLE NODE

2018–19 SPS Chapter Research Award

University of Kentucky

Project Leads: Alex Blose, Ben Kistler, Dany Waller

Chapter Advisor: Charles Brown

Project Summary: Computational methods are powerful tools for solving problems. We built an inexpensive mini supercomputer for use in research, education, outreach, and community building. Once our supercomputer was operational, we then used it to explore how parallel processing impacts the accuracy and processing time of physics-related computing tasks.

Physicists often work with enormous amounts of data that require lots of computational power to analyze. With access to supercomputers, researchers can now run complex computational models and analysis programs more quickly than ever before. Today's physics students need training in these methods, so our chapter decided to build a mini supercomputer and explore how it processes tasks relevant to physics research.

Our supercomputer is based on Tiny Titan, an inexpensive supercomputer you can build from a cluster of nine Raspberry Pi computers. The cluster can be confined to one Raspberry Pi—known as a "node" in the Tiny Titan build—or more so that you can examine accuracy and processing time as a function of node number.

Approximately 25 SPS members were engaged in this project. The first step was assembling the Raspberry Pis and loading an operating system. Then we connected them in the Tiny Titan configuration and, after some troubleshooting, our supercomputer came alive! Team members first learned how to access nodes from the master unit and pass commands, and then began studying how the number of nodes impacts the accuracy and efficiency of three types of simulations.

Modeling a Complex Fluid

We installed a fluid dynamics simulation, designed by Oak Ridge National Laboratory, on our cluster. The simulation approximates a fluid as a collection of balls. Users input the physical properties of the fluid and the number of balls in the fluid (similar to how you might define the number of pixels in an image), and the program models the resulting behavior. We found that the best way to improve the accuracy and efficiency of the simulation was to increase the number of balls, divide the water into sections, and then assign each section to a different node. More nodes always produced better results.

Estimating π

Irrational numbers like π are notoriously hard to calculate because of their nonalgebraic nature. We estimated π with a Monte Carlo simulation based on the ratio of the area of a circle to the area of the square in which the circle is inscribed. The program computes π using N random points, where N is input by a user. We studied how many digits of π our system could calculate with reasonable accuracy as a function of N and the number of nodes. Our results show that for high values of N, increasing the number of nodes decreases the processing time and improves accuracy.

LEFT: Team members prepare to set up the nine Pis. Photo by Dany Waller.

RIGHT: Success! The operating system boots up. Photo courtesy of the University of Kentucky's SPS chapter.

Employing the Ising Model

The Ising model describes the ferromagnetic behavior of materials. Our goal was to model the effects of temperature on magnetism and look at the transition point where ferromagnetic materials become magnetic or nonmagnetic. We are still developing this code.

In addition to continuing work on the Ising model, we are using our mini supercomputer for outreach and individual research projects. We have met new faculty, graduate students, and classmates and look forward to working with many of them on collaborative projects. The cluster has also been a great recruitment tool and helped foster a more inclusive and welcoming environment in SPS. Overall, this has been an excellent learning experience for everyone in our chapter, drawing in physics undergraduates at all levels to learn new skills and mentor others. **//**

To learn more about this project, visit **spsnational.org/awards/sps-chapter-research-award/2019/university-kentucky**.

ABOVE: Flyer used for advertising "Escape the Physics Building."

INVESTIGATING THE IONIC CONDUCTIVITY PLATEAU IN LITHIUM GLASSES

2018–19 SPS Chapter Research Award

Coe College

Project Lead: Anne Ruckman

Chapter Advisor: Caio Bragatto

Project Summary: Research suggests that the ionic conductivity of glass is influenced by the presence of lithium, but the physical mechanisms behind this behavior are not well understood. We investigated this experimentally and computationally by preparing silicate and borate glass samples with different lithium concentrations, conducting electrical impedance spectroscopy measurements, and comparing our results to predictions from existing models.

The electrical conductivity of a glass depends on the number of available charge carriers and their speed. In ionic materials, the charge carrier is almost always an alkali metal or monovalent metal. Scientists expect that glasses with higher alkali ion concentrations should have greater ion conductivity because there are more available charge carriers. However, this is not the case in glasses with high concentrations of lithium. Instead, the ionic conductivity seems to plateau.

The literature often interprets this plateau as an experimental rather than physical limitation, or as a change in glass structure. However, neither of these interpretations fully explain the observed behavior. Molecular dynamics simulations suggest that when present in high concentrations, lithium ions cluster and inhibit a rise in ionic conductivity.

To get a better understanding of this behavior, our chapter experimentally and computationally investigated the impact of lithium concentration on the properties of lithium borate oxide glasses. The Coe College physics department was well equipped for this project, with the capacity to prepare glass samples with high concentrations of lithium and a newly acquired impedance spectrometer, which is necessary for measuring ionic conductivity.

After learning several techniques and refining the process through troubleshooting, we successfully prepared samples of silicate glass and borate glass with various concentrations of lithium. Then we ground the samples into a powder for analysis. We characterized the properties of each sample with electrical impedance spectroscopy, differential scanning calorimetry, Raman spectroscopy, X-ray diffraction, and nuclear magnetic resonance. This gave us a picture of their electrical and thermal properties as well as atomic structures.

The physical properties and glass structures we measured agreed well with the results published in literature and, importantly,

TOP: Coe College SPS member Graham Beckler compresses glass powder into aluminum-lined pellets for conductivity testing.

ABOVE: SPS advisor Dr. Caio Bragatto, left, with project leader Anne Ruckman and fellow student researchers Ethan Weber and Will Guthrie. Photos courtesy of the Coe College SPS chapter.

all followed the same conductivity trend. This indicates that our samples were homogeneous.

Most of our results agreed with existing models. However, we noted a discontinuity in ionic conductivity between the leading model and our experimental results—the same plateau that appears in other published experimental results. This supports the theory that something interferes with the ionic conductivity that's not accounted for in the model. Our work adds to the literature about this interaction, and we are looking forward to sharing it with other researchers in the field.

Eight SPS chapter members were actively engaged in this research project, and many others attended a related research talk and visit to a lab at Iowa State University that collaborated with us. As researchers, we learned novel techniques, gained experience on new equipment, and enhanced our communication, teamwork, and problem-solving skills. This project also strengthened the

relationship between undergraduates and faculty members and between first-year undergraduates and more senior students in our chapter. We look forward to continuing this area of research and further utilizing our newly acquired skills. **//**

To learn more about this project, visit spsnational. org/awards/sps-chapter-research-award/2019/coe-college.

BUILDING BRIDGES BETWEEN NEW INDUCTEES AND ALUMNI

2019 Chapter Project Award

United States Air Force Academy

Project Lead: Lucy Zimmerman

Chapter Advisor: Alina Gearba-Sell

Project Summary: The United States Air Force Academy (USAFA) Sigma Pi Sigma chapter held its fifth induction ceremony in the spring of 2019. At this ceremony, we celebrated our chapter alumni and inducted nine students and seven faculty members, bringing our total number of members to 85.

In honor of the fifth anniversary of the founding of the Sigma Pi Sigma chapter at USAFA in 2019, we made additional efforts to reconnect with alumni. Twelve current Sigma Pi Sigma members were in attendance during the 2019 induction ceremony. First Lieutenant Scott Alsid (ΣΠΣ '14, USAFA '15), the first Sigma Pi Sigma member of the USAFA chapter, joined us for the event, as well as Lieutenant Colonel (ret.) Dan Polsgrove and Lieutenant Colonel (ret.) Brian Smith, both inducted in 2015. The presence of alumni added greater distinction to this year's induction ceremony and fostered stronger interactions between alumni and new Sigma Pi Sigma members. Additional alumni expressed their regrets for not being able to make it this year but demonstrated interest in attending future induction ceremonies.

Colonel Rex Kiziah, head of the USAFA Physics Department, provided the opening remarks for our event and discussed the value and importance of being a member of Sigma Pi Sigma. The induction ceremony was performed by Dr. Alina Gearba-Sell, our chapter advisor, and Cadet Second Class Lucy Zimmerman served as master of ceremonies. Dr. Gearba-Sell discussed the history of Sigma Pi Sigma, the upcoming Physics Congress, and the Sigma Pi Sigma Centennial.

This event also promoted awareness of Sigma Pi Sigma at USAFA. By inducting several members of the junior and senior

classes into Sigma Pi Sigma, we encouraged future physics majors to strive for excellence and an invitation to join this prestigious honor society. The event also helped encourage greater appreciation for Sigma Pi Sigma and the lifetime opportunities available to its members.

In the past, we have held induction ceremonies in conjunction with other institutions. In the spring of 2018, we hosted Dr. Willie Rockward, a past Sigma Pi Sigma president, and seven faculty and students from the University of Colorado Colorado Springs and Colorado College in an effort to strengthen the collaboration between our chapters. In the future, the USAFA Sigma Pi Sigma

TOP: Lieutenant Colonel (ret.) Monte Anderson cuts the cake.

MIDDLE: Cadet Second Class Kayla Brown receives her certificate.

BOTTOM: Faculty, students, alumni, family, and friends at the USAFA Sigma Pi Sigma induction ceremony. Photos courtesy of the USAFA Sigma Pi Sigma chapter.

chapter plans to continue alumni involvement while also reaching out to local schools. We anticipate these efforts will increase the collaboration and growth of SPS/Sigma Pi Sigma in the Colorado Springs area. //

To learn more about this project, visit spsnational.org/sigmapisigma/awards/chapter-project-award/united-states-air-force-academy-0.

AN EMPHASIS ON PHYSICISTS— PAST, PRESENT, AND FUTURE

2019 Chapter Project Award

Missouri Southern State University

Project Lead: Toby Pederson

Chapter Advisor: Jency Sundararajan

Project Summary: The Missouri Southern State University physics community came together to share in Sigma Pi Sigma induction traditions and build community across generations.

The extended Missouri Southern State University (MSSU) physics community reunited in April of 2019 to welcome the next generation of members into Sigma Pi Sigma. Our day of celebration began with the induction of six physicists. This particular ceremony was special in that five members joined Sigma Pi Sigma in the same induction class as our SPS advisor, Dr. Jency Sundararajan.

Our induction began with a welcome from Toby Pederson, MSSU SPS president and Sigma Pi Sigma member, who reflected on the goals of the Society of Physics Students and the history of Sigma Pi Sigma. Dr. Sundararajan discussed the importance of Physics Congresses and encouraged everyone to attend the 2019 Congress in Providence. Then we heard from several faculty who are members of Sigma Pi Sigma.

Dr. Rabindra Bajracharya reminded us of the Sigma Pi Sigma mission to serve and support the physics community, which is achieved by our chapter via outreach, collaboration, and the development and maintenance of alumni networks. Dr. Shayna Burchett described the significance of the Sigma Pi Sigma key, insignia, seal, and motto. The presiding officer of the event, Dr. Daniel Marsh, then shared his experience as a member of Sigma Pi Sigma, highlighted the responsibilities of joining this distinguished group, and invited the incoming class to be inducted into the Physics Honor Society.

Our new inductees joined Sigma Pi Sigma, following the three-step tradition used in each MSSU ceremony: each member ignited a candle displaying a picture of a favorite physicist, signed our

chapter's Red Book, and demonstrated electromagnetic induction to symbolize the Sigma Pi Sigma induction. Pederson then led the charge to the incoming class of Sigma Pi Sigma members and congratulated our new inductees.

After the induction ceremony, our extended physics community gathered for an informal alumni picnic. We were joined by the dean of the College of Arts and Sciences, as well as MSSU faculty, students, alumni, local professionals, and Sigma Pi Sigma members and their families.

This Sigma Pi Sigma induction ceremony and alumni gathering was an informative and motivational experience for current students. The ceremony and picnic provided an excellent venue for students to meet recent graduates and learn about their experiences as graduate students, in the workplace and in conducting research. Students and alumni bonded as they shared their personal experiences as physics students, and our event helped those in attendance make professional contacts and network with local industry personnel.

With this Sigma Pi Sigma Chapter Project award, we were able to engage alumni by bringing together the local physics community, and expand recognition of Sigma Pi Sigma on campus and in the surrounding community. It was a proud occasion for new inductees and inspired the next generation of physics students to work toward an invitation to Sigma Pi Sigma. //

To learn more about this project, visit spsnational. org/sigmapisigma/awards/chapter-project-award/ missouri-southern-state-university.

ABOVE LEFT: Left: Electromagnetic induction demo used to symbolize Sigma Pi Sigma induction. Right: The table setup for the induction ceremony.

ABOVE: Cori Smith, MSSU alumnus, is inducted into Sigma Pi Sigma.

LEFT: Current students, alumni, and SPS members share a picnic lunch. Photos courtesy of the MSSU Sigma Pi Sigma chapter.

The SPS Summer Internship Program offers SPS members 10-week positions in the Washington, DC, area. Interns participate in research, education, policy, and outreach and are placed in organizations such as the American Physical Society, American Association of Physics Teachers, Society of Physics Students, The Optical Society, Capitol Hill, NASA, and the National Institute for Standards and Technology, among others. Over the course of the summer, students engage in a diverse set of activities and projects that collectively provide the interns with a unique learning and professional development opportunity.

The interns maintain weekly blogs highlighting their work and significant experiences. The following articles are excerpts from the journals of a few SPS interns from last summer.

You can find out more about the SPS Internship Program here: spsnational.org/programs/internships.

STARDATE 73012.1

Nolan Roth, 2019 SPS Intern, NASA Goddard Space Flight Center, SPS Member at High Point University

It's hard to know what you want to do for the rest of your life if you don't know what's out there to be done. Oh, you think, the classic unsolved problem of the student! How can it ever be approached? One of the great things about the SPS internship program is that it works to remedy that problem.

Throughout the program, participants have the opportunity to tour each of the intern placement sites, among them NASA, NIST, Capitol Hill, and the Optical Society. These tours reveal the many sides of physics—including those that tend to be out of the spotlight. Physics isn't just about doing research—it can also involve writing, communication, education, outreach, design, and roles in the humanitarian, historical, and social arenas. Students can benefit from learning about these different outlets and from diversifying their network of research opportunities. I definitely have.

During our tour of the Capitol, we visited congressional offices, congressional hallways, congressional statues, congressional bathrooms, and the congressional food court—and we even got to meet with a congressman! The highlight of the day was the hour-long meeting with Illinois Rep. Bill Foster, the only congressperson to have a PhD in physics. The meeting with him was riveting! He

ABOVE: SPS interns meet with Congressman Bill Foster of Illinois. Photo courtesy of SPS National.

spoke on his past, the moral issues of the present, and how to make a difference in the future. He gave book recommendations (one of which, *Sapiens*, by Yuval Noah Harari, is my new favorite nonfiction book) and asked each of us about our summer work. It was a wonderful opportunity, and I believe we all walked out with extra knowledge on the direction of science policy.

That same week featured the NASA tour. We zigzagged across the Goddard campus, popping into buildings, walking through research labs, visiting gift shops, and, most notably, attending the Science Jamboree.

Every summer, NASA hosts this large event that's open to the public (public-ish—you still need badges to get on campus). Teams from many of NASA's large projects set up booths during the event, using demonstrations or models to teach other people about what they do. It was a hotbed of science research, and I loved it. I wended my way through crowds of curious people gathering many pounds' worth of free stickers, bags, posters, and fliers. I introduced myself to various project leads, exchanged cards, and learned about some amazing science that I would love to explore, including TEMPO's space communications network project and the Discover supercomputer in the NASA Center for Climate Simulation.

It's still hard to know what I want to do for the rest of my life, but now I know a bit more about what's out there. The classic unsolved problem of the student may not be completely solved, but with this internship, I've begun to chip away at it. **//**

IT'S THE END OF THE SPS INTERNSHIP AS WE KNOW IT

Terance Schuh, 2019 SPS Intern, NASA Goddard Space Flight Center, The College of New Jersey

(And I feel fine!) This summer has been great, and while I think I'm ready to head home, I want to take time to acknowledge some of the awesome things that came out of this internship! These aspects weren't, by far, inclusive of everything that came out of my SPS internship experience, but they were the highlights.

I made a lot of friendships and connections that I won't soon forget.

Unfortunately, not everyone in the physics community is going to be your friend, but if you're one of those sad souls like me who loves the subject, I promise you'll have no trouble finding a group of people that you end up calling your "physics phamily." That trend continued for me this summer. From the awesome interns in the program and those at SPS who selected us, to my incredible mentors at NASA and my fellow NASA intern lunch buddies—all of these people reminded me once again that I am exactly where I want to be. These are my people; this is my field.

ABOVE: SPS interns take a tour of NASA and enjoy the annual summer Science Jamboree. Photo courtesy of SPS National.

ABOVE: SPS interns take a tour of the National Institute of Standards and Technology (NIST). Photo courtesy of SPS National.

I learned a ton more physics.

Even though I took many physics courses in undergrad, some things are impossible to learn unless you're forced to literally deal with them every day. My research, greatly centered around a subfield called continuum mechanics, fell into that category. One of the first things my mentors told me when I arrived was, "The physics you're going to learn here, you won't learn in school." That's the truth about much of physics in the 21st century, and I'm glad I got a taste of that.

I gained more research skills.

I'm grateful that my mentors allowed me to work on a project that provided room for developing all-around useful research skills. One of the most significant skills I learned was how to develop my own individual research ideas. Even though I've had past research experiences, I've still always been curious about how someone transforms from a researcher who carries out someone else's ideas to one who generates their own unique ideas for future projects.

I got to live in the heart of a large city.

I've never been and still am not keen on city life, especially when it's lived out of a college dorm. I will say, though, that I'm glad I got to experience it. //

THE FINALE

Samantha Staskiewicz, 2019 SPS Intern, AIP FYI Science Policy Communications Intern, The College of New Jersey

I've been back home in New Jersey for a little over a week now, and it's a bittersweet feeling. This summer was truly unforgettable, and I'm so grateful for all the opportunities SPS has given me.

I can't stress enough how special this internship program was, and I truly think that any physics major interested in an internship or summer physics experience should apply. In fact, I wish I had known about this program earlier on in my college career. Although my REU program was eye-opening, it was particularly rewarding to gain physics experience that wasn't research based.

People have often asked me if I plan to be a teacher or if I want to go to graduate school. Other career options aren't stressed much to physics undergraduates. Because of this, I really valued being able to see everything the other interns accomplished over the summer—and how much you can truly do with physics.

Thank you, SPS, for everything. I'm definitely going to tell all of my College of New Jersey physics friends to apply for the program next year—so be on the lookout! //

JURP

JOURNAL *of*
UNDERGRADUATE REPORTS IN PHYSICS

What is JURP?

The Journal of Undergraduate Reports in Physics (JURP) is a peer-reviewed publication of the Society of Physics Students comprised of research, outreach, and scholarly reporting.

JURP provides exposure for SPS members conducting physics research while also highlighting SPS members' participation in SPS programs, awards, and outreach.
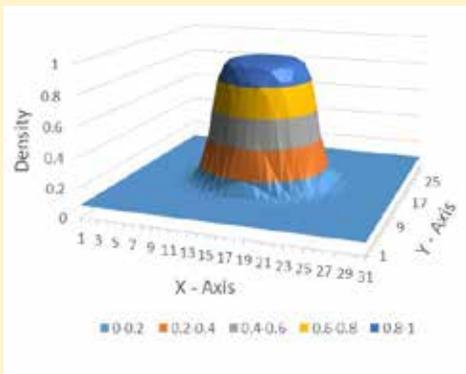
Research

Peer-reviewed papers within any area of physics research.

Accepted research submissions are indexed and searchable.

Programs

Conference reflections, SPS chapter award final reports, SPS intern blogs, and other special programs articles.

Submit Your Report!

All current SPS members are eligible to submit to JURP. The author(s) must have performed all the work reported in the paper as an undergraduate student.

SPS National will accept submissions to JURP on a rolling basis, but final deadline for the print edition is **March 15**.

AIP
American Institute
of Physics

To submit your report and review previous JURP publications, please visit www.spsnational.org/jurp.

SPS